International Journal for Numerical Methods in Fluids

WILEY

RESEARCH ARTICLE OPEN ACCESS

Monolithic Newton-Multigrid Finite Element Methods for the Simulation of Thixoviscoplastic Flows

Naheed Begum | Abderrahim Ouazzi | Stefan Turek

Institute for Applied Mathematics, LSIII, TU Dortmund University, Dortmund, Germany

Correspondence: Naheed Begum (naheed.begum@math.tu-dortmund.de)

Received: 8 February 2024 | **Revised:** 8 November 2024 | **Accepted:** 18 November 2024

Funding: This study was supported by the Deutsche Forschungsgemeinschaft (DFG, German Research Foundation) (446888252), the “Bundesministerium für Wirtschaft und Energie aufgrund eines Beschlusses des Deutschen Bundestages” through “AiF-Forschungsvereinigung: Forschungs-Gesellschaft Verfahrens-Technik e. V.—GVT” under the IGF project number 20871N, and the LSIII and LiDO3 team at ITMC, TU Dortmund University, Germany.

Keywords: 4:1 contraction *Int. J. Numer. Meth. Fluids* | adaptive discrete Newton | finite element methods | generalized Navier–Stokes equations | lid-driven cavity | monolithic | Newton-multigrid | thixoviscoplastic flows

ABSTRACT

In this paper, we shall be concerned with the development, application, and numerical analysis of the monolithic Newton-Multigrid finite element method (FEM) to simulate thixoviscoplastic (TVP) flows. We demonstrate the importance of robustness and efficiency of Newton-Multigrid FEM solver for obtaining accurate solutions. To put our work in proper perspective w.r.t. the delicate challenge of obtaining accurate numerical solutions for TVP flow problems, we content our investigation to TVP quasi-Newtonian modeling approach with an extensive analysis on lid-driven cavity flows, and expose the impact of thixotropic scale in 4:1 contraction configuration application. fldauth.cls class file for setting papers for the *International Journal for Numerical Methods in Fluids*. Copyright 2010 John Wiley & Sons Ltd.

In this paper, we shall be concerned with the development, application, and numerical analysis of the monolithic Newton-Multigrid finite element method (FEM) to simulate thixoviscoplastic (TVP) flows. We demonstrate the importance of robustness and efficiency of Newton-Multigrid FEM solver for obtaining accurate solutions. To put our work in proper perspective w.r.t. the delicate challenge of obtaining accurate numerical solutions for TVP flow problems, we restrict our investigation to TVP quasi-Newtonian modeling approach and lid-driven cavity flows.

1 | Introduction

Thixoviscoplastic (TVP) flow integrates the competitive process of *Aging* and *Rejuvenation* inhabited in the material via plasticity and thixotropy interplay. The viscoplastic equations are supplemented with the evolution microstructure equation, which incorporates buildup and breakdown functions responsible for such processes [1]. It is a nonlinear multifield two-way coupled problem. Besides the microstructure-velocity coupling by means of microstructure-dependent plastic-viscosity and yield stress, TVP flow possesses the velocity-microstructure coupling due to not only the convection, but also to the shear rate-dependent buildup and breakdown functions. In addition, TVP flows incorporate different types of nonlinearities that make the numerical simulations a true challenge [2].

Monolithic Newton-Multigrid finite element method (FEM) solves TVP fields, microstructure, velocity, and pressure, simultaneously. We generalize discrete Newton's method by means of adaptive step-length control for the finite difference approximation of Jacobians. The adaptivity is dependent on the states of convergence that we quantify with the actual rate of the residual convergence. We solve linearized systems inside the outer Newton loops using the monolithic geometric Multigrid method (GMG) with local pressure Schur complement schemes for saddle point problems [3, 4]. They are simple iterative relaxation methods that solve directly on element level, one element or a patch of elements, and perform an outer block Gauss–Seidel iteration. The choices of the blocks are based on the incompressibility constraint or equivalently on the pressure degrees of freedom. Accordingly, for the efficiency of the algorithm, on one hand, we adopt a discontinuous FE approximation for the pressure, and opt for higher order stable Stokes FEM pair, that is biquadratic, and discontinuous linear for velocity, and pressure, respectively [5]. On the other hand, due to no coupling between the pressure and microstructure, we collocate the microstructure and velocity in the same degrees of freedom. The local character of this procedure together with a global defect-correction mechanism, and the choice of discontinuous FE approximations for pressure, results in an efficient solver for TVP problems. Furthermore, the convergence of the linear solver is made to match the optimal accuracy of the nonlinear solver, and the resultant algorithm is of blackbox-type. We analyze the performance of the adaptive discrete Newton-Multigrid solver in comparative studies with different methods and with results available from literature in case studies of benchmark character, that is, flow around cylinder benchmark and lid-driven cavity. In addition, in order to study the performance of the solver w.r.t. different boundary conditions settings and regularization, we manipulate different BCs settings to obtain the same flow fields solution for the classical analytical Bingham viscoplastic benchmark to gather the analysis of this important issue in one example.

For the numerical analysis of the accuracy, robustness, and efficiency of the Newton-Multigrid FEM solver and TVP phenomena, we use lid-driven cavity benchmark to analyze the optimal settings, mesh refinement, and regularization. We investigate the point-wise mesh convergence, and the mesh refinement independency of the solver. We consider the classical lid-driven cavity on unity square for our study of Newtonian, viscoplastic, and TVP flows. The flow is generated by moving the upper lid with x-velocity set to unity, which comes into contact with the stationary walls. That is, the flow problem is subject to nonhomogeneous Dirichlet boundary conditions for x-velocity at the upper boundary wall, and homogeneous Dirichlet boundary conditions at the other walls.

First, we start with the Newtonian lid-driven cavity flow benchmark. It introduces nonuniform recirculating flows with well-studied vortices with respect to Reynolds number. Besides being the benchmark for global quantities, for instance, kinetic energy and enstophy, it also provides a point-wise benchmark, namely the location of vortices and x-axis cutline solutions. We investigate the global quantity benchmark using the kinetic energy, and the point-wise benchmark with the help of the velocity magnitude at the vertical centerline and the locations of the primary and the lower left secondary vortices for the particular Reynolds number set to 1000, 5000, and 10,000, respectively. We also present the corresponding Newton-Multigrid solver behavior.

Second, we analyze the viscoplastic lid-driven cavity flow benchmark. The quasi-Newtonian modeling approach for yield stress materials introduces a regularization parameter to get a well-defined extended viscosity function in the whole computational domain. Hence, we investigate the accurate growth, and location of unyielded regions with respect to the optimal settings of regularization, and mesh refinement, for increased values of the yield stress parameter. Moreover, we analyze the corresponding Newton-Multigrid solver convergence with respect to all parameters, namely the yield stress parameter, and the regularization parameter on successive mesh refinement levels. Meanwhile, we check the optimal strategy for fast convergence for the nonlinear solver.

Finally, we present TVP lid-driven cavity flow, and TVP 4:1 contraction flow. TVP flow equations, in a quasi-Newtonian modeling approach, are an upgrade of generalized viscoplastic Navier–Stokes equations in two aspects. On the one hand, the extended viscosity function integrates the microstructure via thixotropic plastic viscosity and thixotropic yield stress. On the other hand, the set of equations is supplemented with a microstructure equation. This equation reflects the competition process of Aging and Rejuvenation, which occurs via the interaction of buildup and breakdown functions dependent on two additional model parameters, namely buildup and breakdown parameters. Here, for lid-driven cavity, we also investigate the accurate growth and location of unyielded regions with respect to the optimal settings of regularization, and mesh refinement, for increased values of the thixotropic yield stress parameter. We analyze the corresponding Newton-Multigrid solver convergence with respect to the thixotropic yield stress parameter, and regularization parameter on successive mesh refinement levels. Moreover, we investigate the role played by the microstructure equation throughout the analysis of the types of transitions between yielded and unyielded regions. As far as the thixotropic 4:1 contraction flow, we develop a mechanism for obtaining proper boundary settings, and analyze the importance of taking into consideration the thixotropic scale for this close enough configuration to industrial application.

The present paper has the following structure. In Section 2, we introduce TVP's problem formulation in quasi-Newtonian modeling approach. Then, we derive the variational form for stationary TVP flow problems and present the problem in a general saddle point abstract framework. In addition, we present a higher-order FEM discretization based on stable two-field Stokes elements supplemented with necessary stabilization. In Section 3, the nonlinearity of the problem is treated with generalized discrete Newton method w.r.t. the Jacobian's properties, and the accuracy of the Jacobian calculation is related to residual convergences, having a global convergence. The linearized systems inside the outer Newton loops are solved using the GMG in Section 4. The performance and limitations of the solver are exposed in Section 5, with detailed comparative study with different methods and results from literature for cavity Bingham viscoplastic flow, and in Section 10 for flow around cylinder benchmark. Moreover, we manipulated different boundary conditions settings to obtain the classical analytical Bingham benchmark on unity channel to gather the analysis of the solver performance w.r.t BCs settings and regularization parameter in a single test example. Next, we use the lid-driven cavity benchmark to analyze numerically the accuracy, robustness, and efficiency of the Newton-Multigrid FEM solver and TVP phenomena in Section 6. We consider 4:1 contraction configuration in Section 7. We start by deriving a mechanism for obtaining a proper BC settings, and then we analyze the importance of taking into consideration the thixotropic scale in easing the flow along the configuration by inducing extra rejuvenation layer at the vicinity of the upstream channel, and freeing the 4:1 entrance from dead flow. Section 8 highlights the conclusions of the main topics and results presented in this paper.

2 | Problem Formulation

2.1 | Problem Settings

TVP flows are introduced into yield stress flows by taking into consideration the internal material microstructure λ. First, viscoplastic stress is modified to thixotropic stress dependent on the microstructure

$$\begin{cases} \boldsymbol{\sigma}(\lambda) = 2\eta(\lambda)\mathbf{D}(\boldsymbol{u}) + \tau(\lambda)\frac{\mathbf{D}(\boldsymbol{u})}{||\mathbf{D}(\boldsymbol{u})||} & \text{if } ||\mathbf{D}(\boldsymbol{u})|| \neq 0, \\ ||\boldsymbol{\sigma}(\lambda)|| \leq \tau(\lambda) & \text{if } ||\mathbf{D}(\boldsymbol{u})|| = 0, \end{cases} \tag{1}$$

where $\mathbf{D}(\boldsymbol{u})$ denotes the strain rate tensor. The norm for a tensor Λ is given by $||\Lambda|| = \sqrt{Tr(\Lambda^2)}$. We use $||\mathbf{D}(\boldsymbol{u})||$ and $||\mathbf{D}||$ alternately. η denotes the plastic viscosity, and τ defines the yield stress that is a threshold parameter from which the material starts yielding. The shear stress has two contributions: a viscous part, and a strain rate-independent part. Second, an evolution equation for microstructure is introduced to induce the time-dependent process of competition between the destruction (breakdown) and the construction (buildup) inhabited in the material

$$\left(\frac{\partial}{\partial t} + u \cdot \nabla\right)\lambda = \mathcal{F} - \mathcal{G}, \tag{2}$$

where $\mathcal{F}$ and $\mathcal{G}$ are two nonlinear functions representing the buildup and breakdown of material microstructure. A collection of thixotropic models with various choices of η, τ, $\mathcal{F}$ and $\mathcal{G}$ is given in Table 1.

Here η_0 and τ_0 are initial plastic viscosity and yield stress, respectively, in the absence of any thixotropic phenomena. η_∞ and τ_∞ are thixotropic plastic viscosity and yield stress. Λ_c is the critical elastic strain, and G_0 is the elastic modulus of unyielded material. $\mathcal{M}_a$ and $\mathcal{M}_b$ are buildup and breakage constants, and g, p, m, n are rate indices.

In the quasi-Newtonian modeling approach for TVP flows, an extended viscosity $\mu(\cdot,\cdot)$ is used for the generalized Navier–Stokes equations [11, 12]. For instance [13]:

$$\mu\left(D_{\mathrm{II}}, \lambda\right) = \eta\left(D_{\mathrm{II}}, \lambda\right) + \tau\left(D_{\mathrm{II}}, \lambda\right)\frac{\sqrt{2}}{2}\frac{1}{\sqrt{D_{\mathrm{II}}}}\left(1 - e^{-k\sqrt{D_{\mathrm{II}}}}\right), \tag{3}$$

where k is the regularization parameter. $D_{\mathrm{II}} = \frac{1}{2}(\mathbf{D}(\boldsymbol{u}) : \mathbf{D}(\boldsymbol{u}))$ is the second invariant of the strain rate tensor $\mathbf{D}(\boldsymbol{u})$. The generalized Navier–Stokes equations and the evolution equation for microstructure constitute the full set of modeling equations, that is given as follows:

$$\begin{cases} \left(\frac{\partial}{\partial t} + u \cdot \nabla\right)\boldsymbol{u} - \nabla \cdot \left(2\mu\left(D_{\mathrm{II}}, \lambda\right)\mathbf{D}(\boldsymbol{u})\right) + \nabla p = 0 \\ \nabla \cdot \boldsymbol{u} = 0 \\ \left(\frac{\partial}{\partial t} + u \cdot \nabla\right)\lambda - \mathcal{F}\left(D_{\mathrm{II}}, \lambda\right) + \mathcal{G}\left(D_{\mathrm{II}}, \lambda\right) = 0 \end{cases} \tag{4}$$

in Ω, where $\boldsymbol{u}$ denotes velocity, p the pressure, and λ the microstructure. $\mathcal{F}$ and $\mathcal{G}$ are the nonlinear functions for buildup and breakdown of material microstructure. In what follows, we proceed with the stationary TVP problems.

2.2 | Finite Element Discretization

To derive the variational form for TVP flows, we consider the spaces $\mathbb{V} := \left(H_0^1(\Omega)\right)^2$, $\mathbb{T} := H^1(\Omega)$, and $\mathbb{W} := \mathbb{V} \times \mathbb{T}$ be the product space of velocity and microstructure spaces $\mathbb{V}$ and $\mathbb{T}$, respectively. We denote by $\mathbb{Q} := L_0^2(\Omega)$ the pressure space. The velocity-microstructure space $\mathbb{W}$, and the pressure space $\mathbb{Q}$ are associated with H^1-norm $||\cdot||_1$, and L^2-norm $||\cdot||_0$, respectively (for details, we refer to [14, 15]).

Let $\tilde{\boldsymbol{u}} = (\boldsymbol{u}, \lambda)$ be the coupled field, for velocity and microstructure, and $\tilde{\boldsymbol{v}} = (\boldsymbol{v}, \xi)$ be its associated test coupled field. We introduce the TVP form for the coupled field defined on $\mathbb{W} \times \mathbb{W} \times \mathbb{W}$ as

$$a_{\tilde{u}}(\tilde{\boldsymbol{u}})(\tilde{\boldsymbol{u}}, \tilde{\boldsymbol{v}}) = a_{\boldsymbol{u}}(\tilde{\boldsymbol{u}})(\boldsymbol{u}, \boldsymbol{v}) + a_\lambda(\tilde{\boldsymbol{u}})(\lambda, \xi) \quad \forall(\tilde{\boldsymbol{u}}, \tilde{\boldsymbol{v}}) \in \mathbb{W} \times \mathbb{W}, \tag{5}$$

which is the sum of velocity form $a_{\mathbf{u}}(\cdot)(\cdot,\cdot)$ defined on $\mathbb{W} \times \mathbb{V} \times \mathbb{V}$ and microstructure form $a_\lambda(\cdot)(\cdot,\cdot)$ defined on $\mathbb{W} \times \mathbb{T} \times \mathbb{T}$.

We denote by $b(\cdot,\cdot)$, the bilinear form defined on $\mathbb{V} \times \mathbb{Q}$ related to incompressibility constraint.

The weak formulation for TVP flow problems (4) reads:

TABLE 1 | Thixotropic models.

	η	τ	$\mathcal{F}$	$\mathcal{G}$
Worrall et al. [6]	$\lambda\eta_0$	τ_0	$\mathcal{M}_a(1-\lambda)\lVert\mathbf{D}\rVert$	$\mathcal{M}_b\lambda\lVert\mathbf{D}\rVert$
Coussot et al. [7]	$\lambda^g\eta_0$		$\mathcal{M}_a$	$\mathcal{M}_b\lambda\lVert\mathbf{D}\rVert$
Houska [8]	$\left(\eta_0 + \eta_\infty\lambda\right)\lVert\mathbf{D}\rVert^{n-1}$	$\left(\tau_0 + \tau_\infty\lambda\right)$	$\mathcal{M}_a(1-\lambda)$	$\mathcal{M}_b\lambda^m\lVert\mathbf{D}\rVert$
Mujumbar et al. [9]	$\left(\eta_0 + \eta_\infty\lambda\right)\lVert\mathbf{D}\rVert^{n-1}$	$\lambda^{g+1}G_0\Lambda_c$	$\mathcal{M}_a(1-\lambda)$	$\mathcal{M}_b\lambda\lVert\mathbf{D}\rVert$
Dullaert et al. [10]	$\lambda\eta_0$	$\lambda G_0(\lambda\lVert\mathbf{D}\rVert)\Lambda_c$	$\left(\mathcal{M}_{a_1} + \mathcal{M}_{a_2}\lVert\mathbf{D}\rVert\right)(1-\lambda)t^p$	$\mathcal{M}_b\lambda\lVert\mathbf{D}\rVert t^{-p}$

Find $(\tilde{\boldsymbol{u}}, p) \in \mathbb{W} \times \mathbb{Q}$ *such that*

$$a_{\tilde{\mathbf{u}}}(\tilde{\boldsymbol{u}})(\tilde{\boldsymbol{u}}, \tilde{\boldsymbol{v}}) + b(\boldsymbol{v}, p) - b(\boldsymbol{u}, q) = 0, \quad \forall(\tilde{\boldsymbol{v}}, q) \in \mathbb{W} \times \mathbb{Q}. \tag{6}$$

The bilinear forms $a_\lambda(\tilde{\mathbf{u}})(\cdot,\cdot)$, $a_{\mathbf{u}}(\tilde{\mathbf{u}})(\cdot,\cdot)$, and $b(\cdot,\cdot)$ are given as follows:

$$a_\lambda(\tilde{\mathbf{u}})(\lambda, \xi) = \int_\Omega \left(-\mathcal{F}\left(D_{\mathrm{II}}, \lambda\right) + \mathcal{G}\left(D_{\mathrm{II}}, \lambda\right)\right)\xi \, d\Omega + \int_\Omega \mathbf{u} \cdot \nabla \lambda \xi \, d\Omega, \tag{7}$$

$$a_{\mathbf{u}}(\tilde{\mathbf{u}})(\mathbf{u}, \mathbf{v}) = \int_\Omega 2\mu\left(D_{\mathrm{II}}, \lambda\right)\mathrm{D}(\mathbf{u}) : \mathrm{D}(\mathbf{v}) \, d\Omega + \int_\Omega \mathbf{u} \cdot \nabla \mathbf{u} \mathbf{v} \, d\Omega, \tag{8}$$

$$b(\mathbf{v}, q) = -\int_\Omega \nabla \cdot \mathbf{v} q \, d\Omega. \tag{9}$$

The finite element approximations of the problem (6) have to take care of its saddle point character, due to the bilinear form (9). Furthermore, since TVP flows are usually slow, the only remaining issue is the coercivity of the bilinear form (7) in the norm of space $\mathbb{T}$. We opt for higher order stable pair biquadratic for velocity and piecewise linear discontinuous for the pressure, Q_2/P_1^{disc}, and higher order quadratic for microstructure Q_2 with the appropriate stabilization terms [16, 17]. Let the domain Ω be partitioned by a grid $K \in \mathcal{T}_h$ which are assumed to be quadrilaterals such that $\overline{\Omega} = \cup_{k\in\mathcal{T}_h} K$. For an element $K \in \mathcal{T}_h$, we denote by $\mathcal{E}(K)$ the set of all one-dimensional edges of K. Let $\mathcal{E}_i := \cup_{K\in\mathcal{T}_h}\mathcal{E}(K)$ be the set of all interior element edges of the grid $\mathcal{T}_h$.

We define the conforming finite element spaces $\mathbb{V}_h \subset \mathbb{V}$, $\mathbb{T}_h \subset \mathbb{T}$, and $\mathbb{Q}_h \subset \mathbb{Q}$ such that:

$$\mathbb{V}_h = \left\{\mathbf{v}_h \in \mathbb{V}, \mathbf{v}_{h|K} \in \left(Q_r(K)\right)^2 \forall K \in \mathcal{T}_h, \mathbf{v}_h = 0 \text{ on } \partial\Omega_h\right\}, \tag{10}$$

$$\mathbb{T}_h = \left\{\xi_h \in \mathbb{T}, \xi_{h|K} \in Q_r(K) \forall K \in \mathcal{T}_h\right\}, \tag{11}$$

$$\mathbb{Q}_h = \left\{q_h \in \mathbb{Q}, q_{h|K} \in P_{r-1}^{\mathrm{disc}}(K) \forall K \in \mathcal{T}_h\right\}, \tag{12}$$

where Q_r and P_r are polynomials with maximum power in each coordinate less or equal r, and total power less or equal r, respectively. In what follows, the polynomial power r is set equal to 2. Figure 1 exposes the distribution of degrees of freedom for the flow fields.

We set $\mathbb{W}_h := \mathbb{V}_h \times \mathbb{T}_h$, $\tilde{\mathbf{u}}_h = \left(\lambda_h, \mathbf{u}_h\right)$, $\tilde{\mathbf{v}}_h = \left(\mathbf{v}_h, \xi_h\right)$, and define on $\mathbb{W}_h \times \mathbb{W}_h$

$$a_{\tilde{\mathbf{u}}}\left(\tilde{\mathbf{u}}_h\right)\left(\tilde{\mathbf{u}}_h, \tilde{\mathbf{v}}_h\right) = a_{\mathbf{u}}\left(\tilde{\mathbf{u}}_h\right)\left(\mathbf{u}_h, \mathbf{v}_h\right) + a_\lambda\left(\tilde{\mathbf{u}}_h\right)\left(\lambda_h, \xi_h\right) \quad \forall\left(\tilde{\mathbf{u}}_h, \tilde{\mathbf{v}}_h\right) \in \mathbb{W}_h \times \mathbb{W}_h. \tag{13}$$

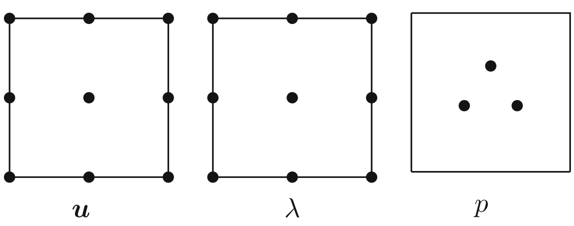

FIGURE 1 | FEM pair for thixoviscoplastic flow problem: Higher order FEM pair $Q_2/Q_2/P_1^{\mathrm{disc}}$.

The approximate problem reads: *Find* $\left(\tilde{\mathbf{u}}_h, p_h\right) \in \mathbb{W}_h \times \mathbb{Q}_h$ *s. t.*

$$a_{\tilde{\mathbf{u}}}\left(\tilde{\mathbf{u}}_h\right)\left(\tilde{\mathbf{u}}_h, \tilde{\mathbf{v}}_h\right) + j_{\tilde{\mathbf{u}}}\left(\tilde{\mathbf{u}}_h, \tilde{\mathbf{v}}_h\right) + b\left(\mathbf{v}_h, p_h\right) - b\left(\mathbf{u}_h, q_h\right) = 0, \quad \forall\left(\tilde{\mathbf{v}}_h, q_h\right) \in \mathbb{W}_h \times \mathbb{Q}_h. \tag{14}$$

The stabilization term $j_{\tilde{\mathbf{u}}}(\cdot,\cdot)$ is given as follows [17].

$$j_{\tilde{\mathbf{u}}}\left(\tilde{\mathbf{u}}_h, \tilde{\mathbf{v}}_h\right) := j_\lambda\left(\lambda_h, \xi_h\right) + j_{\mathbf{u}}\left(\mathbf{u}_h, \mathbf{v}_h\right), \tag{15}$$

$$j_{\mathbf{u}}\left(\mathbf{u}_h, \mathbf{v}_h\right) = \sum_{E\in\mathcal{E}_i} \gamma_{\mathbf{u}} |E|^2 \int_E \left[\nabla \mathbf{u}_h\right] : \left[\nabla \mathbf{v}_h\right] d\sigma, \tag{16}$$

$$j_\lambda\left(\lambda_h, \xi_h\right) = \sum_{E\in\mathcal{E}_i} \gamma_\lambda |E|^2 \int_E \left[\nabla \lambda_h\right]\left[\nabla \xi_h\right] d\sigma. \tag{17}$$

The stabilization (15) is consistent. The term (16) is typically used to stabilize the high Reynolds number flows for Newtonian case. And, the term (17) is used to make the coercivity and the continuity match in $\mathbb{T}_h$ associated with the norm

$$|||\xi_h|||^2 = ||\xi_h||_0^2 + j_\lambda\left(\xi_h, \xi_h\right) \quad \forall \xi_h \in \mathbb{T}_h. \tag{18}$$

For the well-posedness of the problem, we refer to [18]. The stabilized FEM discretization leads to a nonlinear discrete system. In the following Section 3, we present discrete Newton's method linearization techniques that we generalize to handle with robustness the Newton's forward iterates. This method is based on the adaptive manner of the finite difference approximations of the Jacobian.

3 | Generalized Discrete Newton Solver

The generalized discrete Newton's method consists of using an adaptive finite difference approximation of Jacobians w.r.t. states of convergence. It does not require any a priori analysis of the Jacobian, that is, it is a pure black box method.

Let $\left\{\varphi_i, i = 1, 2, \ldots, \mathtt{dim}\mathbb{W}_h\right\}$ and $\left\{\psi_i, i = 1, \ldots, \mathtt{dim}\mathbb{Q}_h\right\}$ denote the basis of the spaces $\mathbb{W}_h$ and $\mathbb{Q}_h$, respectively. We set $\mathcal{W} := \mathbb{R}^{\mathtt{dim}\mathbb{W}_h}$, $\mathcal{Q} := \mathbb{R}^{\mathtt{dim}\mathbb{Q}_h}$, $\mathcal{V} := \mathcal{W} \times \mathcal{Q}$, and denote by $\mathcal{R}(\mathcal{U}) \in \mathbb{W}_h \times \mathbb{Q}_h$, and $\boldsymbol{\mathcal{R}}(\boldsymbol{\mathcal{U}}) \in \mathcal{V}$, the continuous, and the discrete nonlinear residuals, respectively, for the system (14)

$$\mathcal{R}(\mathcal{U}) = \left(\mathcal{R}_\lambda(\lambda, \mathbf{u}), \mathcal{R}_{\mathbf{u}}(\lambda, \mathbf{u}, p), \mathcal{R}_p(\mathbf{u}, p)\right)^{\mathrm{T}}, \tag{19}$$

or in a compact form

$$\mathcal{R}(\mathcal{U}) = \left(\mathcal{R}_{\tilde{\mathbf{u}}}(\tilde{\mathbf{u}}p), \mathcal{R}_p(\tilde{\mathbf{u}}, p)\right)^{\mathrm{T}}, \tag{20}$$

where, the vector $\mathcal{U} = (\mathbf{u}, \lambda, p)^{\mathrm{T}} = (\tilde{\mathbf{u}}, p)^{\mathrm{T}} \in \mathbb{W}_h \times \mathbb{Q}_h$ is expressed as

$$\mathcal{U} = \sum_{i=1}^{\mathtt{dim}\mathbb{W}_h} \tilde{\mathbf{u}}_i \varphi_i + \sum_{i=1}^{\mathtt{dim}\mathbb{Q}_h} p_i \psi_i, \tag{21}$$

and where $\mathcal{U} \in \mathcal{V}$ represents the vector of the coefficients.

The nonlinear iteration is updated with the correction $\delta\mathcal{U}$, that is $\mathcal{U}^{l+1} = \mathcal{U}^l + \delta\mathcal{U}$. Then, the Newton linearization gives the following approximation for the residuals:

$$\mathcal{R}\left(\mathcal{U}^{l+1}\right) = \mathcal{R}\left(\mathcal{U}^l + \delta\mathcal{U}\right) \simeq \mathcal{R}\left(\mathcal{U}^l\right) + \left(\frac{\partial\mathcal{R}\left(\mathcal{U}^l\right)}{\partial\mathcal{U}}\right)\delta\mathcal{U}. \tag{22}$$

The Newton's method iterations, assuming invertible Jacobians, are given as follows:

$$\mathcal{U}^{l+1} = \mathcal{U}^{l} - \omega_l \left(\frac{\partial \mathcal{R}(\mathcal{U}^l)}{\partial \mathcal{U}} \right)^{-1} \mathcal{R}(\mathcal{U}^l). \tag{23}$$

The damping parameter $\omega_l \in (0,1]$ is chosen such that

$$\left\| \mathcal{R}(\mathcal{U}^{l+1}) \right\| \le \left\| \mathcal{R}(\mathcal{U}^{l}) \right\|. \tag{24}$$

The damping parameter is not sufficient for the convergence of this type of highly nonlinear problem, mainly due to the presence of Jacobian singularities related to the problem or simply by being out of the domain of Newton convergence [16, 19].

We use a generalized Newton's method to achieve a robust convergence. The method consists of using adaptive finite difference approximation of Jacobians w.r.t. the states of convergence. The idea behind consists of using an approximate Jacobians w.r.t. states of convergence, that is quadratic, stagnating, linear, superlinear, or sudden changes in convergence. Generally speaking, the method uses loose approximation of the Jacobians far away from the range of the quadratic convergence of Newton's method or close to a stagnating region, and accurate Jacobians in the quadratic region of convergence in an adaptive way [16, 19].

3.1 | Adaptive Newton via Operator-Adaptive Splitting

Based on a priori analysis of Jacobian's property, the Jacobian is split into a direct sum of corresponding operators with different properties, see [16, 19], as follows:

$$\left(\frac{\partial \mathcal{R}(\mathcal{U}^l)}{\partial \mathcal{U}} \right) = \mathcal{J}_1(\mathcal{U}^l) + \delta_l \mathcal{J}_2(\mathcal{U}^l). \tag{25}$$

Increasing the contribution from the second operator in the right side of the equation (25) improves the convergence behavior, but this contribution needs to remain under control. The relative changes of the residual give precious information about the singularity of the Jacobian. Indeed, the larger relative changes in the residual with the first operator in the RHS of (25) represent the "singularity" of the complementary operator contribution. In this case, the parameter δ_l should have a small relative change and remains small and increases as the convergence stagnates. The operator damping parameter δ_l is solely dependent on *the rate of actual residual convergence* r_l, defined as follows

$$r_l := \frac{\left\| \mathcal{R}(\mathcal{U}^l) \right\|}{\left\| \mathcal{R}(\mathcal{U}^{l-1}) \right\|}, \tag{26}$$

The contribution from the second operator in the right side of Equation (25) is controlled via the operator damping parameter $\delta_l \in [0,1]$, which is updated at each nonlinear using increment update

$$\delta_{l+1} = i_a(r_l)\delta_l. \tag{27}$$

In the context of continuous Newton's method, we developed numerically an adaptive increment update for the operator damping parameter in the adaptive Newton's method via operator-adaptive splitting [19], and was successfully applied in the simulations of sea ice models in [20], and granular models in [21], that is

$$i_a(r_l) = 0.2 + \frac{4}{0.7 + \exp(1.5 r_l)}. \tag{28}$$

Next, we provide an alternative black box adaptive Newton via step-length control in divide difference of discrete residual.

3.2 | Adaptive Newton via Adaptive Step-Length Control Parameter

The adaptive discrete Newton method used in the current work is based on adaptive step-length control in finite differences of discrete residuals. The method does not require any a priori analysis of the Jacobian, and it is a pure black box method. The discretization method to the system (14) leads to a system of nonlinear algebraic equations that can be represented as

$$\boldsymbol{\mathcal{R}}(\boldsymbol{\mathcal{U}}) = \mathbf{0}. \tag{29}$$

The Jacobian matrix $\boldsymbol{\mathcal{J}}(\mathcal{U}^l)$ is approximated using the finite differences as

$$\left[\boldsymbol{\mathcal{J}}(\boldsymbol{\mathcal{U}}^l)\right]_{ij} \approx \frac{\boldsymbol{\mathcal{R}}_i(\boldsymbol{\mathcal{U}}^l + \varepsilon_l \mathbf{e}_j) - \boldsymbol{\mathcal{R}}_i(\boldsymbol{\mathcal{U}}^l - \varepsilon_l \mathbf{e}_j)}{2\varepsilon_l}, \tag{30}$$

where $\mathbf{e}_j$ is the vector with unit jth component and 0 otherwise.

The Jacobian given by the finite difference Formula (30) is different from the Jacobian given by operator-adapted splitting Formula (25). Nevertheless, the feedback of the state of convergence is similar and it is given by the rate of the actual residual convergence r_l. The parameter ε_l is updated according to the rate of the actual residual convergence r_l (26), as follows

$$\varepsilon_{l+1} = j_a(r_l)\varepsilon_l. \tag{31}$$

As a consequence, the increment update function j_a should allow for a bigger step-length parameter ε to remove numerical instabilities, while the increment update function i_a reduces the contribution part responsible for the numerical instability. We simply take

$$j_a(r_l) = \frac{1}{i_a(r_l)}. \tag{32}$$

The robustness of choice (32) is also confirmed with numerical tests for dual formulation of Bingham viscoplastic model in [22, 23].

In contrast to the operator splitting strategy, the adaptive discrete Newton's method used here does not require any a priori analysis of the Jacobian; it is a pure black box method. Both methods differentiate between the states of convergence relaying on the feedback given by the rate of the actual residual convergence (26). Generally speaking, the former uses a smaller damping operator parameter to remove instabilities. Conversely, the latter allows for a bigger step-length parameter ε to remove such numerical instabilities. We present concisely the main steps for the solver in Algorithm 1.

The theoretical analysis of the global convergence property of the algorithm goes beyond the interest of this paper and remains an

ALGORITHM 1 | Discrete adaptive Newton using adaptive step-length.

Result: $\mathcal{U}^{l+1} = \mathcal{U}^{l} - \omega_l \delta\mathcal{U}^{l}$, $\omega_l := 1$

$r_0 = \left\| \mathcal{R}(\mathcal{U}^0) \right\|, \varepsilon_0 := 10^{-2}, \qquad \varepsilon_{\max} := 10^{-7}, j_a = \dfrac{1}{0.2 + \dfrac{4}{0.7 + e^{1.5x}}},$

$l_{\max} = 40,\ r_c = 10^{-8}$;

while $r_l \geq r_c \wedge l \leq l_{\max}$;

do

(i) **Calculate convergence rate** $r_l = \dfrac{\left\|\mathcal{R}(\mathcal{U}^l)\right\|}{\left\|\mathcal{R}(\mathcal{U}^{l-1})\right\|}$;

(ii) **Step-length size update** $\tilde{\varepsilon}_{l+1} = j_a(r_l)\,\varepsilon_l$;

$\varepsilon_{l+1} = \max(\tilde{\varepsilon}_{l+1}, \varepsilon_0) \vee \min(\tilde{\varepsilon}_{l+1}, \varepsilon_{\max})$;

(iii) **Calculate FD Jacobian** $\left[\mathcal{J}(\mathcal{U}^l)\right]_{ij} \approx \dfrac{\mathcal{R}_i(\mathcal{U}^l + \varepsilon_l \boldsymbol{e}_j) - \mathcal{R}_i(\mathcal{U}^l - \varepsilon_l \boldsymbol{e}_j)}{2\varepsilon_l}$;

(iv) **Solve via Monolithic MG** $\mathcal{J}(\mathcal{U}^l)\delta\mathcal{U}^l = \mathcal{R}(\mathcal{U}^l)$;

end

open problem. To solve the linear system inside each nonlinear iteration sweep, we use monolithic GMG, where the convergence of linear solver is made to match the optimal accuracy of the nonlinear solver [16]. Section 4 is devoted to monolithic geometric Multigrid linear solver.

4 | Monolithic Multigrid Linear Solver

The discretization and linearization of TVP problem (4) lead to systems of the following saddle-point type

$$\mathcal{J}(\mathcal{U})\delta\mathcal{U} = \begin{pmatrix} \mathbf{A}_{\tilde{\mathbf{u}}} & \mathbf{B}^{\mathrm{T}} \\ \mathbf{B} & \mathbf{O} \end{pmatrix} \begin{pmatrix} \delta\tilde{\mathbf{u}} \\ \delta p \end{pmatrix} = \begin{pmatrix} \mathcal{R}_{\tilde{\mathbf{u}}} \\ \mathcal{R}_p \end{pmatrix}. \tag{33}$$

The focus of this section is to develop monolithic GMGs for this type of system (33). GMGs effectively damp both high- and low-frequency components of errors using the complementary processes of relaxation/smoothing and coarse-grid correction. On the other hand, the coupled Multigrid method or Local Multilevel Pressure Schur Complement (LMPSC) approach as generalization of Vanka-like smoother was originally developed for Multigrid solvers for Navier–Stokes equations [4, 24] and extended to multifield problems [25]. The method solves exactly the local saddle-point problem on a subdomain and performs an overlapping block-Gauss–Seidel iteration. In the following, we briefly describe the principle of GMG via two-level algorithm and its corresponding components in the context of FEM discretization of TVP problem (14).

4.1 | Multigrid Algorithm

We consider the linear saddle-point problem (33) that we rewrite in the following manner

$$\mathcal{J}\delta\mathcal{U} = \mathcal{R}. \tag{34}$$

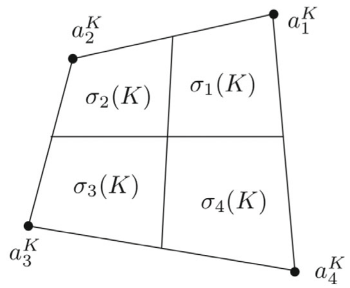

FIGURE 2 | Refinement of element K into subelements $\sigma_i(K)$, $i = 1, \ldots, 2^d$.

ALGORITHM 2 | V-cycle Algorithm.

Result: $MG(k, \delta\mathcal{U}_0, \mathcal{R}) = \delta\mathcal{U}_{\nu_1+\nu_2+1}$

For $k = 1$ on the coarsest level, the direct solver is used

$MG(1, \delta\mathcal{U}_0, \mathcal{R}) = \mathcal{J}_1^{-1}\mathcal{R}$;

while $1 < k \leq L$;

do

(i) **Pre-smoothing step** Let $\delta\mathcal{U}_l \in \mathcal{V}_k$ bedefined by $\delta\mathcal{U}_l = \delta\mathcal{U}_{l-1} + \mathcal{C}_k^{-1}(\mathcal{R} - \mathcal{J}_k\delta\mathcal{U}_{l-1}), \quad 1 \leq l \leq \nu_1$;

(ii) **Correction step** Let $\tilde{\mathcal{R}} = \mathcal{I}_k^{k-1}(\mathcal{R} - \mathcal{J}_k\delta\mathcal{U}_{\nu_1})$,

$\delta\mathcal{U}^c = MG(k-1, \mathbf{0}, \tilde{\mathcal{R}})$;

$\delta\mathcal{U}_{\nu_1+1} = \delta\mathcal{U}_{\nu_1} + \mathcal{I}_{k-1}^{k}\delta\mathcal{U}^c$;

(iii) **Post-smoothing step** Let $\delta\mathcal{U}_l \in \mathcal{V}_k$ be defined by $\delta\mathcal{U}_l = \delta\mathcal{U}_{l-1} + \mathcal{C}_k^{-1}(\mathcal{R} - \mathcal{J}_k\delta\mathcal{U}_{l-1}), \quad 1 \leq l \leq \nu_2$;

end

Let $\{\mathcal{T}_{h_k}\}$ be a family of hierarchy multilevel refinement associated with mesh size h_k, that is, each element on level partition $\mathcal{T}_{h_{k-1}}$ is split into 2^d ($d = 2$) new elements to get level partition $\mathcal{T}_{h_k}$ which are denoted by $\sigma_i(K)$, $i = 1, \ldots, 2^d$ (see Figure 2).

Let $\mathcal{I}_k^{k-1}$ and $\mathcal{I}_{k-1}^{k}$ denote the grid transfer operators, $\mathcal{I}_k^{k-1} : \mathbb{W}_k \times \mathbb{Q}_k \to \mathbb{W}_{k-1} \times \mathbb{Q}_{k-1}$ and $\mathcal{I}_{k-1}^{k} : \mathbb{W}_{k-1} \times \mathbb{Q}_{k-1} \to \mathbb{W}_k \times \mathbb{Q}_k$, and $\mathcal{I}_k^{k-1}$ and $\mathcal{I}_{k-1}^{k}$ be the matrices counterpart $\mathcal{I}_k^{k-1} : \mathcal{V}_k \to \mathcal{V}_{k-1}$ and $\mathcal{I}_{k-1}^{k} : \mathcal{V}_{k-1} \to \mathcal{V}_k$. The maximum Multigrid level is denoted by L, the parameters $\nu_1, \nu_2 \geq 0$ are the number of pre- and post-smoothing steps, respectively.

The k^{th} level iteration $MG\big(k, \delta\mathcal{U}_0, \mathcal{R}\big)$ of the Multigrid algorithm with initial guess $\delta\mathcal{U}_0$ yields an approximation to $\delta\mathcal{U}_k$, the solution of

$$\mathcal{J}_k\delta\mathcal{U} = \mathcal{R}. \tag{35}$$

We describe one step V-cycle in Algorithm 2.

In the pre/post-smoothing steps (i) and (ii), we assume $\rho\big(C_k^{-1}\mathcal{J}_k\big) \lesssim \rho\big(\mathcal{J}_k\big)$. We denote by $\delta\mathcal{U} = S^{\nu_i}(\delta\mathcal{U}, \mathcal{R}), i = 1, 2$ the pre/post-smoothing steps, and present schematically the Algorithm 2 for four-level refinement in Figure 3.

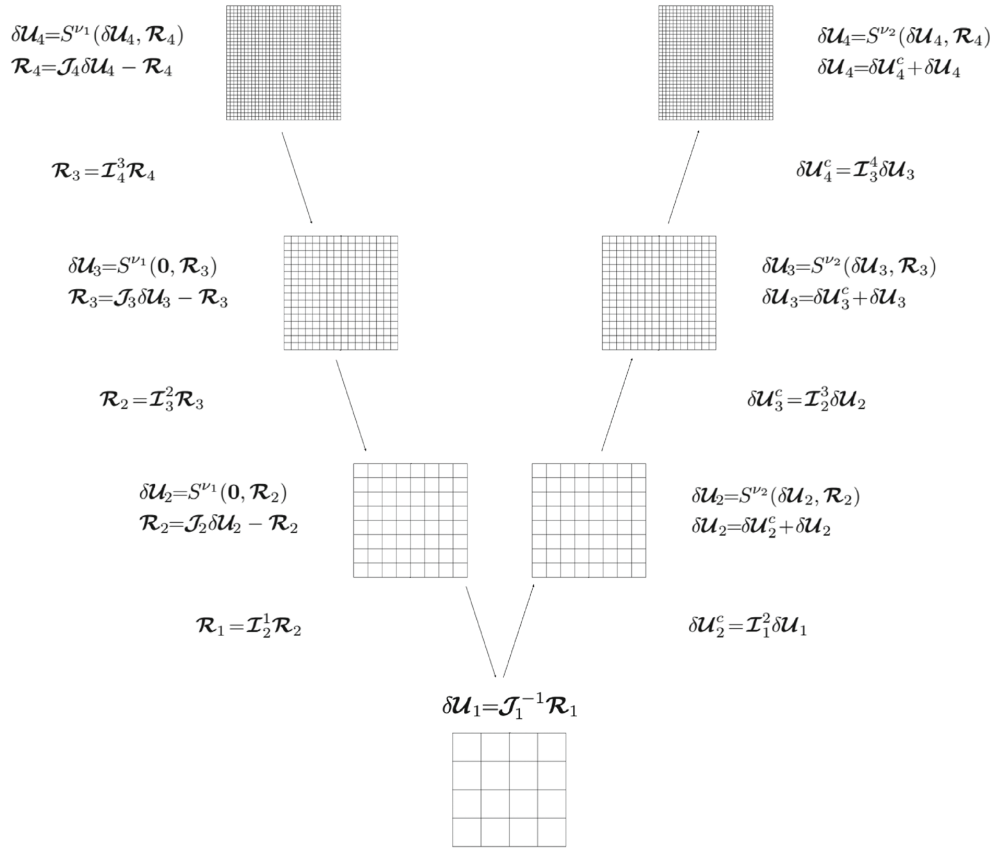

FIGURE 3 | V-cycle schema: Schematic description of V-cycle Multigrid for four levels mesh refinement.

The intergrid transfer operators are done in geometric context for the FEM discretization choice, Q_2 and P_1^{disc}. We proceed, in Section 4.2, with intergrid transfer operators, and in Section 4.3 with smoothing steps via local pressure Schur complement.

4.2 | Grid Transfer Operators

Multigrid method requires intergrid transfer operators mapping data between the grid hierarchy $\mathcal{T}_{h_k}$ and $\mathcal{T}_{h_{k-1}}$. We are using *geometric transfer between FE spaces*. The coarse-to-fine grid (prolongation) operator $\mathcal{I}_{k-1}^{k}$ maps functions defined on the coarser grid level $k-1$ into functions defined on a finer grid level k, while the fine-to-coarse grid (restriction) operator $\mathcal{I}_{k}^{k-1}$ maps functions defined on the finer grid level k into functions defined on a coarser grid level $k-1$.

$$\mathcal{I}_{k-1}^{k} = \left(\mathcal{I}_{k-1,k}^{\tilde{\mathbf{u}}}, \mathcal{I}_{k-1,k}^{p}\right) : \mathbb{W}_{h_{k-1}} \times \mathbb{Q}_{h_{k-1}} \rightarrow \mathbb{W}_{h_k} \times \mathbb{Q}_{h_k}, \tag{36}$$

$$\mathcal{I}_{k}^{k-1} = \left(\mathcal{I}_{k,k-1}^{\tilde{\mathbf{u}}}, \mathcal{I}_{k,k-1}^{p}\right) : \mathbb{W}_{h_k} \times \mathbb{Q}_{h_k} \rightarrow \mathbb{W}_{h_{k-1}} \times \mathbb{Q}_{h_{k-1}}. \tag{37}$$

4.2.1 | Grid Transfer Operators $\mathcal{I}_{k-1,k}^{\tilde{\mathbf{u}}}$ and $\mathcal{I}_{k,k-1}^{\tilde{\mathbf{u}}}$

Microstructure and velocity are approximated with conforming biquadratic finite elements. Thus, the finite element space on a coarser level is a subspace of the finite element space on a finer level $\mathbb{W}_{h_{k-1}} \subset \mathbb{W}_{h_k}$ ($k \geq 1$). Therefore, the prolongation operator $\mathcal{I}_{k-1,k}^{\tilde{\mathbf{u}}}$ is the natural embedding of $\mathbb{W}_{h_{k-1}}$ into $\mathbb{W}_{h_k}$ in $L^2(\Omega)$. Furthermore, any coarse grid function $\tilde{\mathbf{u}}_{k-1} \in \mathcal{W}_{k-1}$ can be expressed in terms of fine grid basis functions

$$\tilde{\mathbf{u}}_{k-1} = \sum_{j=1}^{\mathtt{dim}\mathbb{W}_{h_{k-1}}} \tilde{\mathbf{u}}_{j,k-1}\varphi_j^{k-1} = \sum_{j=1}^{\mathtt{dim}\mathbb{W}_{h_k}} \tilde{\mathbf{u}}_{j,k}\varphi_j^{k}. \tag{38}$$

Using the dual basis, $\left\{\mathcal{N}_i^k, i = 1, \ldots, \mathtt{dim}\mathbb{W}_{h_k}\right\}$, associated with the basis $\left\{\varphi_i^k, i = 1, \ldots, \mathtt{dim}\mathbb{W}_{h_k}\right\}$ of FE space $\mathbb{W}_{h_k}$, that is,

$$\mathcal{N}_j^k\left(\varphi_i^k\right) = \delta_{ij}, \forall i, j = 1, \ldots, \mathtt{dim}\mathbb{W}_{h_k}, \tag{39}$$

where δ_{ij} is the Kronecker delta function, we get

$$\tilde{\mathbf{u}}_{i,k} = \sum_{j=1}^{\mathtt{dim}\mathbb{W}_{h_{k-1}}} \tilde{\mathbf{u}}_{j,k-1}\mathcal{N}_j^k\left(\varphi_i^{k-1}\right). \tag{40}$$

The entries of its matrix representation $\mathcal{I}_{k-1,k}^{\tilde{\mathbf{u}}} \in \mathcal{W}_k \times \mathcal{W}_{k-1}$ are the coarse grid shape functions evaluated at the fine-grid vertices,

$$\left[\mathcal{I}_{k-1,k}^{\tilde{\mathbf{u}}}\right]_{ij} = \mathcal{N}_j^k\left(\varphi_i^{k-1}\right). \tag{41}$$

We use the L^2-projection for the restriction operator, $\mathcal{I}_{k,k-1}^{\tilde{\mathbf{u}}}$, the fine-to-coarse grid mapping for microstructure and velocity. Its matrix representation, $\mathcal{I}_{k,k-1}$ w.r.t. the basis $\left\{\varphi_i^{k-1}, i = 1, \ldots, \mathtt{dim}\mathbb{W}_{h_{k-1}}\right\}$ and $\left\{\varphi_i^{k}, i = 1, \ldots, \mathtt{dim}\mathbb{W}_{h_k}\right\}$ is obtained using the embedding $\mathcal{I}_{k-1}^{k}$ as follows

$$\mathcal{I}_{k,k-1}^{\tilde{\mathbf{u}}} = \mathbf{M}_{k-1}^{-1}\left(\mathcal{I}_{k-1,k}^{\tilde{\mathbf{u}}}\right)^T \mathbf{M}_k, \tag{42}$$

where $\mathbf{M}_{k-1}$, and $\mathbf{M}_k$ are mass matrices at level $k-1$, and k, respectively. Therefore, the transpose of the prolongation matrix is indeed the restriction matrix

$$\begin{aligned}\boldsymbol{\mathcal{R}}_{k-1} &= \mathbf{M}_{k-1}\mathcal{R}_{k-1}\\ &= \mathbf{M}_{k-1}\left(\boldsymbol{\mathcal{I}}^{\tilde{\mathbf{u}}}_{k-1,k}\right)^T\mathcal{R}_k\\ &= \mathbf{M}_{k-1}\mathbf{M}_{k-1}^{-1}\left(\boldsymbol{\mathcal{I}}^{\tilde{\mathbf{u}}}_{k-1,k}\right)^T\mathbf{M}_k\mathcal{R}_k\\ &= \left(\boldsymbol{\mathcal{I}}^{\tilde{\mathbf{u}}}_{k-1,k}\right)^T\boldsymbol{\mathcal{R}}_k.\end{aligned} \tag{43}$$

The coarse grid matrix can be expressed in terms of the fine grid matrix as follows

$$\boldsymbol{\mathcal{J}}^{\tilde{\mathbf{u}}}_{k-1} = \left(\boldsymbol{\mathcal{I}}^{\tilde{\mathbf{u}}}_{k-1,k}\right)^T\boldsymbol{\mathcal{J}}^{\tilde{\mathbf{u}}}_k\,\boldsymbol{\mathcal{I}}^{\tilde{\mathbf{u}}}_{k-1,k}. \tag{44}$$

It is worth mentioning, that there is no need for the evaluation of neither the mass matrix M_{k-1} nor its inversion.

4.2.2 | Grid Transfer Operators $\boldsymbol{\mathcal{I}}^p_{k-1,k}$ and $\boldsymbol{\mathcal{I}}^p_{k,k-1}$

The pressure is approximated by discontinuous linear finite element, P_1^{disc}. Therefore, the multilevel FE approximation spaces for the pressure are nested, $\mathbb{Q}_{h_{k-1}} \subset \mathbb{Q}_{h_k}$. The prolongation operator for the pressure, $\mathcal{I}^p_{k-1,k}$, is a simple interpolation that we define in terms of the local L^2-inner product projection operator; for all $q \in P_1^{\text{disc}}(K)$ there holds $q \in P_1^{\text{disc}}(\sigma_l(K))\left(l = 1,\cdots,2^d\right)$. Then,

$$\sum_{l=1}^{2^d}\int_{\sigma_l(K)}\mathcal{I}^p_{k-1,k}p_{k-1}q\,d\Omega = \int_K p_{k-1}q\,d\Omega, \quad \forall K \in \mathcal{T}_{h_{k-1}}. \tag{45}$$

Its matrix representation is given in terms of the mass matrices w.r.t. the basis of $\mathbb{Q}_{h_k}$ and $\mathbb{Q}_{h_{k-1}}$ as follows

$$\boldsymbol{\mathcal{I}}^p_{k-1,k} = \mathbf{M}_k^{-1}\Sigma^{\mathrm{T}}\mathbf{M}_{k-1}, \tag{46}$$

where, $\Sigma = \left[diag\left(\Sigma_K\right)\right]_{K\in\mathcal{T}_{h_{k-1}}}$ is a diagonal block matrix with $\Sigma_K := \left[\mathbf{I}_{3\times3},\mathbf{I}_{3\times3},\mathbf{I}_{3\times3},\mathbf{I}_{3\times3}\right]$, and $\mathbf{I}_{3\times3}$ denotes the 3×3 identity matrix. Indeed, let a coarse grid function $p_{k-1} \in \mathcal{Q}_k$, be expressed in terms of fine grid basis functions

$$p_{k-1} = \sum_{j=1}^{\mathtt{dim}\mathbb{Q}_{h_{k-1}}} p_{j,k-1}\psi_j^{k-1} = \sum_{j=1}^{\mathtt{dim}\mathbb{Q}_{h_k}} p_{j,k}\psi_j^k. \tag{47}$$

For each element $K \in \mathcal{T}_{h_{k-1}}$ and each basis function ψ_i^k of $P_1^{\text{disc}}(K)$, we have

$$\sum_{j=1}^{\mathtt{dim}P_1^{\text{disc}}} p_{j,k-1}\int_{\sigma_l(K)}\psi_j^{k-1}\psi_i^k\,d\Omega = \sum_{j=1}^{\mathtt{dim}P_1^{\text{disc}}} p_{j,k}\int_{\sigma_l(K)}\psi_j^k\psi_i^k\,d\Omega, \quad \forall l = 1,\cdots,2^d. \tag{48}$$

Summing-up over the subelements, $\sigma_l(K)\left(l = 1,\cdots,2^d\right)$, there holds

$$\sum_{j=1}^{\mathtt{dim}P_1^{\text{disc}}} p_{j,k-1}\int_K\psi_j^{k-1}\psi_i^k\,d\Omega = \sum_{l=1}^{2^d}\sum_{j=1}^{\mathtt{dim}P_1^{\text{disc}}} p_{j,k}\int_{\sigma_l(K)}\psi_j^k\psi_i^k\,d\Omega. \tag{49}$$

Hence, using the fact that $\psi_i^k = \psi_i^{k-1}$ on $P_1^{\text{disc}(K)}$, there holds

$$\mathbf{M}_{k-1}p_{k-1|K} = \sum_{l=1}^{2^d}\mathbf{M}_k p_{k|\sigma_l(K)}, \tag{50}$$

we use the matrix Σ_K to obtain on each K

$$\mathbf{M}_{k-1}p_{k-1|K} = \Sigma_K\mathbf{M}_k p_{k|K}, \tag{51}$$

we get the fine mesh coefficient vector, p_k, via the local mass matrices, and deduce the matrix prolongation for the pressure (46).

Similarly, the restriction operator for the pressure, $\mathcal{I}^p_{k,k-1}$, is the "L^2-transpose" counterpart of the prolongation. For all $K \in \mathcal{T}_{h_{k-1}}$ and $q \in P_1^{\text{disc}}(K)$

$$\int_K\mathcal{I}^p_{k,k-1}p_k q\,d\Omega = \sum_{l=1}^{2^d}\int_{\sigma_l(K)}p_k\,\mathcal{I}^p_{k-1,k}q\,d\Omega. \tag{52}$$

Here, using the fact that $\psi_j^k = \psi_j^{k-1}$ on $P_1^{\text{disc}(K)}$, there holds once again the Formula (51). The prolongation matrix representation is given in terms of the mass matrices w.r.t. the basis of $\mathbb{Q}_{h_k}$ and $\mathbb{Q}_{h_{k-1}}$ as follows

$$\boldsymbol{\mathcal{I}}^p_{k,k-1} = \mathbf{M}_{k-1}^{-1}\Sigma\mathbf{M}_k, \tag{53}$$

which can be interpreted as the mean averaging of mesh coefficient vector p_k to obtain the mesh coefficient vector p_{k-1}.

4.3 | Local Pressure Schur Complement Approach

Local Pressure Schur complement schemes are generalization of Vanka-type smoothers for coupled systems (33) of saddle point type. They are simple iterative relaxation methods that solve directly on element level, one element or a patch of elements, and perform an outer block Gauss–Seidel iterations.

The Pressure Schur Complement, assuming non-singularity of $\mathbf{A}_{\tilde{\mathbf{u}}}$, raises from block Gaussian elimination of the 2×2 block matrix, which leads to the LDU block factorization

$$\mathcal{J} = \begin{pmatrix}\mathbf{I}_{\tilde{\mathbf{u}}} & \mathbf{O}\\ \mathbf{B}\mathbf{A}_{\tilde{\mathbf{u}}}^{-1} & \mathbf{I}_p\end{pmatrix}\begin{pmatrix}\mathbf{A}_{\tilde{\mathbf{u}}} & \mathbf{O}\\ \mathbf{O}_{\tilde{\mathbf{u}}}^{-1} & \mathcal{S}_p\end{pmatrix}\begin{pmatrix}\mathbf{I}_{\tilde{\mathbf{u}}} & \mathbf{A}_{\tilde{\mathbf{u}}}^{-1}\mathbf{B}^{\mathrm{T}}\\ \mathbf{O} & \mathbf{I}_p\end{pmatrix} \tag{54}$$

where $\boldsymbol{\mathcal{S}} = -\mathbf{B}\mathbf{A}_{\tilde{\mathbf{u}}}^{-1}\mathbf{B}^{\mathrm{T}}$ denotes the Schur complement of $\boldsymbol{\mathcal{J}}$. Since $\mathbf{B}$ has full rank, with our discretization choice, the Schur complement $\boldsymbol{\mathcal{S}}$ is invertible, and so is the matrix $\boldsymbol{\mathcal{J}}$. In order to not compromise the precondition for the nonlinearity convergence on the one hand, and to keep the inverting matrices of moderately small size on the other hand, we opt for element-by-element calculation of $\boldsymbol{\mathcal{J}}^{-1}$ using direct solver. It is worth noting that, the element-by-element, or in other word, the local pressure Schur matrices are full, but for only three unknowns, that is, the pressure d.o.f. (Figure 4).

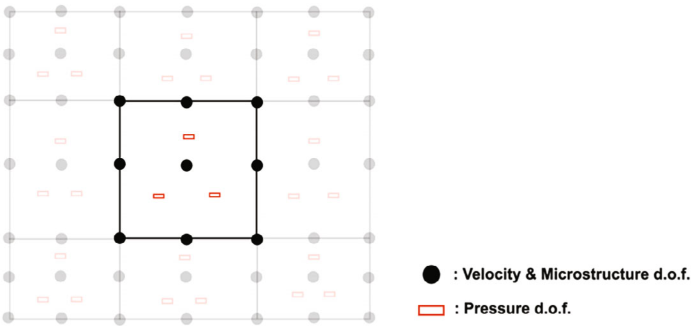

FIGURE 4 | Local degrees of freedom for flow fields. [Colour figure can be viewed at wileyonlinelibrary.com]

We proceed now with the setting of the local subproblems. To do so, we introduce linear prolongation operator

$$\mathcal{P}_K = \left(\mathcal{P}_K^{\tilde{\mathbf{u}}}, \mathcal{P}_K^{p}\right) : \mathcal{W}_h(K) \times \mathcal{Q}_h(K) \to \mathcal{W}_h \times \mathcal{Q}_h \quad \forall K \in \mathcal{T}_h, \tag{55}$$

and the corresponding restriction operator

$$\mathcal{P}_K^{\mathrm{T}} = \left(\mathcal{P}_K^{\tilde{\mathbf{u}}\,\mathrm{T}}, \mathcal{P}_K^{p\,\mathrm{T}}\right) : \mathcal{W}_h \times \mathcal{Q}_h \to \mathcal{W}_h(K) \times \mathcal{Q}_h(K), \quad \forall K \in \mathcal{T}_h. \tag{56}$$

Since the microstructure and the velocity are approximated with conforming Q_2 FE they are lying on the same degree of freedom. Furthermore, using conforming FE approximations, Figure 4, results in an overlapping of corresponding spaces of degrees of freedom $\mathcal{W}_h(K) \forall K \in \mathcal{T}_h$, that is,

$$\forall K \in \mathcal{T}_h, \exists \tilde{K} \in \mathcal{T}_h, \tilde{K} \neq K \mid \mathcal{W}_h(K) \bigcap_{K \neq \tilde{K}} \mathcal{W}_h(\tilde{K}) \neq \emptyset. \tag{57}$$

While using discontinuous FE approximations for the pressure P_1^{disc}, Figure 4, leads to nonoverlapping of spaces of degrees of freedom $\mathcal{Q}_h(K) \forall K \in \mathcal{T}_h$, that is,

$$\mathcal{Q}_h(K) \cap_{K \neq \tilde{K}} \mathcal{Q}_h(\tilde{K}) = \emptyset \quad \forall K, \tilde{K} \in \mathcal{T}_h. \tag{58}$$

Let $\boldsymbol{\mathcal{P}}_K^{\tilde{\mathbf{u}}}, \boldsymbol{\mathcal{P}}_K^{p}$, and $\boldsymbol{\mathcal{P}}_K$ denote matrices representations, that is, the algebraic counterpart of prolongations $\mathcal{P}_K^{\tilde{\mathbf{u}}}, \mathcal{P}_K^{p}$, and $\mathcal{P}_K$, defined on spaces of variables values $\mathcal{W}_K := \mathbb{R}^{\mathtt{dim}\mathbb{W}_K}$, $\mathcal{Q}_K := \mathbb{R}^{\mathtt{dim}\mathbb{Q}_K}$, and $\mathcal{V}_K := \mathcal{W}_K \times \mathcal{Q}_K$, respectively. Thus,

$$\boldsymbol{\mathcal{U}}_K = (\tilde{\mathbf{u}}_K, p_K) := \boldsymbol{\mathcal{P}}_K^{\mathrm{T}} \boldsymbol{\mathcal{U}} = \left(\boldsymbol{\mathcal{P}}_K^{\tilde{\mathbf{u}}\,\mathrm{T}} \tilde{\mathbf{u}}, \boldsymbol{\mathcal{P}}_K^{p\,\mathrm{T}} p\right), \tag{59}$$

$$\boldsymbol{\mathcal{U}} = (\tilde{\mathbf{u}}, p) = \sum_{K \in \mathcal{T}_h} \boldsymbol{\mathcal{P}}_K \boldsymbol{\mathcal{U}}_K = \sum_{K \in \mathcal{T}_h} \left(\boldsymbol{\mathcal{P}}_K^{\tilde{\mathbf{u}}} \tilde{\mathbf{u}}, \boldsymbol{\mathcal{P}}_K^{p} p\right). \tag{60}$$

We calculate the local residuum and local matrices, then we solve the local subproblems of saddle point type to get the local update $\delta \boldsymbol{\mathcal{U}}_K$, followed by the calculation of the global update $\delta \boldsymbol{\mathcal{U}}$, before finally updating the solutions with certain damping parameter ω, as follows;

Local residuum:

$$\boldsymbol{\mathcal{R}}_K(\boldsymbol{\mathcal{U}}) = \boldsymbol{\mathcal{P}}_K^{\mathrm{T}} \boldsymbol{\mathcal{R}}(\boldsymbol{\mathcal{U}}), \tag{61}$$

Local matrices:

$$\boldsymbol{\mathcal{J}}_K(\boldsymbol{\mathcal{U}}) = \boldsymbol{\mathcal{P}}_K^{\mathrm{T}} \boldsymbol{\mathcal{J}}(\boldsymbol{\mathcal{U}}) \boldsymbol{\mathcal{P}}_K. \tag{62}$$

Solve the local subproblems:

$$\boldsymbol{\mathcal{J}}_K(\boldsymbol{\mathcal{U}}) \delta \boldsymbol{\mathcal{U}}_K = \boldsymbol{\mathcal{R}}_K(\boldsymbol{\mathcal{U}}), \tag{63}$$

Calculation of the global update:

$$\delta \boldsymbol{\mathcal{U}} = \sum_{K \in \mathcal{T}_h} \boldsymbol{\mathcal{P}}_K \delta \boldsymbol{\mathcal{U}}_K, \tag{64}$$

Update the solutions:

$$\boldsymbol{\mathcal{U}}^{\mathrm{Update}} = \boldsymbol{\mathcal{U}} - \omega \delta \boldsymbol{\mathcal{U}}. \tag{65}$$

Concisely, the iterations can be written as block Gauss–Seidel iteration

$$\boldsymbol{\mathcal{U}}^{l+1} = \boldsymbol{\mathcal{U}}^{l} - \omega_l \sum_{K \in \mathcal{T}_h} \boldsymbol{\mathcal{P}}_K \left(\boldsymbol{\mathcal{P}}_K^{\mathrm{T}} \boldsymbol{\mathcal{J}}(\boldsymbol{\mathcal{U}}^{l}) \boldsymbol{\mathcal{P}}_K\right)^{-1} \boldsymbol{\mathcal{P}}_K^{\mathrm{T}} \boldsymbol{\mathcal{R}}(\boldsymbol{\mathcal{U}}^{l}). \tag{66}$$

The TVP systems (33) are of saddle point types. While classical smoothers, for instance, point-wise Gauss–Seidel, are not appropriate choices due to the zero block, Local Pressure Schur Complement approach, or cell-based Vanka smoother demonstrate effective performance mainly for systems with the weak coupling of velocity and pressure. Therefore, we maintained its effective performance by preserving the continuity constraint with our choice of discontinuous FE approximations for pressure. As a consequence, the choices of the blocks for the system (33) are based on the pressure degrees of freedom. And due to no coupling between the pressure and microstructure, we collocated the microstructure and velocity in the same degrees of freedom. So, additional communication with the pressure degrees of freedom for thixotropy field is avoided.

This completes the explanation of the two main ingredients of our monolithic Newton-Multigrid FEM solver, that is, the adaptive methodology using discrete adaptive Newton, and the coupled geometric Multogrid using Local Pressure Schur Complement. However, the current state of the solver faces challenges w.r.t additional flow fields (for instance, three-filed formulation for TVP problems, i.e., including TVP stress as a new variable), or the support of high-performance computing. In the next section, we highlight the performance and certain limitations of adaptive Newton-Multigrid FEM solver and present certain alternative fix for further investigations.

5 | Performance and Limitations of Adaptive Discrete Newton-Multigrid Solver

In this section, we aim to spotlight the adaptive Newton-multigrid solver to bear its limitations, success, and possible areas of further investigations.

5.1 | Newton's Step-Length Adaptivity Function and Flow Models

In the current state of our solver, Newton's step-length adaptivity function is only empirical, and it was originally developed for quasi-Newtonian modeling of yield-stress materials. As TVP problems remain in this broad category of yield stress materials, more tests for different types of flows and materials (for instance, Giesekus-type models for viscoelastic materials, $\kappa - \epsilon$ models for turbulent flows, multiphase flows via level set method, and fluid–structure interaction problems) need to be done to check whether this function requires modification or adaptation w.r.t flow models and materials.

5.2 | Computational Complexity and One Possible Fix

The local subproblem (63) is of saddle point type with (30×30)-matrices of the form

$$\mathcal{J}_K = \begin{pmatrix} \mathbf{A}_{u,u} & \mathbf{A}_{u,v} & \mathbf{A}_{u,\lambda} & \mathbf{B}_1^{\mathrm{T}} \\ \mathbf{A}_{v,u} & \mathbf{A}_{v,v} & \mathbf{A}_{v,\lambda} & \mathbf{B}_2^{\mathrm{T}} \\ \mathbf{A}_{\lambda,u} & \mathbf{A}_{\lambda,v} & \mathbf{A}_{\lambda,\lambda} & \mathbf{O} \\ \mathbf{B}_1 & \mathbf{B}_2 & \mathbf{O} & \mathbf{O} \end{pmatrix}. \tag{67}$$

Let us define the $\mathbf{A}_{\mathbf{u}}$, $\mathbf{A}_{(\mathbf{u},\lambda)}$, and $\mathbf{A}_{(\mathbf{u},p)}$ be the submatrices

$$\mathbf{A}_{\mathbf{u}} = \begin{pmatrix} \mathbf{A}_{u,u} & \mathbf{A}_{u,v} \\ \mathbf{A}_{v,u} & \mathbf{A}_{v,v} \end{pmatrix}, \quad \mathbf{A}_{(\mathbf{u},p)} = \begin{pmatrix} \mathbf{A}_{\mathbf{u}} & \mathbf{B}^{\mathrm{T}} \\ \mathbf{B} & \mathbf{O} \end{pmatrix}, \quad \mathbf{A}_{(\mathbf{u},\lambda)} = \begin{pmatrix} \mathbf{A}_{\mathbf{u}} & \mathcal{B}_1^{\mathrm{T}} \\ \mathcal{B}_2 & \mathbf{A}_{\lambda} \end{pmatrix}, \tag{68}$$

where $\mathbf{B} = (\mathbf{B}_1, \mathbf{B}_2)^{\mathrm{T}}$, $\mathcal{B}_1 = \mathbf{A}_{\lambda,\mathbf{u}} = (\mathbf{A}_{\lambda,u}, \mathbf{A}_{\lambda,v})$, and $\mathcal{B}_2 = \mathbf{A}_{\mathbf{u},\lambda} = (\mathbf{A}_{u,\lambda}, \mathbf{A}_{v,\lambda})^{\mathrm{T}}$.

The local pressure Schur Complement matrices $\mathcal{S}_p$, the Schur Complement of $\mathbf{A}_{\mathbf{u}}$ in $\mathbf{A}_{(\mathbf{u},p)}$, involves only the velocity not the microstructure, that is

$$\mathcal{S}_p = -\mathbf{B}\mathbf{A}_{\mathbf{u}}^{-1}\mathbf{B}^{\mathrm{T}}, \tag{69}$$

The Pressure Schur Complement matrices $\mathcal{S}_p$ do not increase the complexity of the microstructure. So, instead of calculating $\mathcal{J}_K^{-1}$ by Gaussian elimination, for instance, one calculates $\mathcal{S}_p^{-1}$ to deduce pressure, and then calculates the velocity and microstructure. Despite the matrix $\mathcal{S}_p$ might be full in general, it involves only the local pressure unknowns [4], which are very small than the total number of unknowns including velocity and microstructure.

A similar technique can be applied to the matrix $\mathbf{A}_{\tilde{\mathbf{u}}} := \mathbf{A}_{(\mathbf{u},\lambda)}$ to not increase the complexity of the problem with additional physical field. Indeed, we use again of the following block factorization

$$\mathbf{A}_{\tilde{\mathbf{u}}} = \begin{pmatrix} \mathbf{I}_{\mathbf{u}} & \mathbf{O} \\ \mathcal{B}_1\mathbf{A}_{\mathbf{u}}^{-1} & \mathbf{I}_{\lambda} \end{pmatrix} \begin{pmatrix} \mathbf{A}_{\mathbf{u}} & \mathbf{O} \\ \mathbf{O} & \mathcal{S}_{\lambda} \end{pmatrix} \begin{pmatrix} \mathbf{I}_{\mathbf{u}} & \mathbf{A}_{\mathbf{u}}^{-1}\mathcal{B}_2^{\mathrm{T}} \\ \mathbf{O} & \mathbf{I}_{\lambda} \end{pmatrix}, \tag{70}$$

where

$$\mathcal{S}_{\lambda} = \mathbf{A}_{\lambda} - \mathcal{B}_1\mathbf{A}_{\mathbf{u}}^{-1}\mathcal{B}_2^{\mathrm{T}}, \tag{71}$$

is the Schur complement, of $\mathbf{A}_{\mathbf{u}}$ in $\mathbf{A}_{\tilde{\mathbf{u}}}$, associated to the microstructure λ. Thus, one here can also calculate $\mathcal{S}_{\lambda}^{-1}$ instead of calculating $\mathbf{A}_{\tilde{\mathbf{u}}}^{-1}$. In doing so, we might preserve the complexity of the problem w.r.t. additional physical fields.

5.3 | Vanka-Type Smoothers and Parallel Computing

Our current version of LPSC uses block Guass–Seidel iterations, which is not suitable for parallel computing. This is a major limitation of the current approach and requires further investigation. One might use instead the block Jacobi iterations in contrast to our adopted Guass–Seidel iteration strategy. In doing so, the block will consist of all unknowns stored on one processor, and after each smoothing iteration, the communication should be done to get the averaged values. As a consequence, communications between processors are avoided during the smoothing process.

After listing some limitations of the current state of our solver, we proceed to explore its performance to build on for further improvement. We intend to show the solver performance in simple relative comparative analysis for the most appealing case study of viscoplastic Bingham cavity flow, using different methods, fixed point method, Newton's method, adaptive continuous method with Jacobian operator splitting on the one hand, and with available reference results from literature on the other hand. Furthermore, in Appendix A, we give an exclusive performance case study for flow around cylinder Benchmark, for Newtonian, power-law, and viscoplastic Bingham models.

5.4 | Analysis of Solver Performance

For our comparative analysis, we use the CC2d-power-law application from FeatFlow[1] software to generate the data for fixed point method, Newton's method, and adaptive continuous Newton with Jacobian operator splitting. The application uses lower-order discretization on quadrilateral $\tilde{Q}_1/Q_0$, rotated bilinear for velocity, and constant for pressure.

In Figures 5 and 6, we display the performance comparison in terms of the residuum convergence and Multigrid convergence rate w.r.t. iterations using fixed point, Newton's method, adaptive continuous Newton's method via Jacobian operator splitting, and adaptive discrete Newton's method via adaptive step-length for yield-stress value $\tau_0 = 2.0$ and $\tau_0 = 5.0$ for successive mesh refinement levels 6, 7, 8, and 9. The corresponding statistic of the performance comparison is classified in terms of number of nonlinear iterations per the average number of Multigrid iterations required for each nonlinear iteration (NL/ANMG) in Table 2.

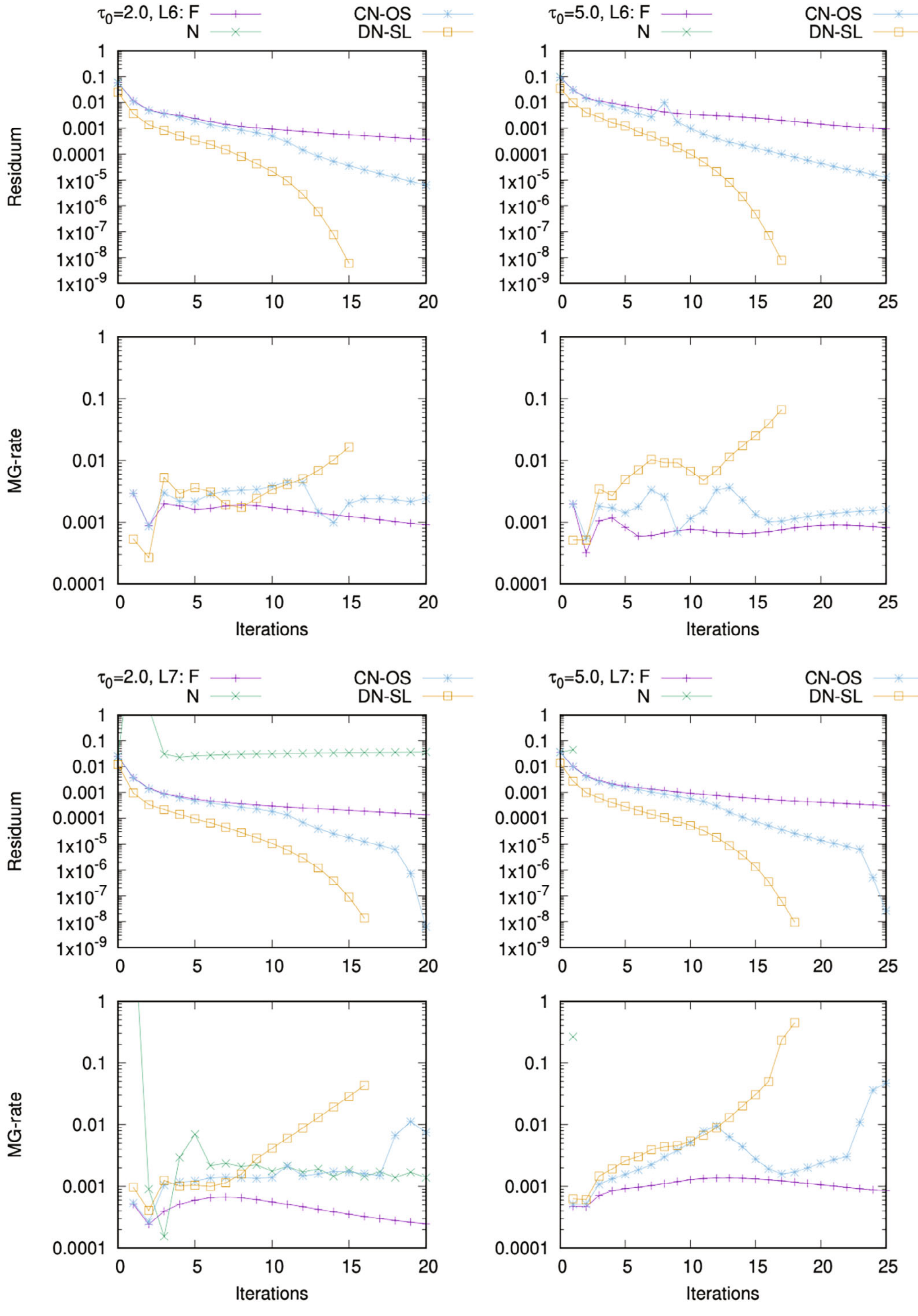

FIGURE 5 | Viscoplastic Bingham flow in lid-driven cavity: Performance comparison in terms of Residuum convergence and Multigrid rate w.r.t. iterations of fixed point, Newton's method, adaptive continuous Newton's method via Jocobian operator splitting CN-OS, and adaptive discrete Newton's method via adaptive step-length DN-SL for successive mesh refinement levels for Bingham viscoplastic flow for yield-stress value $\tau_0 = 2.0$ and $\tau_0 = 5.0$. [Colour figure can be viewed at wileyonlinelibrary.com]

Despite the FEM order discrepancy in the discretization used in the comparative study shown in Figures 5 and 6, and Table 2, the study approve the opted strategy of the adaptive discrete Newton's method via adaptive step-length. Indeed, the adaptive discrete Newton's via step-length follows the convergence path of fixed point method, and the adaptive continuous Newton's method via Jacobian operator splitting, and discards the singularity of the "exact" accurate approximation of Jacobian, which is indicated by the divergence of Newton's method.

Concerning Multigrid, the convergence rate remains in the accepted range, even if it is increasing as the solver approaches the solution and for the very finest refinement level, which is bearable as the nonlinear rate is decreasing. It is worth noting that

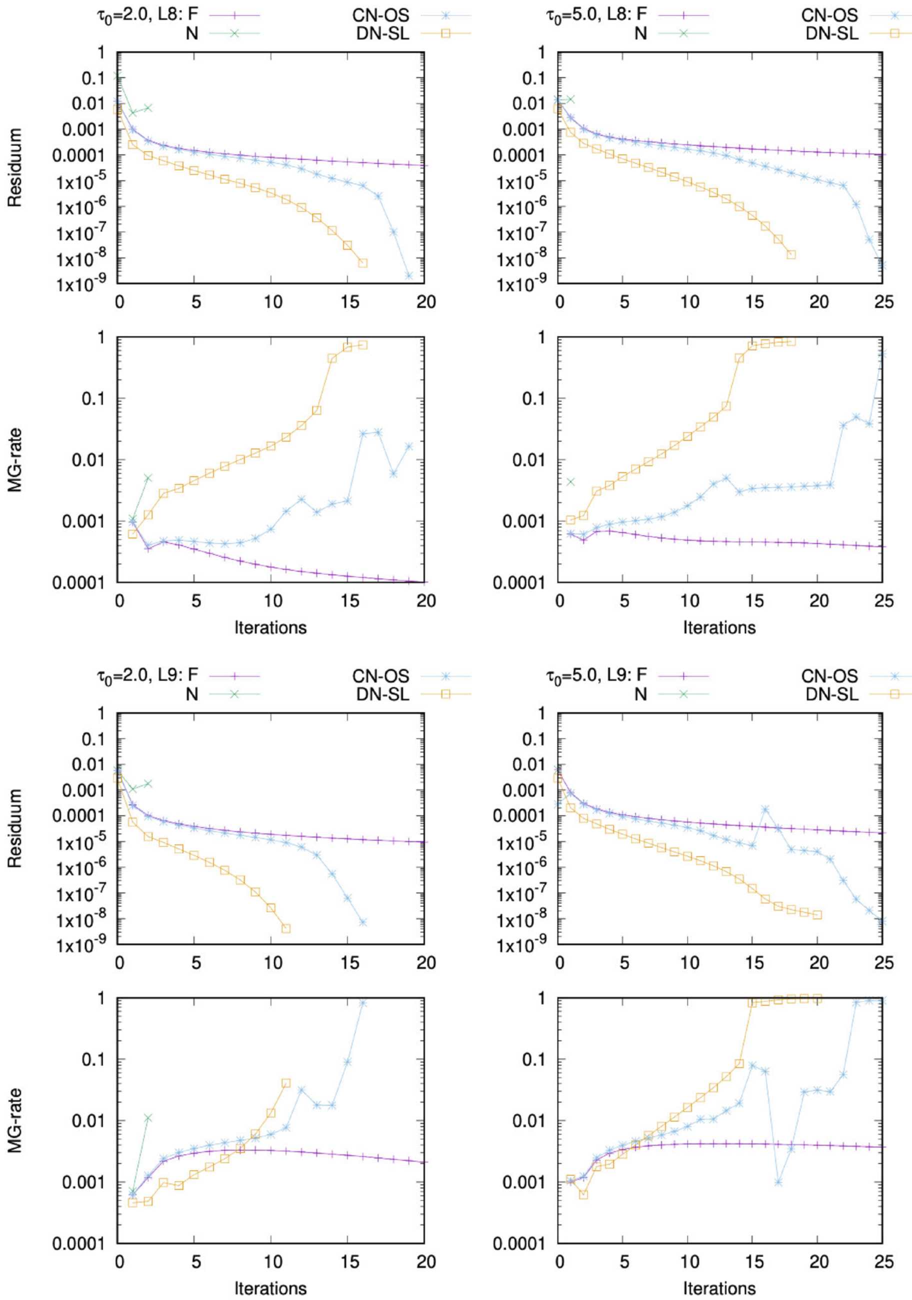

FIGURE 6 | Viscoplastic Bingham flow in lid-driven cavity: Performance comparison in terms of Residuum convergence and Multigrid rate w.r.t. iterations of fixed point, Newton's method, adaptive continuous Newton's method via operator splitting CN-OS, and adaptive discrete Newton's method via step-length DN-SL for successive mesh refinement levels for Bingham viscoplastic flow for yield-stress value $\tau_0 = 2.0$ and $\tau_0 = 5.0$. [Colour figure can be viewed at wileyonlinelibrary.com]

TABLE 2 | Viscoplastic Bingham flow in lid-driven cavity: Statistic of the performance comparison, of fixed point method, Newton's method, adaptive continuous Newton's method via operator splitting CN-OS, and adaptive discrete Newton's method via step-length DN-SL for successive mesh refinement levels for Bingham viscoplastic flow for yield-stress value $\tau_0 = 2.0$ and $\tau_0 = 5.0$.

	$\tau_0 = 2.0$				$\tau_0 = 5.0$			
	Fixed point	**Newton**	**Adaptive**		**Fixed point**	**Newton**	**Adaptive**	
Level			**CN-OS**	**DN-SL**			**CN-OS**	**DN-SL**
6	*40/1	—	20/1	15/1	*40/1	—	31/1	17/1
7	*40/1	—	18/1	16/1	*40/1	—	26/1	18/1
8	*40/1	—	18/1	16/2	*40/1	—	25/1	18/2
9	*40/1	—	15/2	15/3	*40/1	—	25/2	20/4

for these case studies, we used standard Multigrid, and allowed only for one-digit gain for both linear and nonlinear solvers. Alternatively, an adaptive Multigrid w.r.t. nonlinear rate can be activated.

We continue the detailed analysis of the solver behavior by displaying the residuum, Multgrid rate, nonlinear rate, and the step-length update, during the convergence process w.r.t. mesh refinement, and regularization parameters $k = 10^2$, and $k = 10^3$ for yield stress parameters $\tau_0 = 2.0$, and $\tau_0 = 5.0$ in Figure 7, and w.r.t. mesh refinement, and nonlinearity in terms of yield stress parameter $\tau_0 = 2.0$, $\tau_0 = 5.0$, and $\tau_0 = 2.0$, $\tau_0 = 20.0$ for regularization parameter $k = 10^3$ in Figure 8.

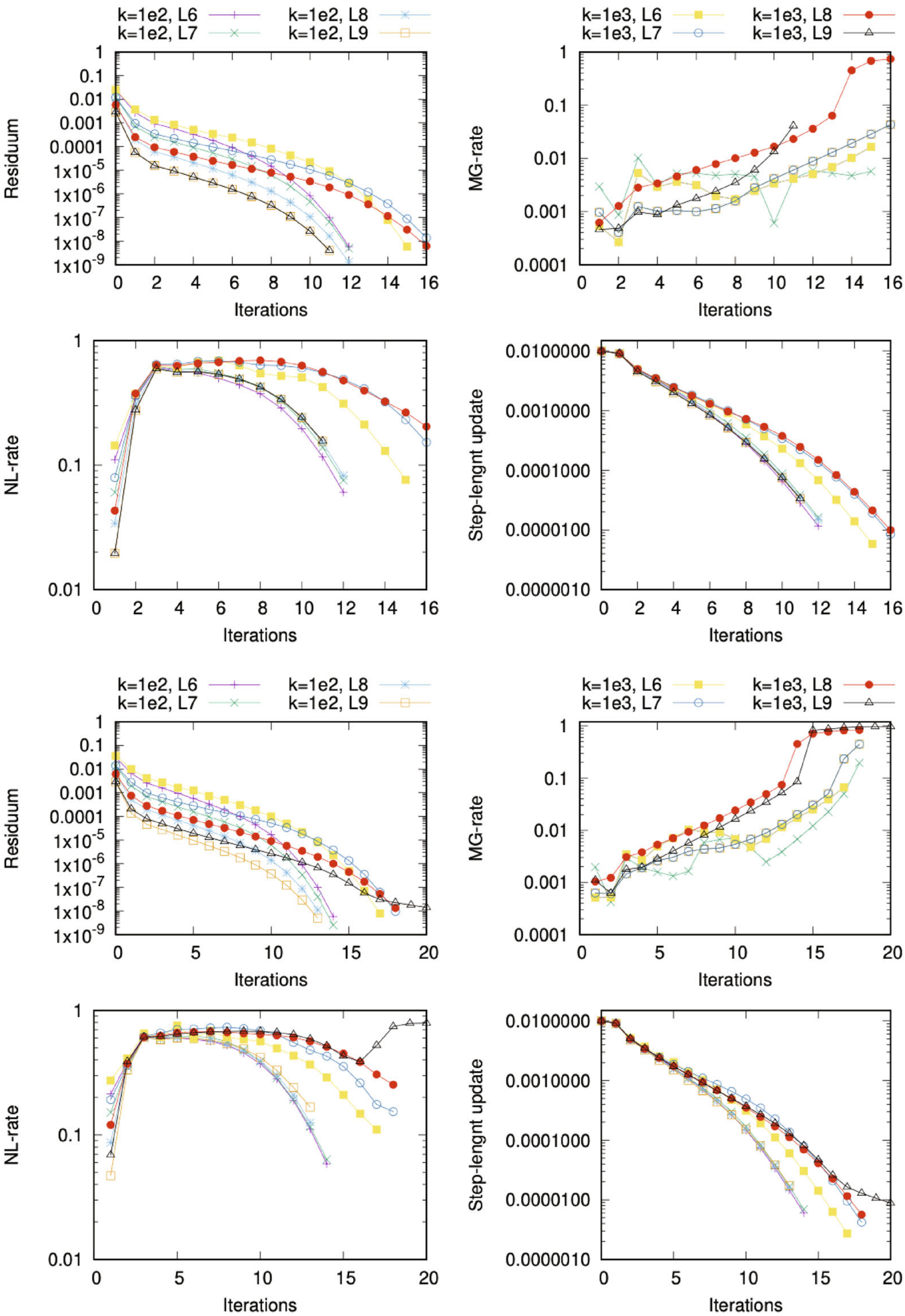

FIGURE 7 | Adaptive discrete Newton via step-length for viscoplastic Bingham Cavity flow: Solver behavior, Residuum, Multgrid rate, Nonlinear rate, and the step-length update, during the convergence process for Bingham flow w.r.t. mesh refinement, and regularity parameter $k = 10^2$ and $k = 10^3$ for yield stress parameters $\tau = 2.0$ (top) and $\tau = 5.0$ (bottom). [Colour figure can be viewed at wileyonlinelibrary.com]

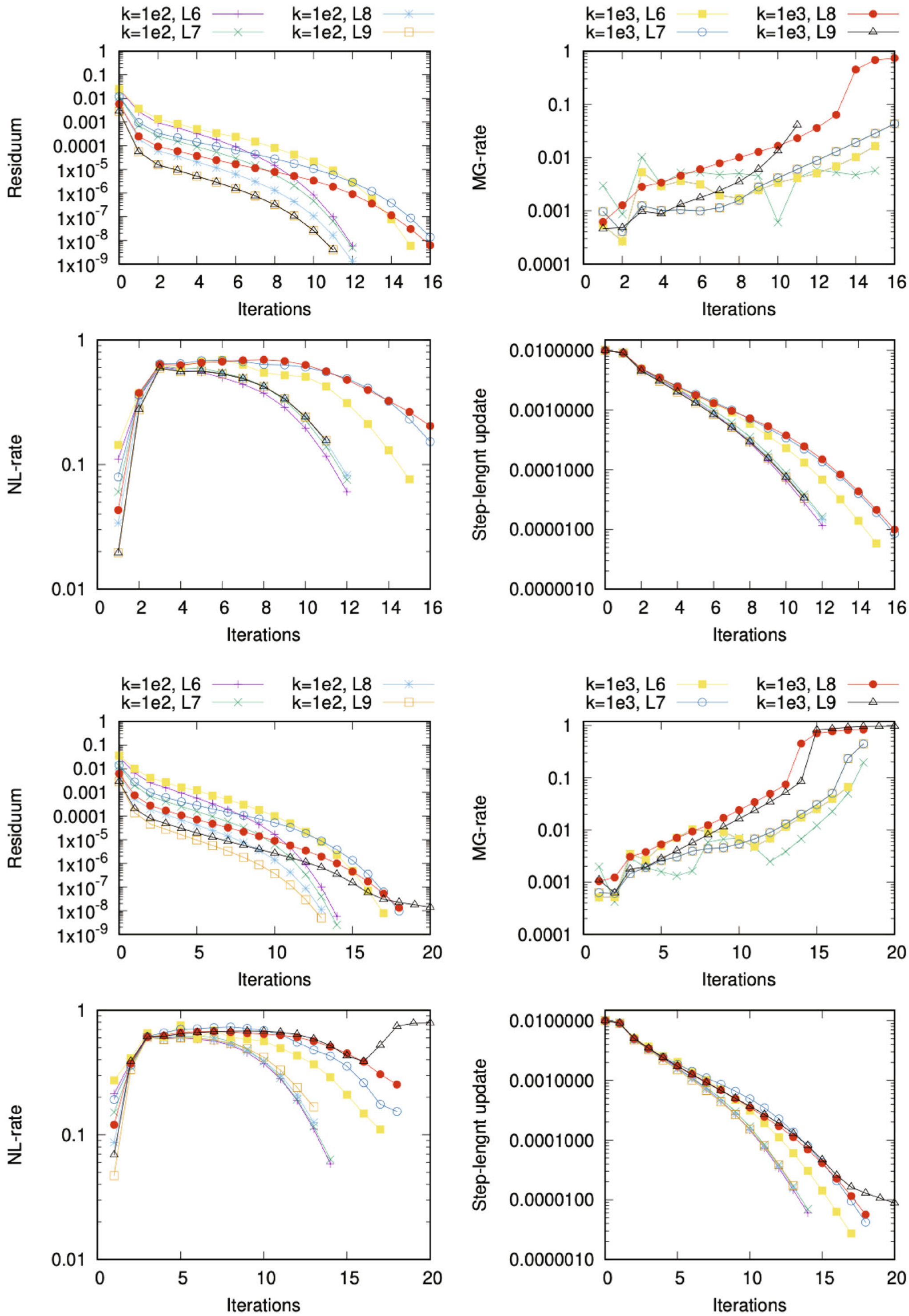

FIGURE 8 | Adaptive discrete Newton via step-length for viscoplastic Bingham Cavity flow: Solver behavior, Residuum, Multgrid rate, Nonlinear rate, and the step-length update, during the convergence process for Bingham flow w.r.t. mesh refinement, and nonlinearity in term of yield stress parameter, that is, for yield stress parameters $\tau = 2.0$, and $\tau = 5.0$ (top), and for yield stress parameters $\tau = 2.0$ and $\tau = 20.0$ (bottom). [Colour figure can be viewed at wileyonlinelibrary.com]

From the displayed results in Figures 7 and 8, the residuum is converging for all cases with an accepted range for Multigrid rate. Moreover, the step-length update, as a function of the nonlinear rate, decreases with a rate in perfect accordance with the residuum convergence rate, which confirms the feedback character of the nonlinear rate for the well-defined Jacobian. Once again, the Multigrid is far from being bulletproof; its convergence rate is increasing inversely with the nonlinear convergence rate, indicating the need for a good precondition for the smoother with more optimal complexity.

We list the statistic of the performance of adaptive discrete Newton's method via step-length solver versus available results from literature for successive mesh refinement levels, yield-stress

TABLE 3 | Viscoplastic Bingham flow in lid-driven cavity: Statistic of the performance of the adaptive discrete Newton's method via step-length DN-SL for Bingham viscoplastic flow in terms of number of nonlinear iteration iterations, and the average number of multigrid required for one nonlinear iteration (NL/ANMG) w.r.t. successive mesh refinement levels, yield-stress value $\tau_0 = 2.0$, $\tau_0 = 5.0$, and $1\tau_0 = 20.0$, and regularization parameter $k = 10^2$ and 10^3, with available results from literature.

	$\tau_0 = 2.0$				$\tau_0 = 5.0$				$\tau_0 = 20.0$
	DN-SL present		Dual from [26]		DN-SL present		Dual from [26]		DN-SL present
	k		ϵ		k		ϵ		k
Level	10^2	10^3	10^{-2}	10^{-3}	10^2	10^3	10^{-2}	10^{-3}	10^3
6	13/1	12/1	12	12	13/1	12/1	17	18	21/1
7	12/1	11/1	9	9	13/1	12/1	13	14	24/2
8	11/1	11/1	—	—	11/1	11/1	—	—	23/3
9	11/1	10/1	—	—	11/1	11/1	—	—	20/4

$$u = \begin{cases} \frac{1}{8}\left((1-2\tau_0)^2 - (1-2\tau_0-2y)^2\right) & \text{if } y \in [0, \frac{1}{2} - \tau_0) \\ \frac{1}{8}(1-2\tau_0)^2 & \text{if } y \in [\frac{1}{2} - \tau_0, \frac{1}{2} + \tau_0] \\ \frac{1}{8}\left((1-2\tau_0)^2 - (2y-2\tau_0-1)^2\right) & \text{if } y \in (\frac{1}{2} + \tau_0, 1] \end{cases}$$

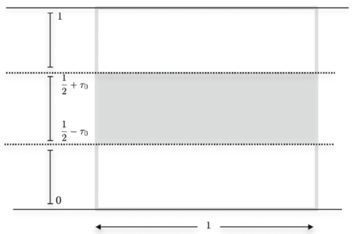

FIGURE 9 | Bingham viscoplastic benchmark: Analytic Bingham viscoplastic velocity solution (left), and the corresponding yielded (unshaded) and unyielded (shaded) zones distribution (right) w.r.t. yield stress parameter.

value $\tau_0 = 2.0$, $\tau_0 = 5.0$, and $\tau_0 = 20.0$, and regularization parameter $k = 10^2$, and 10^3 in Table 3.

The reader can check the reference [26] for other results, and we included the ones that reach moderate refinement levels, despite the loose stopping criterion.

We proceed with the analysis of the performance of the solver w.r.t. different boundary conditions settings and regularization parameters in a single test example in Section 5.5.

5.5 | Regularization and Type of BCs Investigations

The important issue of the performance of the solver w.r.t. regularization parameter and different types of boundary conditions settings is dispersed throughout different flow problems. Indeed, the lid-driven cavity flow problem (Sections 5.4 and 6) consider solely the continuous Dirichlet BCs, the 4:1 contraction (Section 7) uses discrete data as Dirichlet BCs instead of pressure drop BCs with the help of the double gate mechanism to the reduced one-dimensional model (Section 7.1), and the flow around cylinder benchmark (section A) uses both Dirichlet BCs and Neumann BCs. To gather the analysis of this important issue of the solver performance w.r.t. different BCs settings in a single test example, we consider the classical analytical Bingham viscoplastic benchmark on unity channel. It is shown in [27] that this benchmark allows for different boundary conditions settings, that is Dirichlet BCs as well as pressure drop BCs.

The classical analytical Bingham viscoplastic benchmark consists of a yield stress-dependent analytic function $\boldsymbol{u}_{ex} = (u, 0)^{\mathrm{T}}$ on unit channel Figure 9, leading to an unyielded region located along the center of the channel with the width dependent on yield stress parameter τ_0, that is, $y \in \left[\frac{1}{2} - \tau_0, \frac{1}{2} + \tau_0\right]$.

The analytical solution Figure 9 as Dirichlet BCs settings, the pressure solution presents discontinuity between the yield zone, Poiseuille law, that is, $\nabla p = -1$, and constant pressure in the unyielded zone, that is, $\nabla p = 0$. While the pressure solution with the pressure drop BCs settings leads to no discontinuity between yielded and unyielded zones, the pressure solution is linear in both zones with $\nabla p = -1$, see [27]. So, in order to balance this discrepancy between the pressure solutions of Dirichlet BCs and pressure drop BCs settings, we further impose a force term in the unyielded zone for the Dirichlet BCs case, that is $(-1, 0)^{\mathrm{T}}$ for $y \in \left[\frac{1}{2} - \tau_0, \frac{1}{2} + \tau_0\right]$. Figure 10 presents the corresponding solution for flow fields, pressure, velocity, and shear rate for both boundary conditions settings. And, in Table 4, we present the statistics of solver behavior w.r.t mesh refinement in terms of the nonlinear iterations, and the average number of multigrid iterations (NL/ANMG) for the set of regularization parameter k set $\{10^1, 10^2, 10^3, 10^4, 10^5, 10^6\}$.

With the different boundary settings, Dirichlet BCs with the nonhomogeneous force and pressure drop BCs, the flow fields solution for Bingham benchmark coincide as shown in Figure 10. Consequently, this case study gives credibility to the comparative analysis of the solver behavior w.r.t. different boundary settings. Table 4 confirms once again, for both boundary settings with a noticeable close behavior in terms of NL/ANMG, that the nonlinear iterations sweeps increase w.r.t. the increase of the

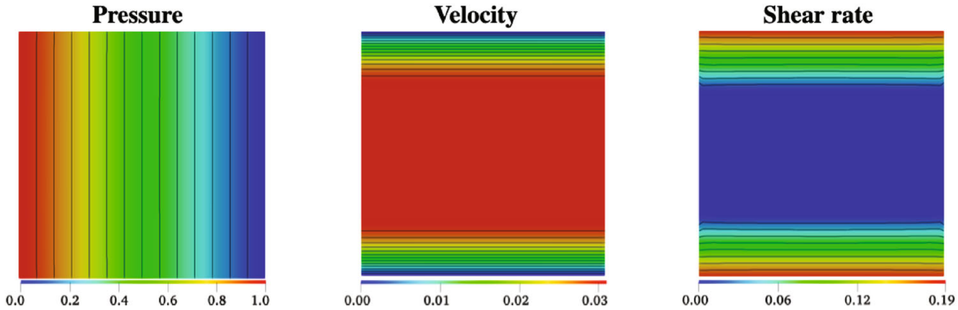

FIGURE 10 | Bingham viscoplastic benchmark: Flow solutions for Dirichlet BCs with nonhomogenuous force in the unyielded region, $(-1,0)^{\mathrm{T}}$ for $y \in \left[\frac{1}{2}-\tau_0, \frac{1}{2}+\tau_0\right]$, and pressure drop BCs, where $\eta_0 = 1.0$ and $\tau_0 = 0.25$. [Colour figure can be viewed at wileyonlinelibrary.com]

TABLE 4 | Bingham viscoplastic benchmark: Solver's performance statistic w.r.t. different boundary conditions settings, that is Dirichlet BCs with nonhomogenuous force in the unyielded region, $(-1,0)^{\mathrm{T}}$ for $y \in \left[\frac{1}{2}-\tau_0, \frac{1}{2}+\tau_0\right]$, pressure drop BCs, and regularization parameter k set $\{10^1, 10^2, 10^3, 10^4, 10^5, 10^6\}$, for $\eta_0 = 1.0$, yield-stress value $\tau_0 = 0.25$.

	Dirichlet BCs						Pressure drop BCs					
	k						k					
Level	10^1	10^2	10^3	10^4	10^5	10^6	10^1	10^2	10^3	10^4	10^5	10^6
2	2/1	10/1	10/1	14/1	18/1	22/1	2/1	12/1	14/1	16/1	18/1	20/1
3	2/1	10/1	10/1	14/1	18/1	18/1	2/1	10/1	14/1	16/1	16/1	14/1
4	3/1	9/1	12/1	16/2	18/2	20/2	3/1	10/1	12/1	16/2	17/2	20/2
5	2/1	8/1	10/2	16/3	20/3	26/4	3/1	10/2	12/2	14/3	16/3	25/4
6	3/1	8/1	10/2	17/3	22/3	27/4	3/1	10/2	12/2	14/3	16/3	28/4

regularization parameter k, which is intended for the clarity of the comparison by deactivating the continuation process w.r.t. regularization parameter. Furthermore, the nonlinear solver via the number of nonlinear iterations remains stable for each and every regularization parameter k w.r.t. the mesh refinement, which is direct consequence of the robustness and the flexibility of the linear Multigrid solver to provide the optimal accuracy required for the nonlinear solver. It is worth to note that the number of linear Multigrid iterations is almost independent of mesh refinement and regularization parameters.

The mechanism of our solver is clarified, and we proceed to investigate numerically the accuracy, robustness, and efficiency of TVP monolithic Newton-Multigrid solver in Section 6. We focus our numerical investigation on lid-driven cavity configuration for Houska's material model from Table 1.

6 | Numerical Results and Discussions

Lid-driven cavity flow represents an academic standard benchmark for incompressible CFD codes. Therefore, we present the corresponding Newton-Multigrid solver behavior results for Newtonian, viscoplastic, and TVP flows. Furthermore, this problem is accepted as a test configuration to check point-wise mesh convergence for velocity for Newtonian flow despite the lack of regularity due to the pressure singularity in the corners of the upper-lid. Hence, we use it in the same context to investigate the point-wise convergence w.r.t. regularization for TVP flow. We consider the classical lid-driven cavity settings on unity square for our analysis. The flow is generated with the moving of the upper lid with x-velocity set to unity, which comes into contact with the stationary walls. That is, the flow problem is subject to nonhomogeneous Dirichlet boundary conditions for x-velocity at the upper boundary wall, and homogeneous Dirichlet boundary conditions at the other walls. The next subsection is devoted to Newtonian lid-driven cavity flow.

6.1 | Newtonian Flow in Lid-Driven Cavity

We use Newtonian lid-driven cavity flow benchmark to validate our numerical method and simulation algorithm. Besides the global quantity, it provided us with a point-wise benchmark, in terms of cutline solutions, and well-studied vortices, with respect to the Reynolds number. The global accuracy of the approximation that consists of the L_2-norm of the velocity is investigated using the kinetic energy. On the other hand, the point-wise accuracy is investigated using the velocity magnitude at the vertical center-line beside the primary vortex and the lower left secondary vortex. In order to check the solver convergence, we list in Table 5 the kinetic energy, $\frac{1}{2}\int_\Omega ||\boldsymbol{u}||^2\,dx$, and Newton-Multigrid convergence behavior, which means the number of nonlinear iterations versus the average number of Multigrid sweeps (N/M), w.r.t. mesh refinement for an increased Reynolds number $\mathrm{Re} = 1000, \mathrm{Re} = 5000$, and $\mathrm{Re} = 10,000$. The starting solution for any level is the interpolated one from one level coarser. Table 6 shows the primary vortex and lower left secondary vortex w.r.t. mesh refinement for Reynolds number $\mathrm{Re} = 1000, \mathrm{Re} = 5000$, and $\mathrm{Re} = 10,000$. Moreover, we provide the streamfunction

TABLE 5 | Newtonian flow in lid-driven cavity: The kinetic energy and the number of Newton-Multigrid iterations, nonlinear number of iterations, and the average number of Multigrid iterations (N/M), for different mesh refinement at Reynolds number Re = 1000, Re = 5000, and Re = 10, 000.

Re		1000		5000		10000	
Level	**Cells**	**Energy×10²**	**N/M**	**Energy×10²**	**N/M**	**Energy×10²**	**N/M**
5	1024	4.541506	5/1	6.082524	6/1	7.940472	7/1
6	4096	4.458877	5/1	4.955858	5/1	5.369527	6/1
7	16,384	4.452357	3/1	4.768669	4/1	4.868399	5/1
8	65,536	4.451904	3/1	4.744815	3/2	4.783917	4/2
9	262,144	4.451846	3/1	4.742921	3/1	4.773500	3/2
10	1,048,576	4.451834	2/1	4.742815	3/1	4.772692	3/1
Ref. values ≈		4.45	—	4.74	—	4.77	—

TABLE 6 | Newtonian flow in lid-driven cavity: The primary vortex and the lower left secondary vortex at Re = 1000, Re = 5000, and Re = 10, 000.

Re	1000		5000		10, 000	
Level	ψ_{max}	$\psi_{min} \times 10^3$	ψ_{max}	$\psi_{min} \times 10^3$	ψ_{max}	$\psi_{min} \times 10^3$
6	0.1190073	−1.72813	0.1249471	−3.145666	0.1586626	−5.7535749
7	0.1189360	−1.72649	0.1225439	−3.077555	0.1236127	−3.2070181
8	0.1189361	−1.72851	0.1222499	−3.072411	0.1225210	−3.1831353
9	0.1189362	−1.72963	0.1222269	−3.073524	0.1224097	−3.1910101
10	0.1189366	−1.72965	0.1222259	−3.073589	0.1223892	−3.1797390
Ref.	0.1189 [28]	−1.729 [28]	0.1221 [29]	−3.070 [28]	—	—

contours for the mesh refinement level 9 and the velocity magnitude at vertical center-line w.r.t. mesh refinement for Reynolds number Re = 1000, Re = 5000, and Re = 10, 000.

As can be seen in Table 5, grid-independent results are achieved for the kinetic energy, and the displayed mesh convergence of the kinetic energy is in accordance w.r.t. Reynolds number. Moreover, for Reynolds number Re set equal to 10,000, simulations are done with edge-oriented stabilization. Thus, the mesh convergence results confirm the consistency of the edge-oriented stabilization. Also, in regard to the Newton-Multigrid method, the ratio N/M shows the mesh and Reynolds number independent solver behavior. It is worth mentioning that for the coarser levels, a few extra nonlinear iterations are required in contrast to finer mesh simply due to the decrease of interpolation error in the starting solutions.

We proceed with the solution's point-wise mesh convergence study by tracking the locations of the generated vortices for the different Reynolds numbers. Indeed, it raises awareness when dealing with visualization benchmark quantities and provides a base mesh requirement for well-documented classical Newtonian problems.

Figure 11 displays the locations of the generated vortices and the visual cutline of the velocity magnitude solutions with the successive mesh refinement at the vertical centerline for the same set of Reynolds numbers, Re is set equal to 1000, 5000, and 10,000.

At a relatively lower Reynolds number, Re set equal to 1000, three vortices are generated. The main vortex is in the middle of the cavity, the bottom left corner vortices are near the bottom left corner of the cavity, and the bottom right vortex is near the bottom right corner of the cavity. As the Reynolds number increases, for Reynolds number Re set equal to 5000, a fourth top left vortex is generated, and for Reynolds number Re set equal to 10,000, a fifth secondary bottom right vortex is generated near the bottom right corner, increasing the bottom's left vortices to a primary bottom right and secondary bottom right vortices. Furthermore, the common vortices for all Reynolds number, that is, the main, the bottom's left and the primary bottom's right vortices, change in shapes and locations with respect to the particular Reynolds number. Moreover, the velocity magnitude cutlines solutions show mesh refinement convergence in accordance with convection domination w.r.t. each particular Reynolds number.

We restrict the quantified of the location track to the common vortices for all Reynolds numbers, Re set equal to 1000, 5000, and 10,000, that is, the main and bottom's left vortices. In Table 6, we list ψ_{max} and ψ_{min} of the main and bottom's left vortices, with respect to mesh refinement for Reynolds number Re set equal to 1000, 5000, and 10,000.

Table 6 shows quantitatively the point-wise mesh convergence, once again, in accordance with progressive induces of convection with respect to the increases of Reynolds number. In Section 6.2, we investigate the accuracy of viscoplastic lid-driven cavity flow solutions with respect to the optimal settings of the pair regularization parameter and mesh refinement, besides the corresponding Newton-Multigrid solver behavior.

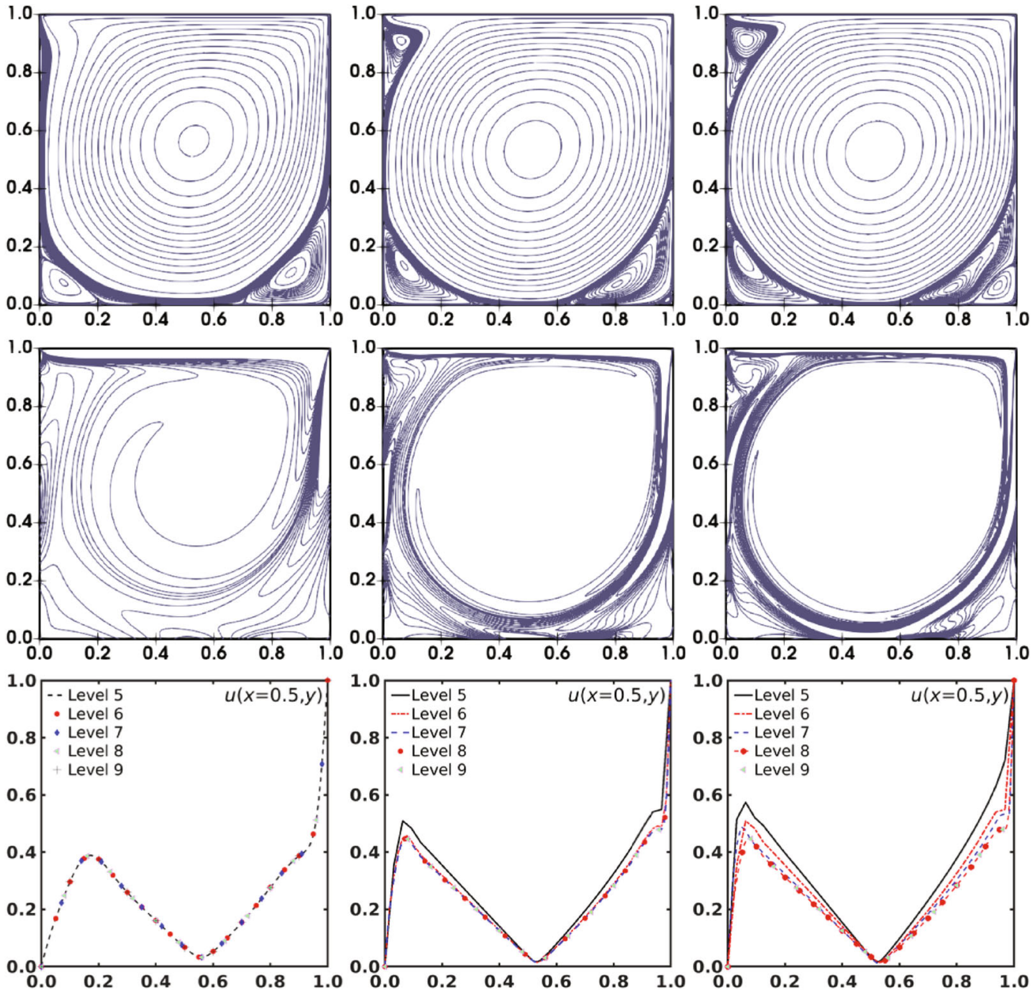

FIGURE 11 | Newtonian flow in lid-driven cavity: Streamfunction's contours at mesh refinement level 9 (TOP), the vortocity's contours at mesh refinement level 9 (middle), and velocity magnitude at vertical centerline w.r.t. mesh refinement (bottom) computed for Reynolds number Re = 1000, Re = 5000, and Re = 10,000 respectively (left to right). [Colour figure can be viewed at wileyonlinelibrary.com]

After obtaining the minimum mesh refinement for accurate solutions for problems having mesh refinement convergence in the global sense or point-wise, we proceed in Section 6.2 in the same way with problems that might lack such property for artificial reasons, for instance, due to regularization issue in quasi-Newtonian modeling of yield stress fluids.

6.2 | Viscoplastic Flow in Lid-Driven Cavity

We investigate the impact of the regularization parameter in quasi-Newtonian modeling approach for viscoplastic flow. Figure 14 shows the boundary limit of the numerical approximation of the rigid zone w.r.t. regularization parameter k. Clearly, the relative convergence of the boundary limit of the rigid zone w.r.t. regularization parameter k is obtained. Furthermore, there is an optimal regularization $k_L \approx 2^8 \approx 10^3$ from which there is no further accuracy improvement in capturing the rigid zone by increasing the regularization parameter k.

To start with, we analyze the convergence of the boundary-limit between unyielded and yielded region w.r.t. to regularization parameter k. In Figure 12, we display, in half of the cavity, the convergence of the boundary-limit for three different values of yield stress parameter $\tau_0 = 1.0$, $\tau_0 = 2.0$, and $\tau_0 = 5.0$ for the set of increasing regularization parameter $\{10^2, 10^3, 10^4\}$. We continue in Figure 13 to display the converged boundary-limit, in full cavity, in relative positions to the stream-line contours for the set of yield stress $\{1.0, 2.0, 5.0, 10.0, 20.0, 50.0\}$. Then, we summarize this visual analysis in Figure 14. The convergence analysis is displayed on the left-half of cavity, while the position of the converged boundary-limit relative to the sreamline contours is displayed on the right-half of cavity. We use the optimal choice of the regularization parameter and mesh refinement level to predict the relative position of the rigid zone to streamfunction contours for an increased nonthixotropic yield stress parameter $\tau_0 = 1$, $\tau_0 = 2$, $\tau_0 = 5$, $\tau_0 = 10$, $\tau_0 = 20$, and $\tau_0 = 50$. In addition, we provide the corresponding Newton-Multigid data in Table 7, that is, the number of nonlinear iterations and the average number of Multigrid iterations (N/M), w.r.t. different regularization parameters k and mesh refinement levels L. The solutions are calculated using the continuation process w.r.t. regularization k.

From Table 7, we conclude that the Newton-multigrid solver is mesh refinement independent. Clearly, the nonlinearity of the problem is increased by increasing the nonthixotropic yield stress

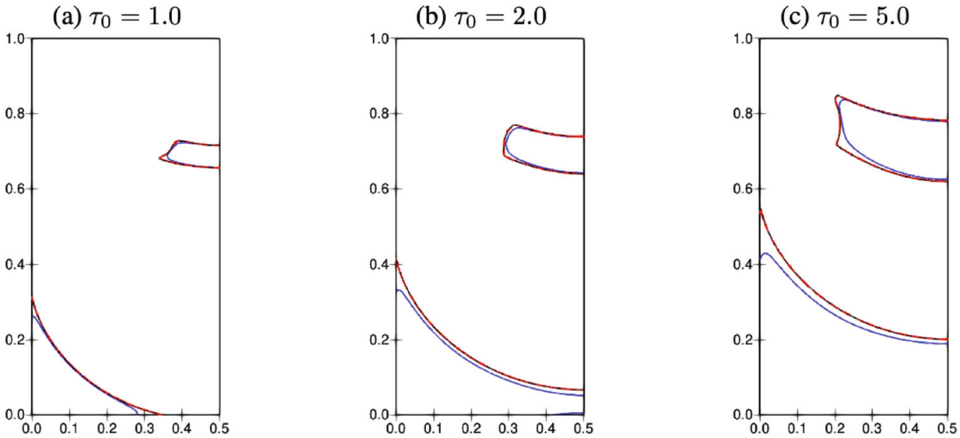

FIGURE 12 | Viscoplastic lid-driven cavity flow: Impact of the regularization parameter on the accurate track of the interface between unyielded and yielded regions for different yield stress parameter values, while $\eta_0 = 1.0$, and the regularization parameter is set to $k = 10^2$ (blue), $k = 10^3$ (black), and $k = 10^4$ (red). The solutions are calculated at mesh-refinement level 7.

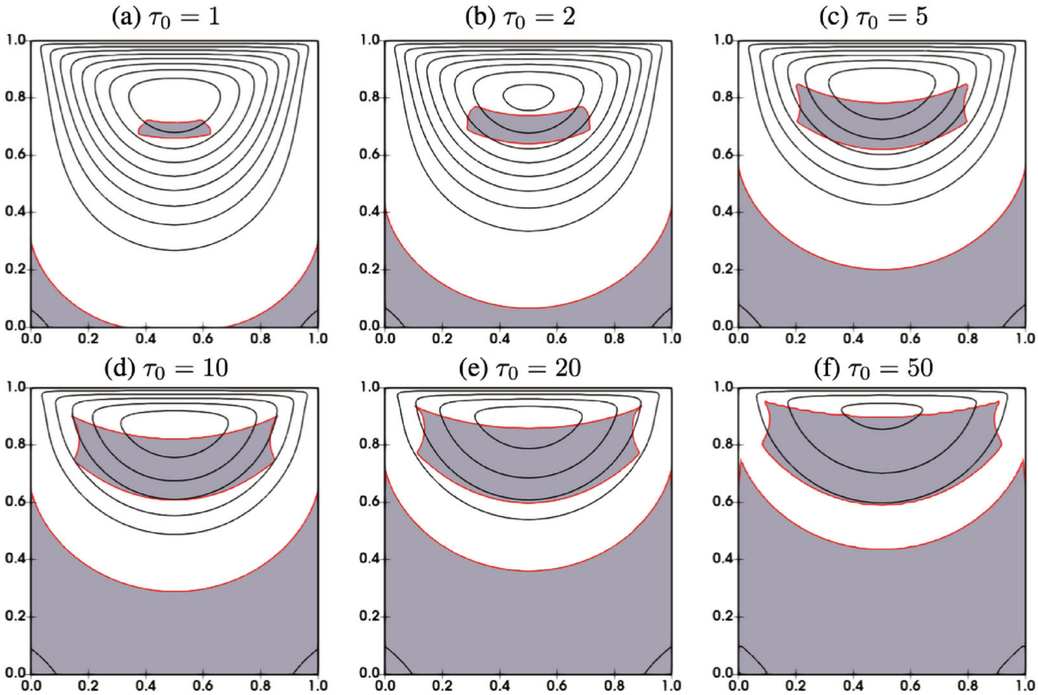

FIGURE 13 | Bingham viscoplastic flow in lid-driven cavity: The relative position of the plastic/rigid zone to streamfunction contours for an increased nonthixotropic yield stress parameter τ_0. The other parameters are set to $\eta_0 = 1.0$, $\eta_\infty = 0.0$, and $\tau_1 = 0.0$. The solutions are calculated at mesh-refinement level 8, and regularization parameter $k = 10^4$.

parameter τ_0. It is worth to note that the slight increases in the number of nonlinear iterations w.r.t. mesh refinement is due to the continuation process w.r.t. regularization parameter k used to obtain the solutions. We obtain the point-wise convergence of the boundary limit of the rigid zone w.r.t. the regularization parameter k. Furthermore, there is pair $(k, L) \approx \left(2^8, 8\right)$ regularization and mesh refinement level beyond which no further resolution improvement is possible.

Viscoplastic lid-driven cavity flow investigation provided us with the optimal settings of mesh refinement and regularization parameters for accuracy and the continuation strategy with respect to regularization parameters for efficiency. Next, in Section 6.3, we proceed with the investigations of TVP flow.

6.3 | TVP Flow in Lid-Driven Cavity

TVP lid-driven cavity flow investigations concern the track of the location and shape of the formed unyielded regions with respect to thixotropic yield stress, the performance of Newton-Multigrid solver with respect to thixotropic yield stress, regularization parameter, mesh refinement level, and the role of the microstructure equation in defining transitions between regions. We analyze the corresponding Newton-Multigrid solver convergence with

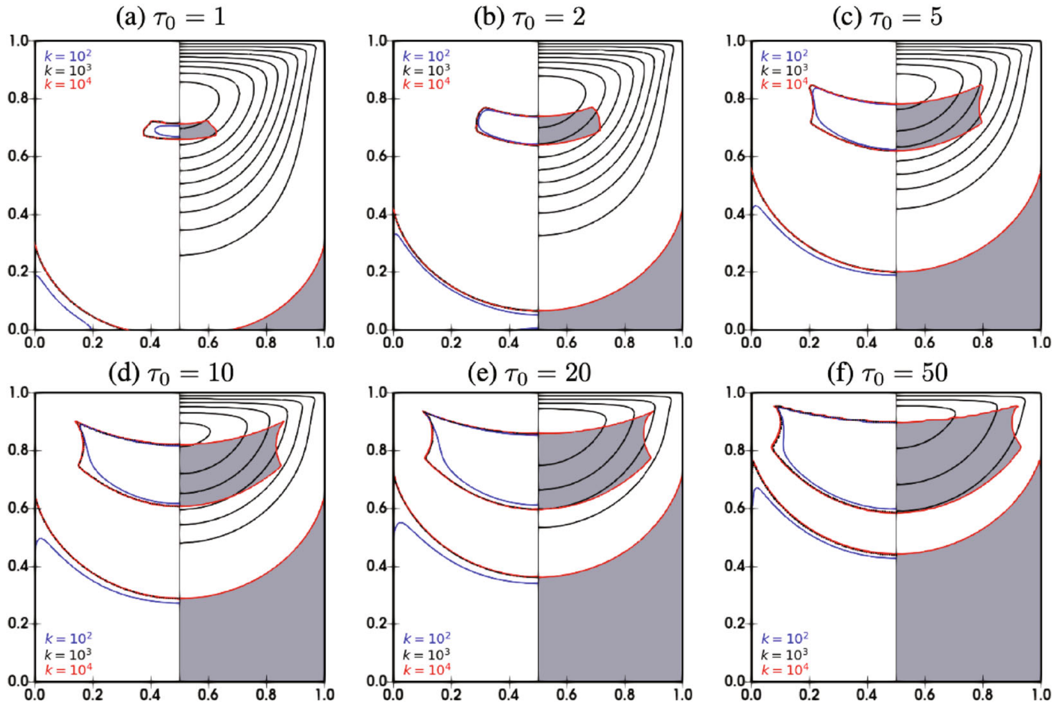

FIGURE 14 | Bingham viscoplastic flow in lid-driven cavity: The convergence analysis of the plastic/rigid zone w.r.t. regularization parameter k, $k = 10^2$ (blue), $k = 10^3$ (black), and $k = 10^4$ (red) on the left-half cavity, and of the relative position of the plastic/rigid zone to streamfunction contours on the right-half cavity, for an increased nonthixotropic yield stress parameter τ_0. The other parameters are set to $\eta_0 = 1.0$, $\eta_\infty = 0.0$, and $\tau_1 = 0.0$. The solutions are calculated at mesh-refinement level 8. [Colour figure can be viewed at wileyonlinelibrary.com]

TABLE 7 | Viscoplastic flow in lid-driven cavity: The number of Newton-Multigrid iterations, nonlinear number of iterations and the average number of Multigrid iterations (N/M), w.r.t. different values of regularization parameter k and mesh refinement levels L for Bingham viscoplastic flow for different values of nonthixotropic yield stress parameters τ_0.

$k \backslash L$	5	6	7	5	6	7	5	6	7
		$\tau_0 = 1$			$\tau_0 = 2$			$\tau_0 = 5$	
5×10^1	2/1	2/1	2/1	2/1	2/1	2/1	3/1	3/1	3/1
1×10^2	3/1	3/1	3/1	3/1	3/1	3/1	4/1	4/1	4/1
5×10^2	3/1	2/1	2/1	3/1	2/1	3/1	3/2	3/2	3/1
1×10^3	2/2	3/2	3/1	3/1	3/1	4/1	4/1	5/2	5/2
5×10^3	2/1	2/1	4/1	3/1	3/2	6/2	4/1	8/2	6/1
1×10^4	2/1	2/2	5/1	3/1	3/1	6/1	4/1	5/4	6/3
		$\tau_0 = 10$			$\tau_0 = 20$			$\tau_0 = 50$	
5×10^1	4/1	3/1	3/1	4/1	4/1	3/2	5/4	4/2	4/2
1×10^2	5/2	4/1	4/1	5/2	5/2	5/1	6/5	5/4	5/1
5×10^2	5/3	3/2	3/1	4/4	3/4	4/3	5/4	4/2	4/3
1×10^3	5/2	7/4	9/1	5/5	7/2	8/1	5/5	9/2	9/2
5×10^3	5/1	7/3	8/2	6/3	6/4	6/4	6/4	7/2	8/2
1×10^4	6/1	7/2	8/3	6/3	5/5	7/3	6/3	7/3	8/2

respect to thixotropic yield stress parameter, and regularization parameter on successive mesh refinement levels. Furthermore, TVP flow equations, in contrast to Bingham viscoplastic flow equations, increase the numerical simulation challenges. First, the extended viscosity function integrates the microstructure via thixotropic plastic viscosity and thixotropic yield stress. Second, the set of equations is supplemented with a microstructure evolution equation.

Figure 15 sets out the relative position of the rigid zones (shaded area), in terms of shear rate, to streamfunction contours for a set of increased thixotropic yield stress parameter τ_∞, $\{0.5, 1.0, 2.0, 5.0, 10.0, 20.0\}$. The solutions are calculated with the resolution threshold pair mesh refinement level, and regularization parameter k set equal to 7, and 10^4, respectively.

Figure 15 depicts the formation of two unyielded regions, one resting at the bottom of the cavity and separated from the yielded

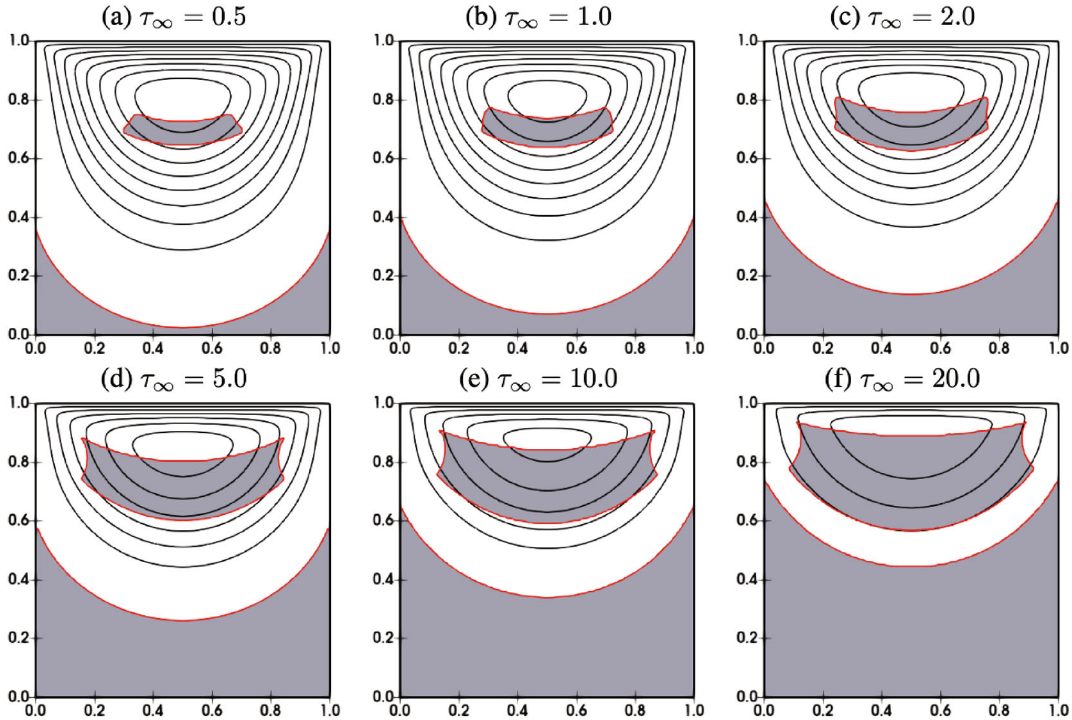

FIGURE 15 | Thixoviscoplastic flow in lid-driven cavity: The relative position of the plastic/rigid zone to streamfunction contours for an increased thixotropic yield stress parameter τ_∞. The other parameters are set to $\eta_0 = 1.0$, $\eta_\infty = 0.0$, $\tau_0 = 1.0$, $\mathcal{M}_a = 1.0$ and $\mathcal{M}_b = 0.1$. The Papanastasiou regularization parameter is set to $k = 10^4$. The solutions are calculated at mesh-refinement level 8. [Colour figure can be viewed at wileyonlinelibrary.com]

region with a circular interface, and the other located near the lid of a lip-like shape surrounded by the yielded region. For the set of increased thixotropic yield stress parameter values, both unyielded regions expand and occupy the shrinking yielded region. Moreover, as the thixotropic yield stress parameter increases, the intensity of the main vortex decreases and moves toward the lid. The unyielded regions for the set of increased thixotropic yield stress parameter values, are built on the unyielded regions, that correspond to the nonthixotropic yield stress value τ_0 set equal to 1.0. This is concretized in the corresponding larger unyielded regions compared to viscoplastic unyielded regions, which makes the thixotropic lid-driven cavity flow more challenging for Newton-Multigrid solver, due to the additional dependency of the extended viscosity function on microstructure.

The Newton-Multigrid solver's statistics results are listed in Table 8, in a block-wise manner. Each block corresponds to a particular thixotropic yield stress parameter value, and displays the Newton-Multigrid results with respect to increases in regularization parameters for successive mesh refinement levels. The blocks correspond to the set of increased yield stress parameters $\{0.5, 1.0, 2.0, 5.0, 10.0, 20.0\}$. The solutions are calculated using the continuation process w.r.t. regularization k. Similar to the viscoplastic case, the nonlinearity of the problem is increased either by increasing the plasticity in terms of the thixotropic yield stress parameter or by increasing the regularization parameter. The additional numerical complexity related to microstructure equation, namely extra nonlinearities, increased a little bit the nonlinear sweeps. With respect to the linear solver, Multigrid shows mesh-independent behavior for all blocks of the thixotropic yield stress parameter, which confirms the efficient performance of monolithic Newton-Multigrid for multifield problems.

Numerical simulations provide the flow distribution of TVP material for the main fields, velocity, microstructure, and pressure, as well as numerical quantities, for instance, shear rate. So far, the location and shape of zones have been analyzed by means of shear rate. With the interplay role of shear rate and microstructure in defining the zones, we intend to show the flow distributions of the microstructure field only, for the investigation of types of transitions between zones. We proceed with our investigation to analyze the role played by the microstructure equation in defining the types of transitions between unyielded and yielded regions. The microstructure evolution equation integrates the competition processes of Aging (buildup) and Rejuvenation (breakdown) inhabited in thixotropic material. This process occurs via the interaction of buildup and breakdown functions dependent on two additional model parameters, namely buildup and breakdown parameters. We restrict our analysis with respect to breakdown parameters, as such types of transitions are due to the ratio of breakdown parameter and buildup parameter.

Figure 16 draws the breakdown parameter, $\mathcal{M}_b = 0.5$, $\mathcal{M}_b = 1.0$, and $\mathcal{M}_b = 2.0$, to investigate the type of transitions within the material microstructure. The rigid zone is kept unchangeable by setting yield stresses to $\tau_\infty = \tau_0 = 2.0$ while other parameters are set to $\eta_0 = 1.0$, $\eta_\infty = 0.0$, $\tau_0 = 2.0$, and $\mathcal{M}_a = 1.0$.

The microstructure solutions lie between zero and unity, and it take values close to unity for indicating unyielded zones in Figure 16. Moreover, a clear smooth transition occurs between

TABLE 8 | Thixoviscoplastic flow in lid-driven cavity: Number of Newton-Multigrid iterations, nonlinear number of iterations, and the average number of Multigrid iterations (N/M), w.r.t. different values of regularization parameter k and mesh refinement levels L for thixoviscoplastic flow for different values of thixotropic yield stress parameter τ_∞.

$k \backslash L$	5	6	7	5	6	7	5	6	7
		$\tau_\infty = 0.5$			$\tau_\infty = 1$			$\tau_\infty = 2$	
5×10^1	4/2	4/2	4/2	3/2	3/3	7/1	3/2	3/3	8/1
1×10^2	4/1	4/2	5/1	4/1	4/2	7/1	4/2	4/2	8/1
5×10^2	4/1	4/1	5/1	3/1	4/1	6/1	4/2	4/2	8/1
1×10^3	4/1	4/1	4/1	4/2	4/2	8/1	4/4	6/1	7/1
5×10^3	4/1	4/1	3/2	7/1	9/1	5/1	6/1	9/1	8/1
1×10^4	4/1	4/2	4/2	5/1	7/1	4/1	7/1	10/1	8/2
		$\tau_\infty = 5.0$			$\tau_\infty = 10.0$			$\tau_\infty = 20.0$	
5×10^1	4/2	3/2	11/1	11/1	4/2	7/1	12/1	5/3	9/1
1×10^2	4/2	5/2	11/1	10/1	5/3	8/1	12/1	6/3	10/1
5×10^2	5/2	4/2	10/1	9/1	5/3	5/1	8/1	5/5	11/1
1×10^3	5/2	9/1	10/1	10/1	9/1	7/1	8/2	9/1	9/2
5×10^3	5/1	5/1	5/1	8/1	8/2	6/1	8/1	7/1	11/1
1×10^4	5/1	5/2	5/1	8/3	7/1	5/1	8/2	7/1	9/1

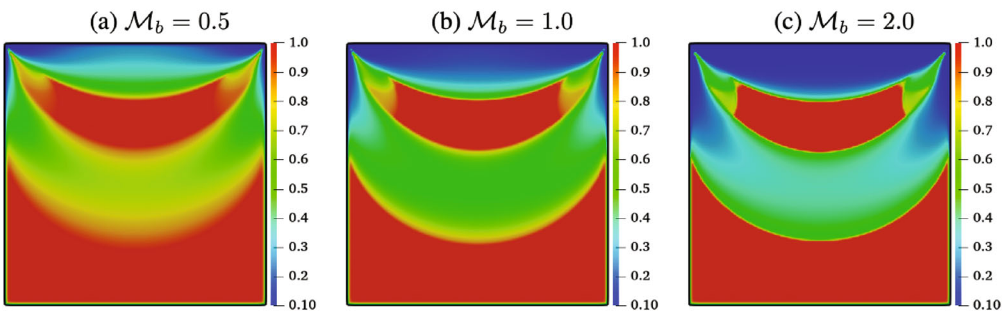

FIGURE 16 | Thixoviscoplastic flow in lid-driven cavity: Impact of breakdown parameter on structuring level of material w.r.t breakdown parameter while, $\eta_0 = 1.0$, $\eta_\infty = 0.0$, $\tau_0 = \tau_\infty = 2.0$, and $\mathcal{M}_a = 1.0$. The Papanastasiou regularization parameter is chosen as $k = 10^4$. The solutions are calculated at mesh-refinement level 7 and through integration of uniform speed $U = 1.0$ at upper lid of square cavity. [Colour figure can be viewed at wileyonlinelibrary.com]

zones, termed as *shear localization*, for relatively small values of breakdown parameter. As the breakdown parameter increases, the transitions get sharper and reveal the *shear band* phenomenon. Next Section §7 is dedicated to the manifestation of thixotropic phenomena to 4:1 contraction configuration.

7 | TVP 4:1 Contraction Application

We proceed with a 4:1 contraction configuration as close enough to industrial application as it is present in most engineering processes, for instance. Besides the complex geometric topology and the corresponding non-structured meshing Figure 17, it raises the challenges w.r.t. boundary conditions settings. On the one hand, the microstructure equation requires an inflow BC, and on the other hand, it is not obvious to derive an analytic BCs expression for Houska thixoviscplastic model. Figure 17 presents the computational domain and the coarse gird mesh, where we show the different zones, inflow's entrance zone, transit's zone, and outflow's exit zone, with the corresponding quadrilateral composition. Furthermore, 4:1 configuration constitutes a different additional test for the solver. In Figure 18, we concisely describe a one-step multilevel algorithm on the mesh-slice for the transit's zone.

In order to deal with the boundary condition settings problem, we assume a fully developed flow and drive a Houska TVP as a reduced one-dimensional model, that we use to get a discrete one-dimensional Houska solution that we use for BCs settings. Moreover, the Houska TVP reduced model solution can be used as a validation tool for the fully developed FEM two-dimensional numerical solutions. In doing so, we established a double-gate to a reduced model to get on one hand a proper BCs settings, and on the other hand a validation tool for FEM numerical solutions.

7.1 | Mechanism for BCs Settings and Solution's Validation

In contrast to the Bingham viscoplastic benchmark, Houska TVP raises the challenges w.r.t. boundary conditions and reference

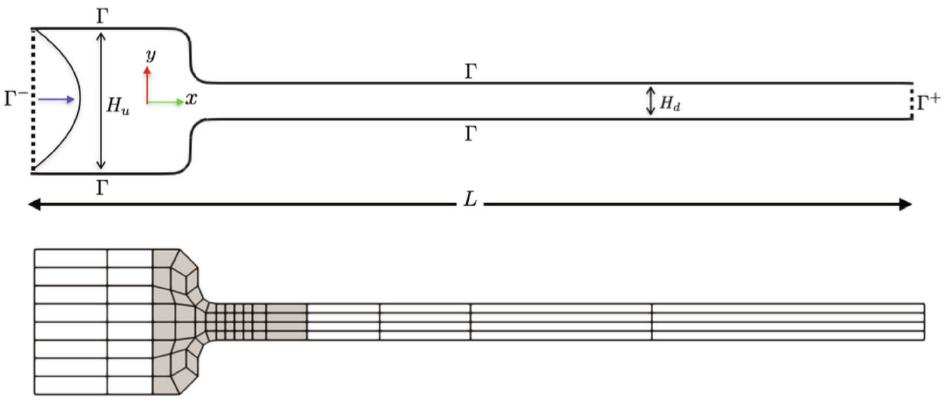

FIGURE 17 | Thixoviscoplastic contraction flow: 4:1 Contraction configuration and coarse grid mesh. [Colour figure can be viewed at wileyonlinelibrary.com]

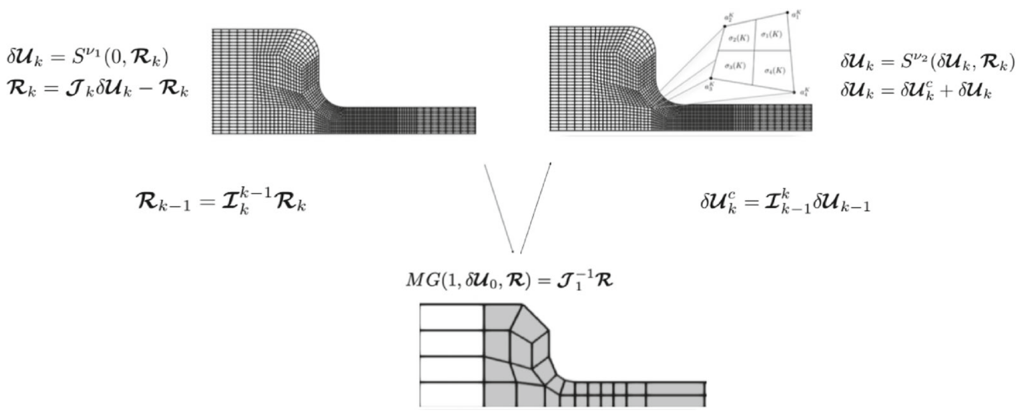

FIGURE 18 | Multigrid V-cycle schema: Schematic description of V-cycle Multigrid on a mesh-slice for the transit's zone of 4:1 contraction configuration.

solutions. On the one hand, the microstructure equation requires an inflow BCs, and on the other hand, the complexity of having analytic reference solutions. We deal with these challenges by assuming a fully developed flow and driving a Houska TVP as reduced one-dimensional model, that we use to get a discrete one-dimensional Houska solution that we utilize for BCs, and for the validations for two-dimensional numerical tests.

We display the one-dimensional reduced Houska TVP velocity solution as a discrete data, that we use as Dirichlet BCs for the two-dimensional numerical tests in Figure 19 (left-top). We give two-dimensional FEM Houska TVP velocity solution distribution in Figure 19 (right-top). Then for validations, we take the two-dimensional solutions at vertical cross lines, simply with the representative line $y = 0.5$, that we compare to the one-dimensional reduced Houska TVP Figure 19 (left-top). Similarly, we display the microstructure solution for the one-dimensional reduced Houska model as discrete data together with the microstructure FEM two-dimensional Houska model in Figure 19 (left-bottom), and the microstructure FEM two-dimensional distribution in Figure 19 (right-bottom).

It is clear from the two-dimensional FEM Houska TVP velocity solution distribution in Figure 19 (right-top), and the perfect agreement of its vertical cut lines with the one-dimensional reduced Houska TVP velocity solution in Figure 19 (left-top), that the solution satisfies the fully developed flow assumption. Moreover, the solution at outflow is free from the well-known reversing back flow associated with classical "do-nothing" BCs. Moreover, the perfect agreement of the vertical cut lines of the FEM two-dimensional Houska TVP microstructure solution, displayed in Figure 19 (right-bottom), with the one-dimensional reduced Houska TVP microstructure solution in Figure 19 (left-bottom) confirms the validity of the FEM two-dimensional Houska TVP microstructure solution. Having the double-gate mechanism to the reduced Houska model for obtaining proper BCs settings and a validation solution's tool, we proceed to investigate the impact of taking into consideration the thixotropic scale in yield stress material in 4:1 contraction flow.

7.2 | TVP 4:1 Contraction Application

Our aim is to revisit the 4:1 flow characteristics by taking into consideration thixotropic scale in viscoplastic material simply by tuning the breakdown parameter $\mathcal{M}_b$. We display in Figure 20 the flow simulations with two breakdown parameters $\mathcal{M}_b = 1.0$ (top) and $\mathcal{M}_b = 2.0$ (bottom).

As it is increasing, the breakdown parameter induces more rejuvenation layers in the vicinity of the upper stream channel on the one hand, and freeing the entrance zone from deed flow

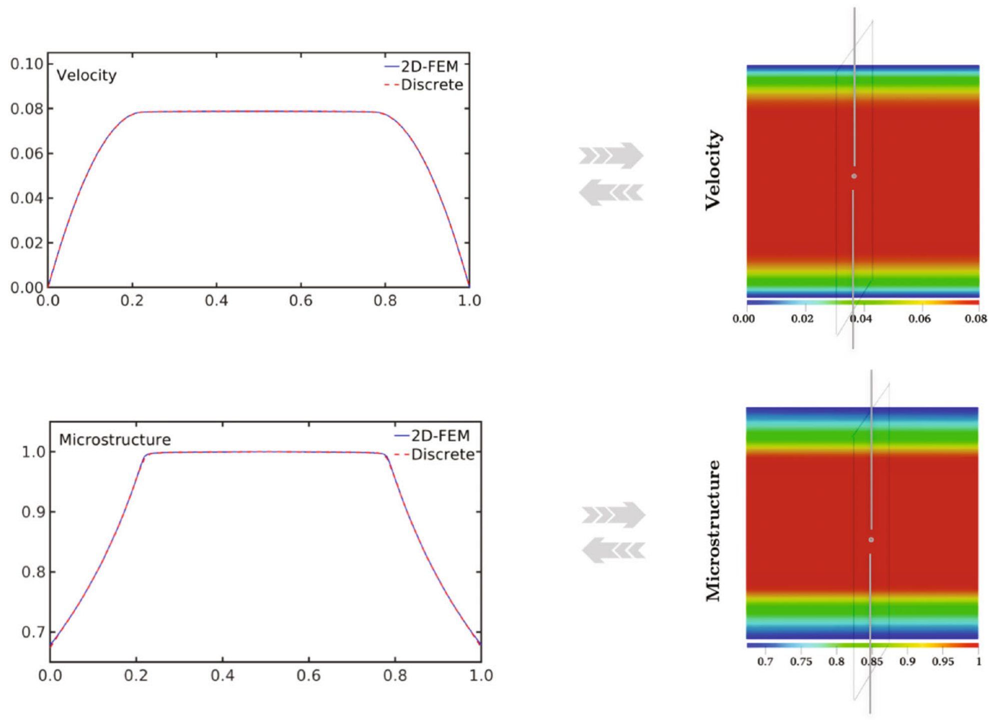

FIGURE 19 | Mechanism for TVP BCs settings and solution's validation: Comparison of velocity and microstructure solutions of 1D and fully developed 2D models for TVP flows. [Colour figure can be viewed at wileyonlinelibrary.com]

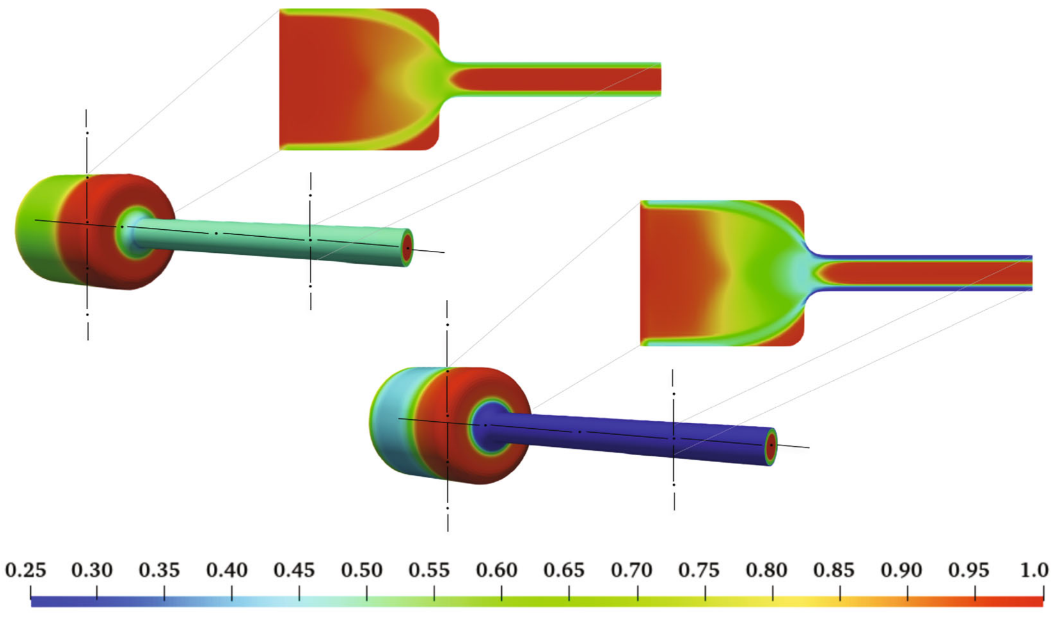

FIGURE 20 | Thixoviscoplastic flows in contractions: Microstructure λ distribution with respect to breakdown parameter, $\mathcal{M}_b = 1.0/\mathcal{M}_b = 2.0$ (top/bottom). The remaining model parameters are set to $\mathcal{M}_a = 1.0$, $\tau_0 = 0.0$, $\eta_\infty = 1.0$, $\tau_\infty = 2.0$, $\eta_0 = 1.0$, and $k = 10^4$. [Colour figure can be viewed at wileyonlinelibrary.com]

on the other hand, which eases the flowing of TVP material in contrast to simple yield stress material. As a consequence, the optimal pressure drop BCs settings for yield stress material taking into consideration thixotropic scale is lower, suggesting the need for further investigations in the design of channels used in the transportations of thixotropic material, for instance, crude oil.

8 | Summary

We presented a Newton-Multigrid FEM solver for the quasi-Newtonian modeling approach for TVP flows. Based on a two-field Stokes solver, we used higher-order stable Q_2/P_1^{disc} FE discretization for velocity and pressure. Then, we collocate the microstructure field similar as the velocity field, using the higher order Q_2 FE approximation, with edge-oriented jump of the gradient to upgrade the coercivity to match the space norm. Additionally, it is consistent with FEM discretization, linear with respect to the problem, and improves the solver's efficiency. The FEM quasi-Newtonian model for TVP flows is a highly nonlinear multifield coupled problem. The extended viscosity for generalized TVP Stokes equations is dependent on flow fields, by means of shear rate and microstructure, and the regularization parameter. Besides the thixotropic model is dependent on the shear rate. Consequently, the FEM quasi-Newtonian modeling approach requires a robust solver to obtain accurate numerical solutions.

First, we used an adaptive discrete Newton and monolithic geometric Multigrid solver to delicately handle the regularization and to treat the nonlinearity multifield coupled issues alike. The solver has two folds with respect to adaptivity; the one related to discrete Newton's method is done via the step-size in finite difference approximation of the Jacobian, while the one related to the linear Multigrid solver is achieved by requiring optimal convergence according to the nonlinear one. The resultant solver is a black box solely dependent on the actual rate of the nonlinear residual convergence, singularity-free, and robust with respect to the starting guess.

Second, we advantageously concretized the monolithic geometric Multigrid solver on FEM discretization choice. It is based on the local pressure Schur complement (LPSC) approach to handle the coupled linearized TVP saddle point problems locally. That is, to solve exactly on the element level, one element or a patch of elements, and perform an outer block Gauss–Seidel iteration. The choice of the blocks for block Gauss–Seidel iteration is based on the pressure degrees of freedom P_1^{disc}. The local character of this procedure together with the global defect-correction mechanism on the one hand, and the choice of discontinuous FE approximations for the pressure on the other, results in an efficient linear solver.

Summarizing, we developed a solver for accurate, robust, and efficient monolithic Newton-Multigrid FEM TVP generalized Stokes equations. The developed solver is black box, and is based on the monolithic Newton-Multigrid method. It uses an adaptive strategy for the step-size control in divided differences for the Jacobian approximation. The size of step length follows the convergence process via the actual residual convergence rate. Accordingly, the Multigrid convergence is made optimal to achieve the nonlinear convergence. To conclude, the combination of pair Q_2/P_1^{disc} FEM discretization together with an adaptive Newton-Multigrid solver results in a highly numerically accurate, robust, and efficient solution scheme. We analyzed the performance of the solver w.r.t. to regularization parameters, mesh refinement, and different boundary conditions settings in detailed case studies. The current state of our solver does not support high-performance computing platforms, and it is in the focus of our future investigations.

For numerical investigations, we used a lid-driven cavity as an academic standard benchmark to investigate the accuracy, robustness, and the efficiency of our developed monolithic Newton-Multigrid FEM TVP solver. Moreover, we considered the 4:1 contraction configuration as a close enough to industrial application, and it raises the challenges w.r.t. boundary conditions settings.

At the start, we used Newtonian lid-driven cavity flow benchmark to validate our numerical method and simulation algorithm. It provided us with a point-wise benchmark, in terms of cutline solutions, and well-studied vortices, with respect to Reynolds number. We got mesh convergence for both, global quantity (in terms of kinetic energy), and point-wisely (in terms of vertical centerline velocity magnitude cutlines and the locations of vortices). Moreover, we achieved mesh refinement independent behavior for Newton-Multigrid solver for a wide range of Reynolds numbers. Importantly, since the Newtonian flow is free from regularization effects, which occur for our choice of quasi-Newtonian modeling approach for viscoplastic and TVP flows, we obtained a reference base for a mesh refinement for FEM solutions point-wisely.

Then, we addressed the quasi-Newtonian modeling approach for yield stress materials, as it introduces a regularization parameter to get a well-defined extended viscosity function in whole computational domain. We investigated the accurate growth and location of unyielded regions. On the one hand, we obtained the point-wise convergence of interfaces between unyielded and yielded regions with respect to regularization parameter k. Furthermore, for the pair mesh refinement level, and regularization parameter k set equal to 7, and 10^4 respectively, we reached the best resolution beyond which no further clear improvement by either increasing the mesh refinement level or regularization parameter is expected. On the other hand, lower-regularization parameter's solutions are used as a start for higher-regularization parameter's solutions with nonuniform increases in continuation process. For TVP, we maintained the numerical complexity related to plasticity of the same order as viscoplastic problem to analyze the impact of the upgrade of the TVP flow system with microstructure numerical challenges, namely weak coercivity, extra nonlinearities, and additional degrees of freedom. With respect to the Newton-Multigrid solver, we got a mesh-independent behavior of linear Multigrid solver, and the number of Multigrid sweeps increased in perfect accordance with the nonlinear solver's sweeps. That is, the accuracy of the linear solver matches optimally the requirements for the accuracy of the nonlinear solver.

We sealed our investigation with the analysis of the competition process of Aging and Rejuvenation, which occurs via the interaction of buildup and breakdown functions dependent on buildup and breakdown parameters. For lid-driven cavity, we examined the types of transitions between yielded and unyielded regions by monitoring the microstructure equation. We showed a smooth transition between zones, termed as *shear localization*, for relatively small values of breakdown parameter, and sharp transition between zones, termed as *shear band*, for relatively higher values of breakdown parameter. For 4:1 contraction configuration, we developed a double-gate mechanism to the one-dimensional reduced Houska model to obtain the proper BCs settings, which was used as a validation tool as well. Then, we investigated the impact of taking into consideration the thixotropic scale in yield stress material. We demonstrated that at thixotropic scale, more rejuvenation layers appear in the vicinity of the upper stream channel, and the entrance zone gets free from the deed flow, easing the flowing of TVP material. Consequently, we recommend the revisit in the design of channels used in transportations of thixotropic material to take into consideration the lower optimal pressure drop BCs settings at the thixotropic scale.

Acknowledgments

We are indebted to the anonymous reviewers for valuable remarks and comments, which leads to the inclusion of the extended analysis of the solver's performance by considering case studies to address the sensibility analysis with key parameters and by addressing the important issue of BCs settings. We also acknowledge the funding provided by the "Deutsche Forschungsgemeinschaft (DFG, German Research Foundation, 446888252)"; the "Bundesministerium fÃ¼r Wirtschaft und Energie aufgrund eines Beschlusses des Deutschen Bundestages" through "AiF-Forschungsvereinigung: Forschungs-Gesellschaft Verfahrens-Technik e. V.—GVT" under the IGF project number "20871N"; and the support by LSIII and LiDO3 team at ITMC, TU Dortmund University, Germany. Open Access funding enabled and organized by Projekt DEAL.

The paper is dedicated to Prof. Stefan Turek on the occasion of his 60th birthday, in recognition of his great contributions in CFD and HPC.

Conflicts of Interest

The authors declare no conflicts of interest.

Data Availability Statement

The data that support the findings of this article is available from the corresponding author upon reasonable request.

Endnotes

[1] https://www.mathematik.tu-dortmund.de/featflow/en/software.html.

[2] https://wwwold.mathematik.tu-dortmund.de/featflow/en/software.html.

References

1. M. Jenny, S. Kiesgen de Richter, N. Louvet, S. Skali-Lami, and Y. Dossmann, "Taylor-Couette Instability in Thixotropic Yield Stress Fluids," *Physical Review Fluids* 2 (2017): 23302–23323.

2. A. Ouazzi, N. Begum, and S. Turek, "Newton-Multigrid FEM Solver for the Simulation of Quasi-Newtonian Modelling of Thixotropic Flows," in *Numerical Methods and Algorithms in Science and Engineering*, WCCM-ECCOMAS2020, vol. 700 (2021).

3. H. Damanik, "FEM Simulation of Non–isothermal Viscoelastic Fluids" (PhD thesis, Technical University of Dortmund, 2011).

4. S. Turek, *Efficient Solvers for Incompressible Flow Problems: An Algorithmic and Computational Approach* (Berlin, Heidelberg: Springer, 1999).

5. V. Girault and P. A. Raviart, *Finite Element Methods for Navier-Stokes Equations* (Berlin-Heidelberg: Springer, 1986).

6. W. Worrall and S. Tuliani, "Viscosity Changes During the Aging of Clay-Water Suspensions," *Transactions of the British Ceramic Society* 63 (1964): 164–185.

7. P. Coussot, Q. D. Nguyen, H. T. Huynh, and D. Bonn, "Viscosity Bifurcation in Thixotropic, Yielding Fluids," *Journal of Rheology* 46, no. 3 (2002): 573–589.

8. M. Houška, "Engineering Aspects of the Rheology of Thixotropic Liquids" (PhD thesis, Faculty of Mechanical Engineering, Czech Technical University of Prague, 1981).

9. A. Mujumdar, A. N. Beris, and A. B. Metzner, "Transient Phenomena in Thixotropic Systems," *Journal of Non-Newtonian Fluid Mechanics* 102, no. 2 (2002): 157–178.

10. K. Dullaert and J. Mewis, "Transient Phenomena in Thixotropic Systems," *Journal of Non-Newtonian Fluid Mechanics* 139 (2006): 30–31.

11. A. Ouazzi, S. Turek, and H. Damanik, "A Curvature–Free Multiphase Flow Solver via Surface Stress–Based Formulation," *International Journal for Numerical Methods in Fluids* 88, no. 1 (2018): 18–31, https://doi.org/10.1002/fld.4509.

12. S. Turek, A. Ouazzi, and J. Hron, "On Pressure Separation Algorithms (PSepA) for Improving the Accuracy of Incompressible Flow Simulations," *International Journal for Numerical Methods in Fluids* 59 (2009): 387–403.

13. T. C. Papanastasiuo, "Flow of Materials With Yield," *Journal of Rheology* 31 (1987): 385–404.

14. F. Brezzi and M. Fortin, *Mixed and Hybrid Finite Element methods* (Berlin: Springer, 1986).

15. R. Temam, *Navier-Stokes Equations Theory and Numerical Analysis* (Amsterdam, The Netherlands: Elsevier Science Publishers, 1979).

16. A. Ouazzi, *Finite Element Simulation of Nonlinear Fluids: Application to Granular Material and Powder* (Germany: Shaker Verlag, 2006).

17. S. Turek and A. Ouazzi, "Unified Edge–Oriented Stabilization of Nonconforming FEM for Incompressible Flow Problems: Numerical Investigations," *Journal of Numerical Mathematics* 15, no. 4 (2007): 299–322.

18. N. Begum, "Efficient FEM Simulation Techniques for Thixoviscoplastic Flow Problems" (PhD Thesis, TU Dortmund University, 2023).

19. S. Mandal, A. Ouazzi, and S. Turek, "Modified Newton Solver for Yield Stress Fluids," in *Proceedings of ENUMATH 2015, the 11th European Conference on Numerical Mathematics and Advanced Applications* (Springer, 2016), 481–490.

20. C. Mehlmann and T. Richter, "A Modified Global Newton Solver for Viscous-Plastic Sea Ice Models," *Ocean Modelling* 116 (2017): 96–107.

21. S. Mandal, S. Turek, R. Schwarze, M. Haustein, A. Ouazzi, and A. Gladky, "Numerical Benchmarking of Granular Flow With Shear Dependent Incompressible Flow Models," *Journal of Non-Newtonian Fluid Mechanics* 262 (2018): 92–106.

22. A. Fatima, "An Adaptive Discrete Newton Method for Regularization–Free Bingham Model" (PhD thesis, TU Dortmund University, 2023).

23. A. Fatima, S. Turek, A. Ouazzi, and A. Afaq, "An Adaptive Discrete Newton Method for Regularization–Free Bingham Model," Technical report, Fakultät für Mathematik, TU Dortmund, January 2021, Ergebnisberichte des Instituts für Angewandte Mathematik, Nummer 635.

24. S. P. Vanka, "Block–Implicit Multigrid Solution of Navier–Stokes Equations in Primitive variables," *Journal of Computational Physics* 65 (1986): 138–158.

25. H. Damanik, J. Hron, A. Ouazzi, and S. Turek, "Monolithic Newton-Multigrid Solution Techniques for Incompressible Nonlinear Flow Models," *International Journal for Numerical Methods in Fluids* 71, no. 2 (2012): 208–222.

26. A. Aposporidis, E. Haber, M. A. Olshanskii, and A. Veneziani, "A Mixed Formulation of the Bingham Fluid Flow Problem: Analysis and Numerical Solution," *Computer Methods in Applied Mechanics and Engineering* 200, no. 29 (2011): 2434–2446.

27. N. Begum, A. Ouazzi, and S. Turek, "Thixoviscoplastic Flow Simulations Based on Houska Thixotropic and Bingham Viscoplastic Models," *Proceedings in Applied Mathematics and Mechanics* (2024), https://doi.org/10.1002/pamm.202400003.

28. C. Bruneau and M. Saad, "The 2D Lid-Driven Cavity Problem Revisited," *Computers & Fluids* 35 (2006): 326–348.

29. R. Kupperman, "A Central-Difference Scheme for a Pure Stream Function Formulation of Incompressible Viscous Flow," *SIAM Journal on Scientific Computing* 23 (2001): 1–18.

30. J. Hron, A. Ouazzi, and S. Turek, "A Computational Comparison of Two FEM Solvers for Nonlinear Incompressible Flow," in *Lecture Notes in Computational Science and Engineering*, vol. 35 (New York: Springer, 2003), 87–109.

Appendix A

Solver Performance on Flow Around Cylinder Benchmark

In this section, we consider the classical flow around cylinder benchmark as a case study for the performance of our solver in relative comparisons using different methods. In this context, we revisit the results in [19, 30] to systematically analyze our solver performance, for Newtonian flow for Reynolds number Re $= 20$ and Re $= 50$, for power-law model for the power indices $r = 0.5$ and $r = 0.9$, and for Bingham viscoplastic model for yield stress parameter $\tau_0 = 0.1$, $\tau_0 = 1.0$, $\tau_0 = 5.0$, and $\tau_0 = 10.0$. We use the power-law application from FeatFlow[2] software to produce the results for fixed point method, Newton's method, and adaptive continuous Newton with operator splitting. It uses the lowest stable stokes FEM pair on quadrilateral, rotated bilinear for velocity, and constant for pressure $\tilde{Q}_1/Q_0$. In Figure A1, we present the computational domain, the coarse grid mesh, and the mesh for the refinement level 4. Furthermore, we display in Table A1 the mesh information with the corresponding unknowns for both discretizations $\tilde{Q}_1/Q_0$ and Q_2/P_1^{disc}.

Flow Around Cylinder Case Study for Newtonian Flow

We perform the performance comparison in terms of residuum convergence and Multigrid rate w.r.t. nonlinear iterations of fixed point, Newton's method, adaptive continuous Newton's method via operator splitting CN-OS, and adaptive discrete Newton's method via step-length DN-SL for Newtonian flow for Reynolds number value Re $= 20$ and Re $= 50$ for successive mesh refinement levels, L3, L4, L5, and L6, which we display in Figure A2 (top), Figure A2 (bottom), Figure A3 (top), and Figure A3 (bottom), respectively. In Table A2, we summarize the statistic of the performance comparison in terms of number of nonlinear iteration iterations, and the average number of multigrid required for one nonlinear iteration. Then, we focus on the adaptive discrete Newton via step-length, and present the solver behavior by displaying in Figure A4, the Residuum, Multgrid rate, Nonlinear rate, and the step-length update, during the convergence process w.r.t. mesh refinement levels, and nonlinearity, that is, for the Reynolds number Re $= 20$ and Re $= 50$.

Flow Around Cylinder Case Study for Power-Law

We perform the performance comparison in terms of Residuum convergence and Multigrid rate w.r.t. nonlinear iterations of fixed point, Newton's method, adaptive continuous Newton's method via operator splitting CN-OS, and adaptive discrete Newton's method via step-length DN-SL for power-law for power indices value $r = 0.5$ and $r = 0.9$ for successive mesh refinement levels, L3, L4, L5, and L6, which we display in Figure A5 (top), Figure A5 (bottom), Figure A6 (top), and Figure A6 (bottom), respectively. In Table A3, we summarize the statistic of the performance comparison in terms of number of nonlinear iterations, and the average number of multigrid required for one nonlinear iteration. Then, we focus on the adaptive discrete Newton via step-length, and present the

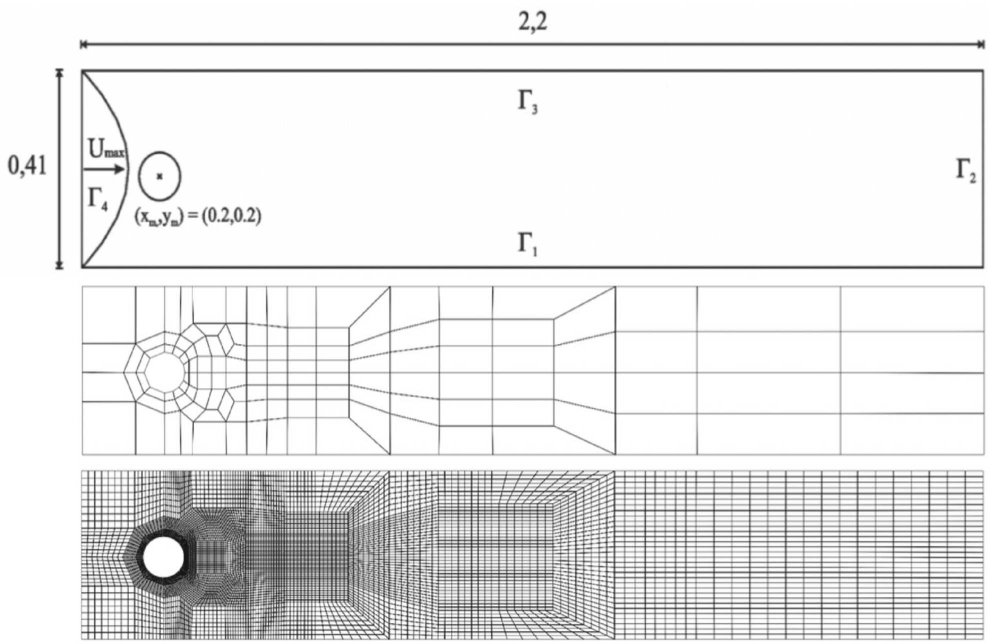

FIGURE A1 | Geometry, coarse grid mesh, that is, mesh refinement level 1, and mesh refinement level 4 for the "flow around cylinder" configuration.

TABLE A1 | Mesh information and the total unknowns for $\tilde{Q}_1/Q_0$ and Q_2/P_1^{disc} FEM discretizations for successive mesh refinement level for the "flow around cylinder" configuration.

Mesh information			Total unknowns	
Level	**Element**	**Vertices**	$\tilde{Q}_1/Q_0$	Q_2/P_1^{disc}
1	156	130	702	1 533
2	572	520	2 686	5 927
3	2 184	2 080	10, 608	23, 295
4	8 528	8 320	42, 016	92, 351
5	33, 696	33, 280	167, 232	367, 743
6	13, 952	133, 120	667, 264	—

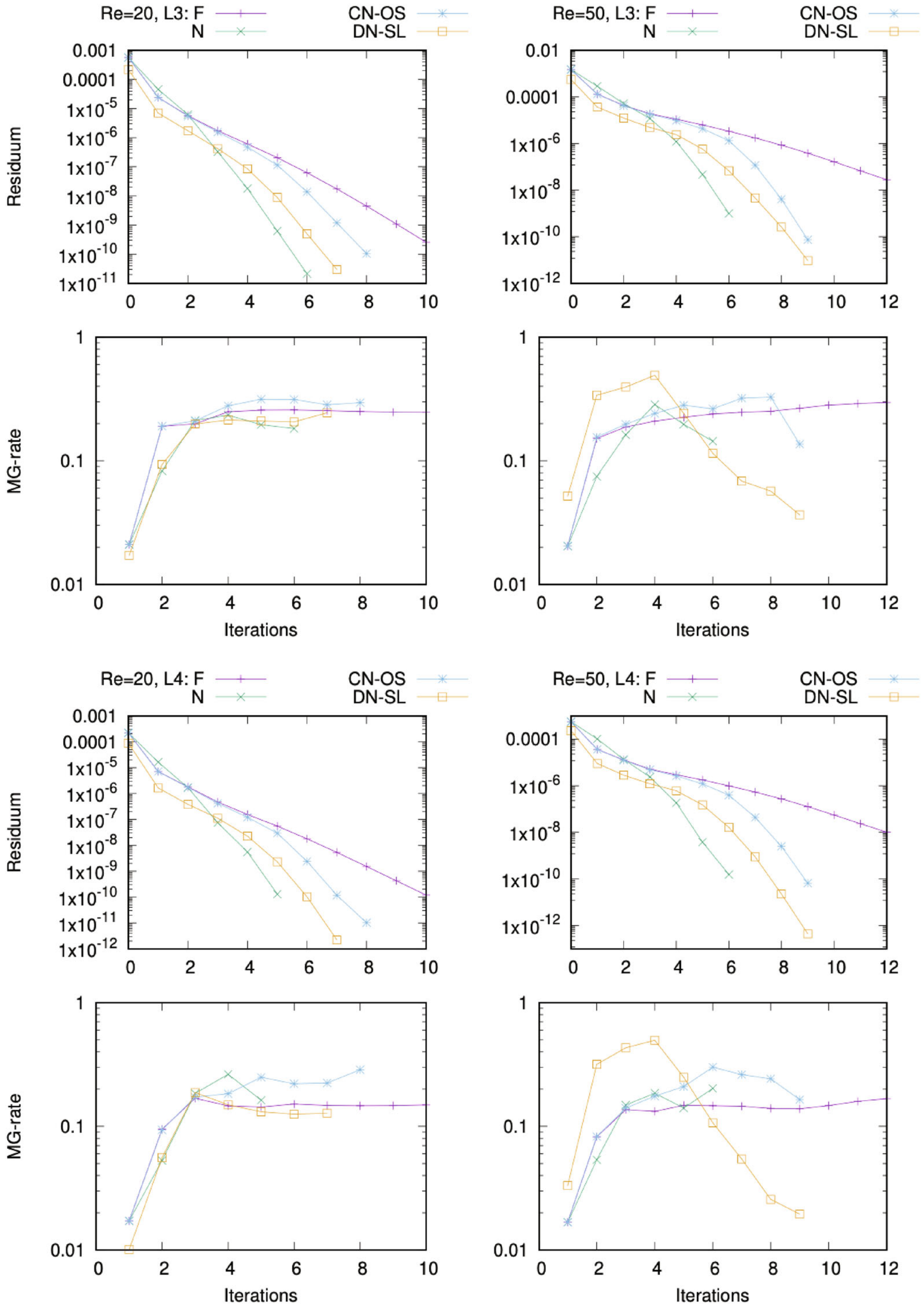

FIGURE A2 | Flow around cylinder case study for Newtonian flow: Performance comparison in terms of Residuum convergence and Multigrid rate w.r.t. iterations of fixed point, Newton's method, adaptive continuous Newton's method via operator splitting CN-OS, and adaptive discrete Newton's method via step-length DN-SL for successive mesh refinement levels for Newtonian flow for Reynolds number value Re = 20 and Re = 50. [Colour figure can be viewed at wileyonlinelibrary.com]

solver behavior by displaying in Figure A7, the Residuum, Multgrid rate, Nonlinear rate, and the step-length update, during the convergence process w.r.t. mesh refinement levels, and nonlinearity, that is, for power-law indices $r = 0.5$ and $r = 0.9$.

Flow Around Cylinder Case Study for Bingham Model

We perform the performance comparison in terms of Residuum convergence and Multigrid rate w.r.t. nonlinear iterations of fixed point, Newton's method, adaptive continuous Newton's method via operator splitting CN-OS, and adaptive discrete Newton's method via step-length DN-SL for Bingham model for yield stress parameter values $\tau = 0.1$, $\tau = 1.0$, $\tau = 5.0$, and $\tau = 10.0$ for successive mesh refinement levels, L3, L4, L5, and L6, which we display in Figures A8–A11, respectively. In Table A4, we summarize the statistics of the performance comparison in terms of number of nonlinear iteration iterations, and the average number of multigrid required for one nonlinear iteration. Then, we focus on the

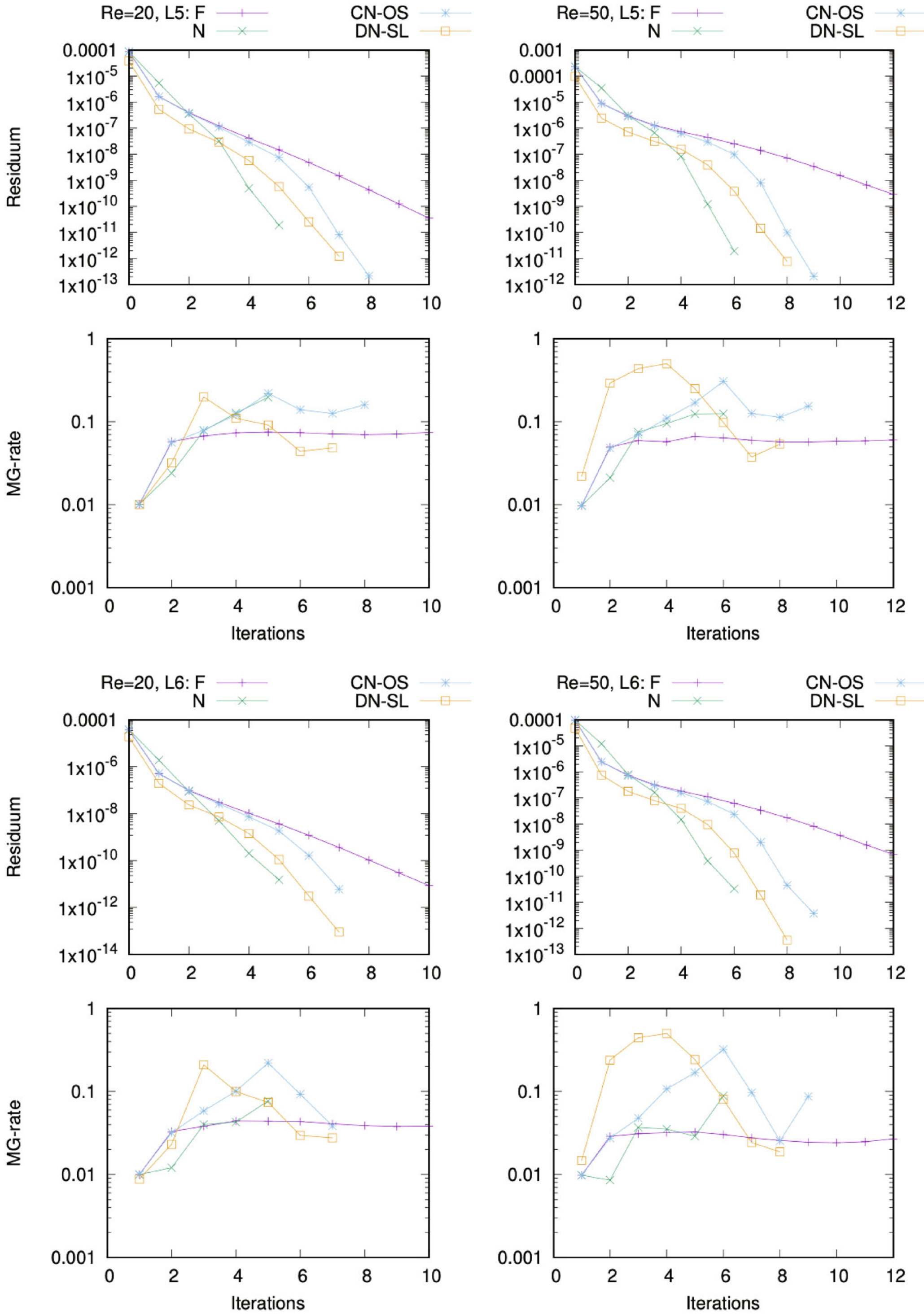

FIGURE A3 | Flow around cylinder case study for Newtonian flow: Performance comparison in terms of Residuum convergence and Multigrid rate w.r.t. iterations of fixed point, Newton's method, adaptive continuous Newton's method via operator splitting CN-OS, and adaptive discrete Newton's method via step-length DN-SL for successive mesh refinement levels for Newtonian flow for Reynolds number value Re = 20 and Re = 50. [Colour figure can be viewed at wileyonlinelibrary.com]

adaptive discrete Newton via step-length, and present the solver behavior by displaying the Residuum, Multgrid rate, Nonlinear rate, and the step-length update, during the convergence process w.r.t. mesh refinement levels, and nonlinearity, that is, for yield stress parameters $\tau = 0.1$ and $\tau = 1.0$ in Figure A12, $\tau = 1.0$ and $\tau = 5.0$ in Figure A13, $\tau = 0.1$ and $\tau = 5.0$ in Figure A14, and $\tau = 0.1$ and $\tau = 10.0$ in Figure A15, respectively.

TABLE A2 | Flow around cylinder case study for Newtonian flow: Statistic of the performance comparison in terms of number of nonlinear iteration iterations, and the average number of multigrid required for one nonlinear iteration, of fixed point method, Newton's method, adaptive continuous Newton's method via operator CN-OS splitting, and adaptive discrete Newton's method via step-length DN-SL for successive mesh refinement levels for Newtonian flow for Reynolds number value Re = 20 and Re = 50.

	Re = 20				Re = 50			
Level	**Fixed point**	**Newton**	**Adaptive CN-OS**	**Adaptive DN-SL**	**Fixed point**	**Newton**	**Adaptive CN-OS**	**Adaptive DN-SL**
3	10/2	6/2	8/2	7/2	15/2	6/2	9/2	9/2
4	10/2	6/2	8/2	7/2	15/2	6/2	9/2	9/2
5	10/1	6/2	8/2	7/1	16/1	6/2	9/2	8/1
6	10/1	6/2	7/1	7/1	15/1	6/2	9/1	8/1

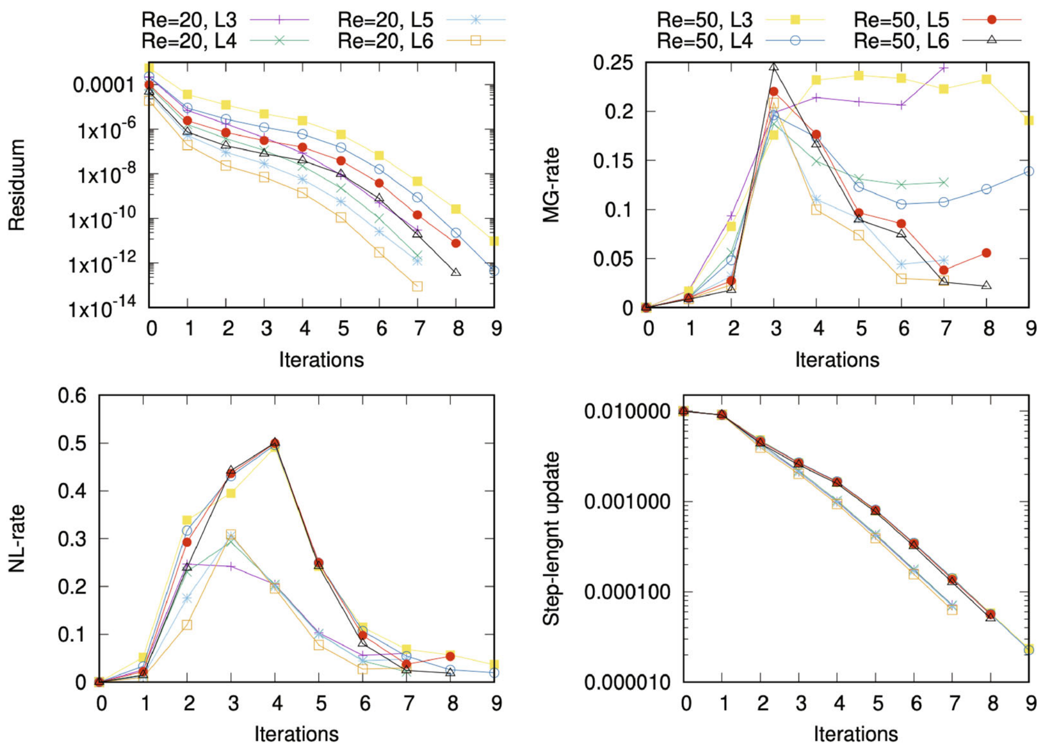

FIGURE A4 | Adaptive discrete Newton via step-length for flow around cylinder case study for Newtonian flow: Solver behavior, Residuum, Multgrid rate, Nonlinear rate, and the step-length update, during the convergence process for Newtonian flow w.r.t. mesh refinement levels, L3, L4, L5, and L6, and nonlinearity, that is, for the Reynolds number Re = 20 and Re = 50. [Colour figure can be viewed at wileyonlinelibrary.com]

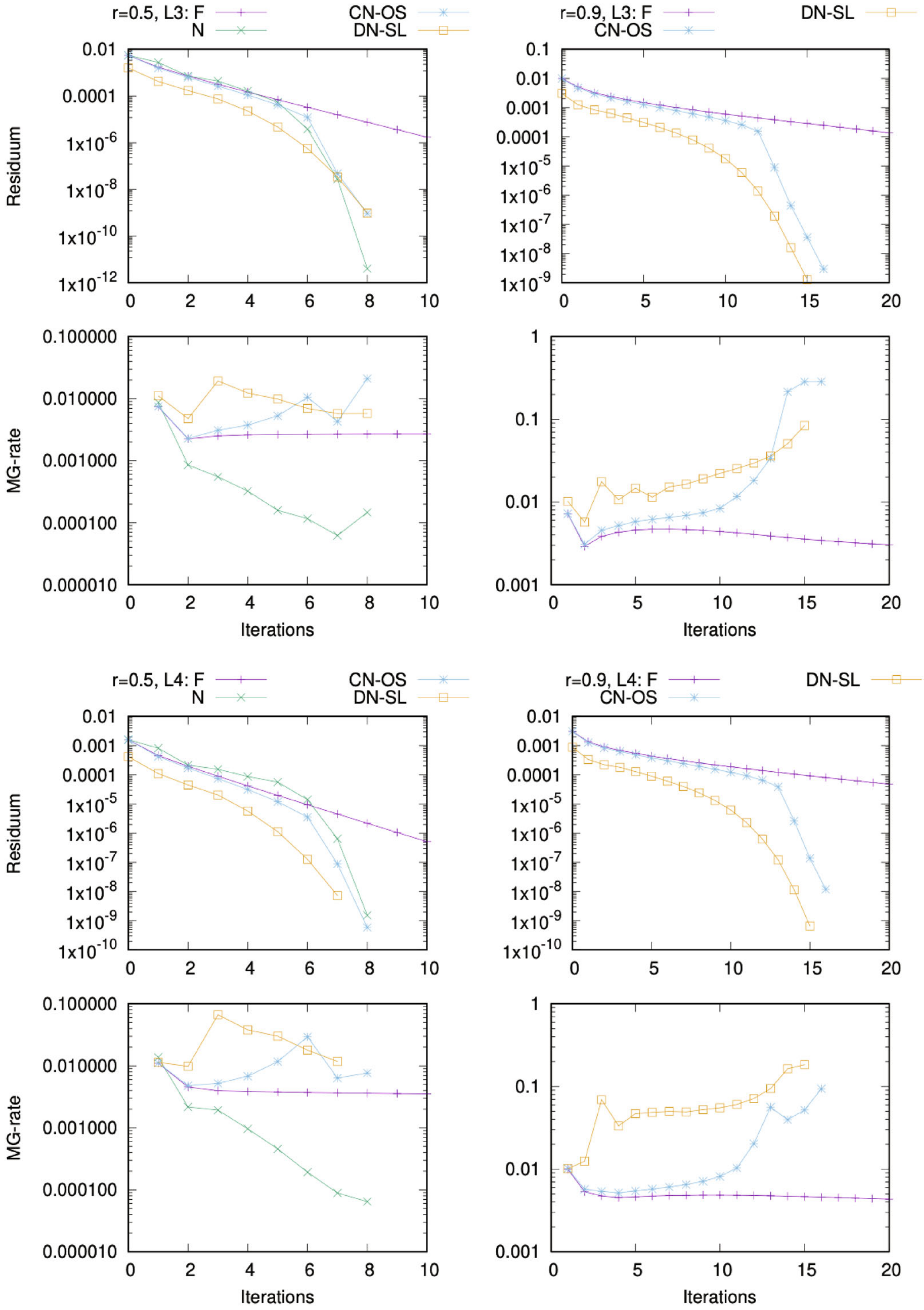

FIGURE A5 | Flow around cylinder case study for Power-law: Performance comparison, in terms of Residuum convergence and Multigrid rate w.r.t. iterations, of fixed point, Newton's method, adaptive continuous Newton's method via operator splitting CN-OS, and adaptive discrete Newton's method via step-length DN-SL for successive mesh refinement levels for power-law model for the power indices values $r = 0.5$ and $r = 0.9$. [Colour figure can be viewed at wileyonlinelibrary.com]

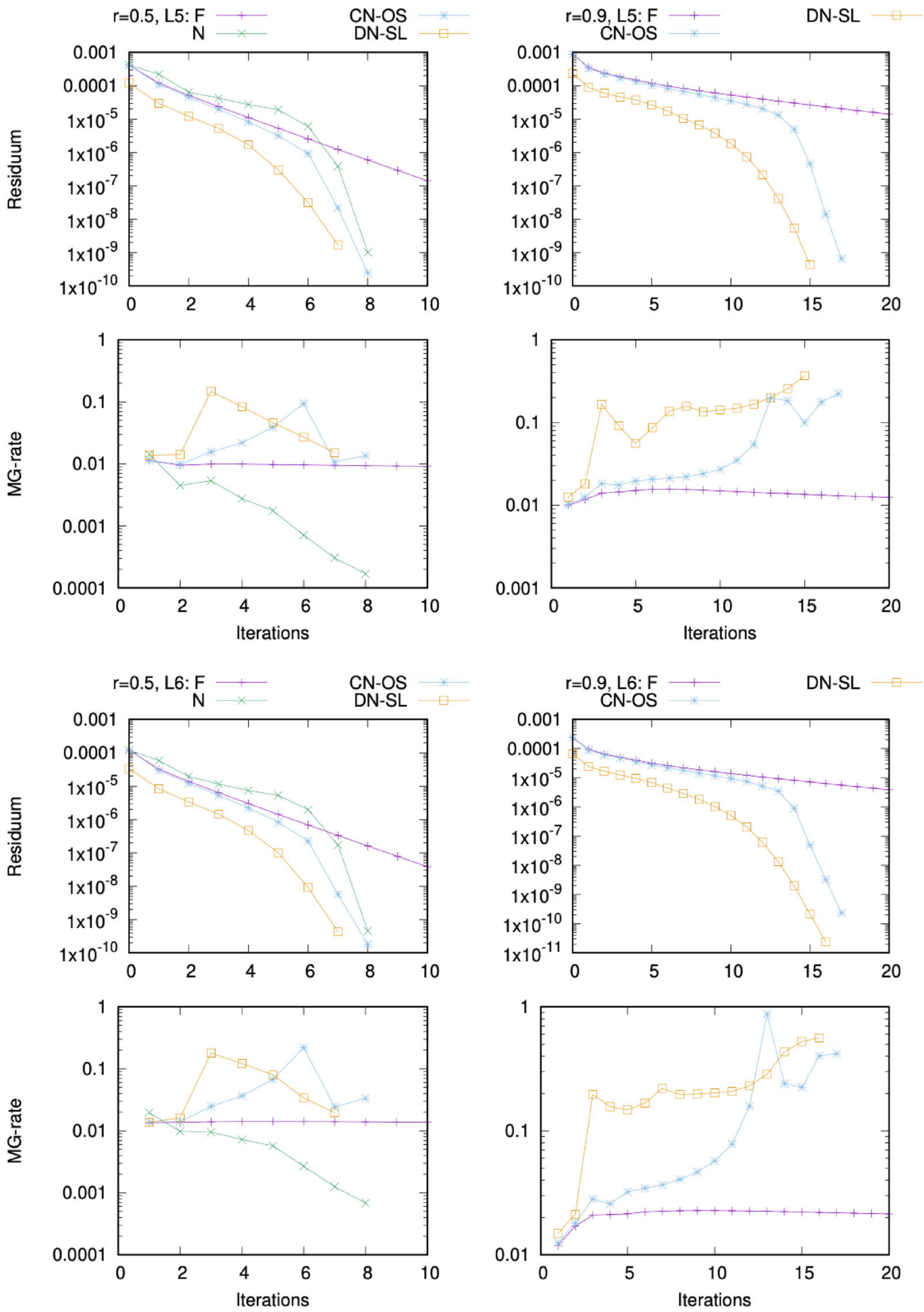

FIGURE A6 | Flow around cylinder case study for Power-law: Performance comparison, in terms of Residuum convergence and Multigrid rate w.r.t. iterations, of fixed point, Newton's method, adaptive continuous Newton's method via operator splitting CN-OS, and adaptive discrete Newton's method via step-length DN-SL for successive mesh refinement levels for power-law model for the power indices values $r = 0.5$ and $r = 0.9$. [Colour figure can be viewed at wileyonlinelibrary.com]

TABLE A3 | Flow around cylinder case study for Power-law: Statistic of the performance comparison, in terms of number of nonlinear iteration iterations, and the average number of multigrid required for one nonlinear iteration, of fixed point method, Newton's method, adaptive continuous Newton's method via operator CN-OS splitting, and adaptive discrete Newton's method via step-length DN-SL for successive mesh refinement levels for power-law model for the power index values $r = 0.5$ and $r = 0.9$.

Power-law								
	$r = 0.5$				$r = 0.9$			
Level	**Fixed point**	**Newton**	**Adaptive point**	**Adaptive DN-SL**	**Fixed point**	**Newton**	**Adaptive point**	**Adaptive DN-SL**
3	17/1	8/1	8/1	8/1	*40/1	—	16/1	15/1
4	15/1	8/1	8/1	7/1	*40/1	—	16/1	15/1
5	14/1	8/1	8/1	7/1	*40/1	—	17/1	15/2
6	12/1	8/1	8/1	7/1	*40/1	—	17/2	16/2

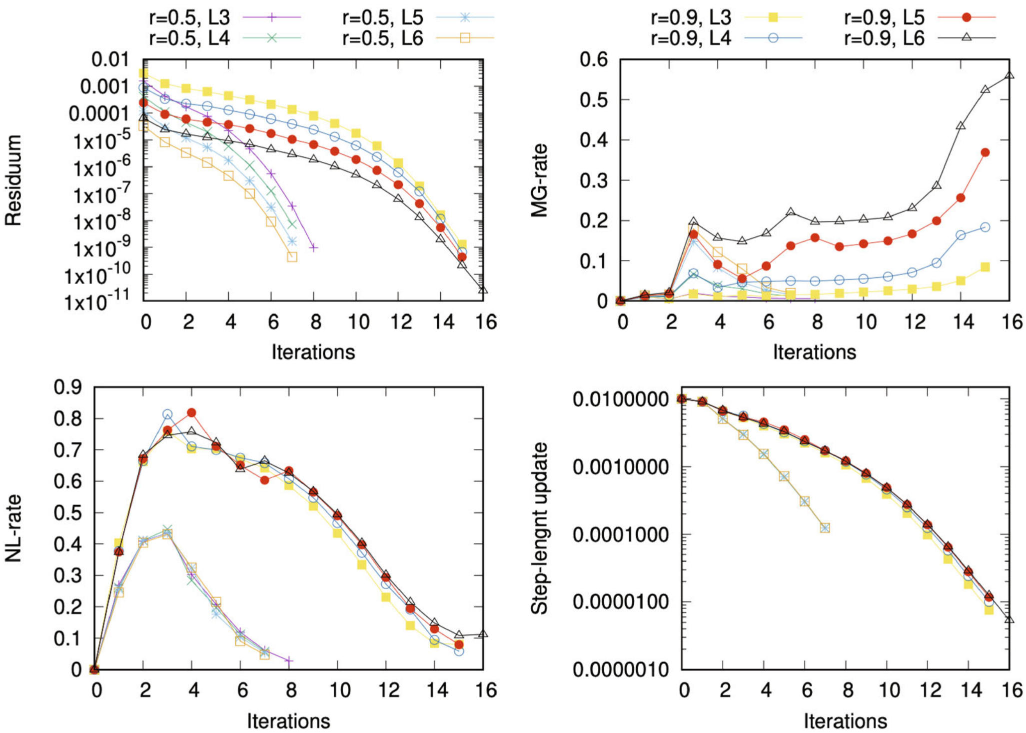

FIGURE A7 | Adaptive discrete Newton via step-length for flow around cylinder case study for power-law: Solver behavior, Residuum, Multgrid rate, Nonlinear rate, and the step-length update, during the convergence process for Newtonian flow w.r.t. mesh refinement levels, L3, L4, L5, and L6, and nonlinearity, that is, for the power indices $r = 0.5$, and 0.9. [Colour figure can be viewed at wileyonlinelibrary.com]

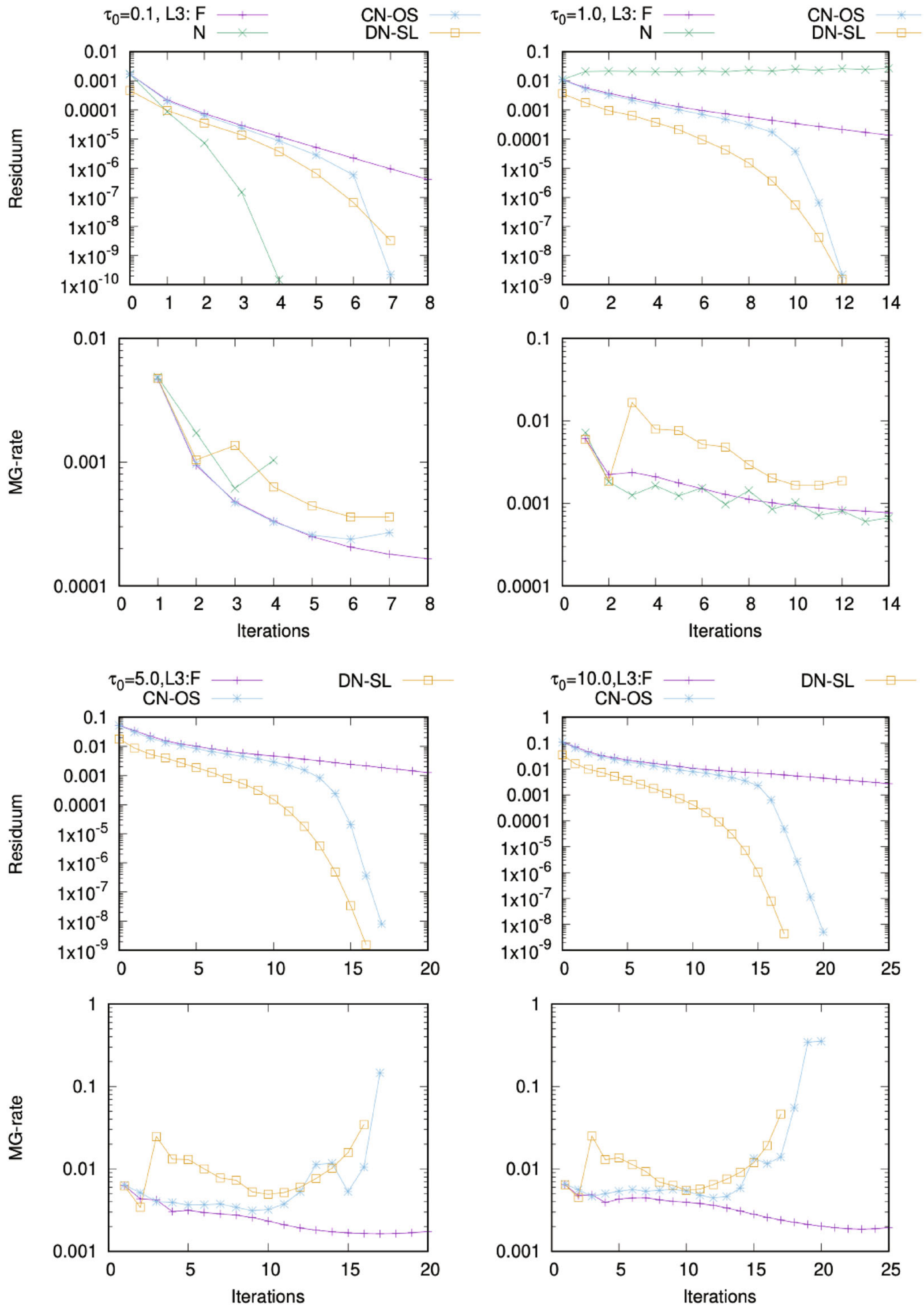

FIGURE A8 | Flow around cylinder case study for viscoplastic Bingham model: Performance comparison, in terms of Residuum convergence and Multigrid rate w.r.t. iterations, of fixed point, Newton's method, adaptive continuous Newton's method via operator splitting CN-OS, and adaptive discrete Newton's method via step-length DN-SL for successive mesh refinement levels for viscoplastic Bingham model for yield stress parameter values $\tau_0 = 0.1$, $\tau_0 = 1.0$, $\tau_0 = 5.0$, and $\tau_0 = 10.0$. [Colour figure can be viewed at wileyonlinelibrary.com]

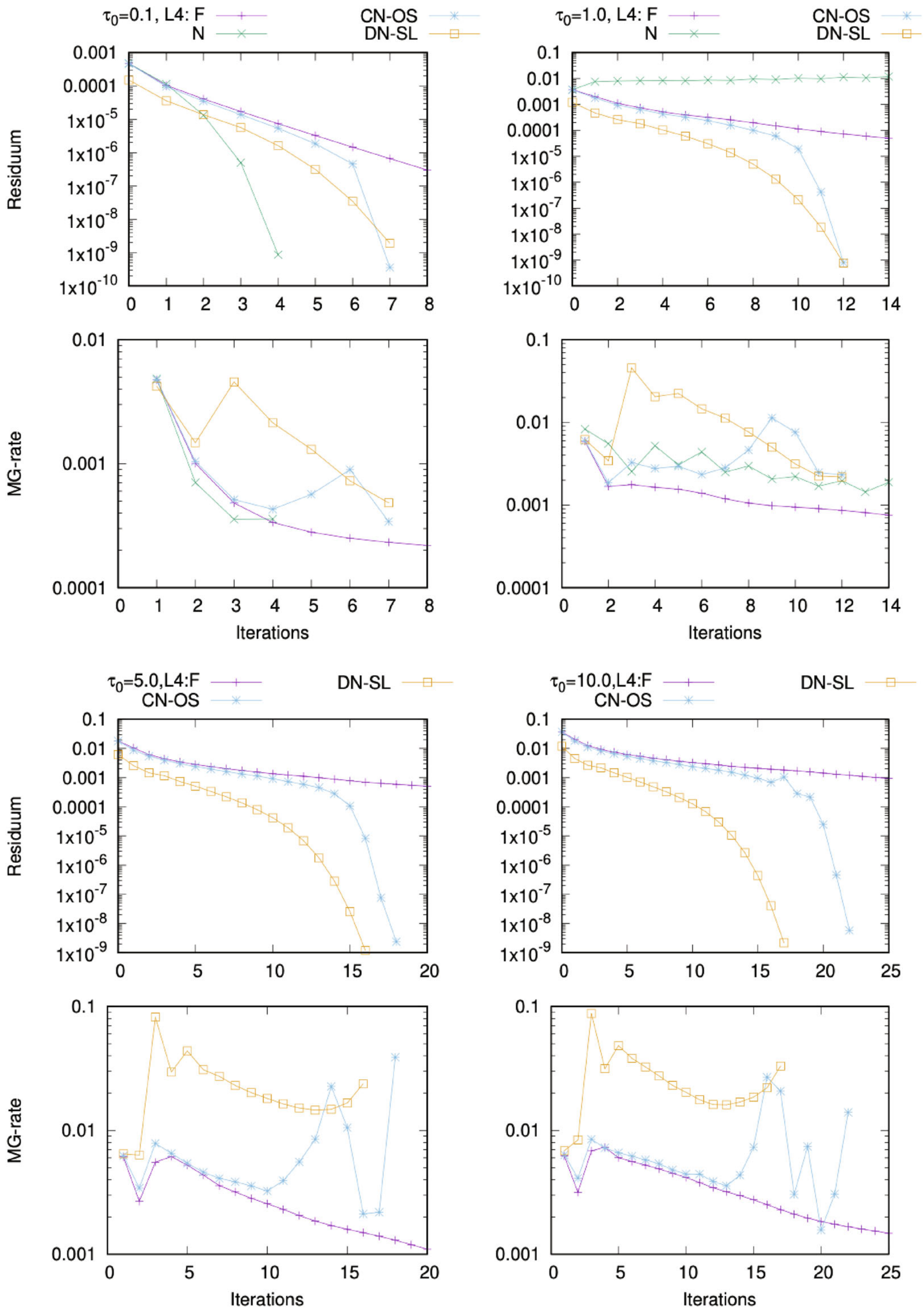

FIGURE A9 | Flow around cylinder case study for viscoplastic Bingham model: Performance comparison, in terms of Residuum convergence and Multigrid rate w.r.t. iterations, of fixed point, Newton's method, adaptive continuous Newton's method via operator splitting CN-OS, and adaptive discrete Newton's method via step-length DN-SL for successive mesh refinement levels for viscoplastic Bingham model for yield stress parameter values $\tau_0 = 0.1$, $\tau_0 = 1.0$, $\tau_0 = 5.0$, and $\tau_0 = 10.0$. [Colour figure can be viewed at wileyonlinelibrary.com]

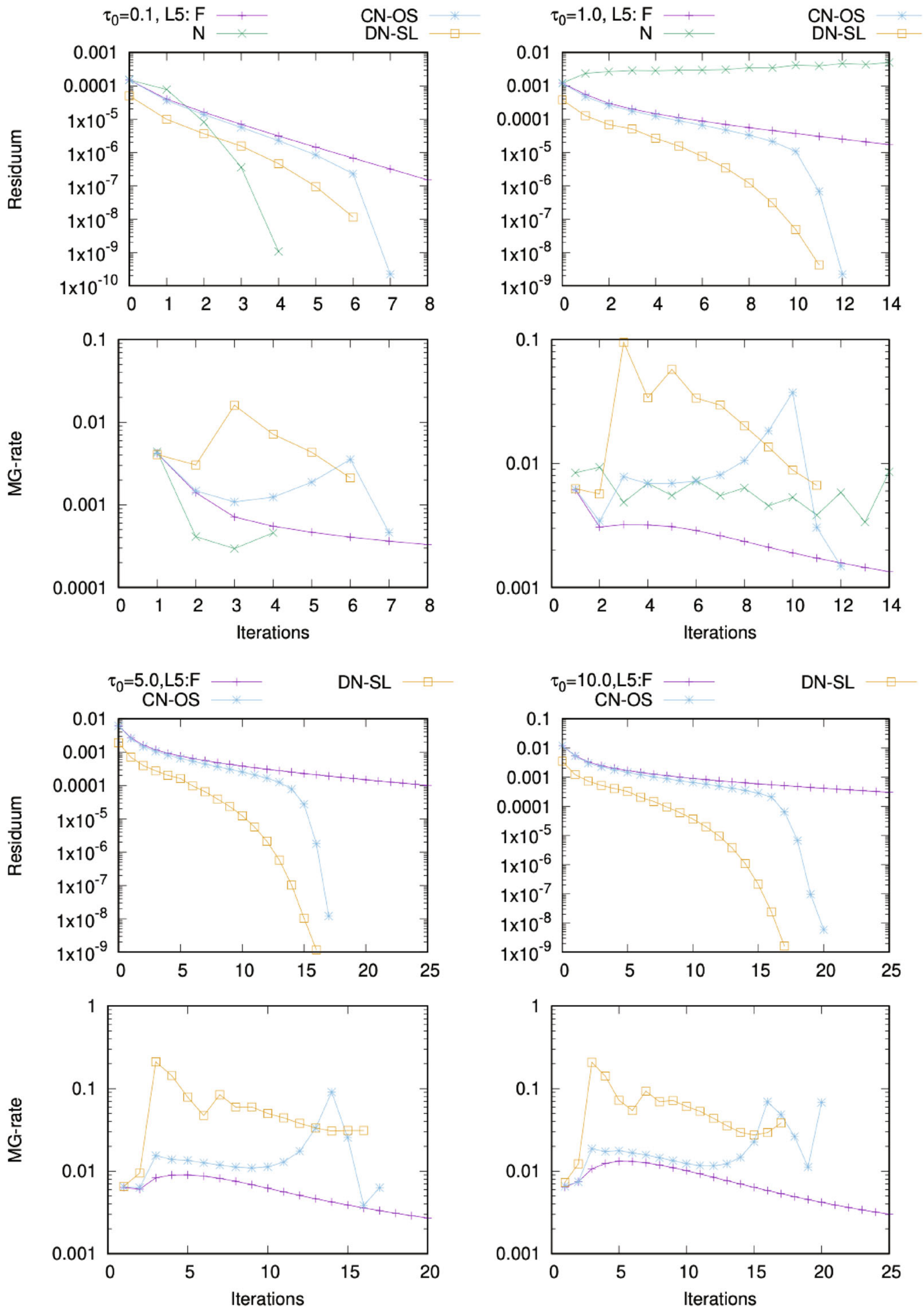

FIGURE A10 | Flow around cylinder case study for viscoplastic Bingham model: Performance comparison, in terms of Residuum convergence and Multigrid rate w.r.t. iterations, of fixed point, Newton's method, adaptive continuous Newton's method via operator splitting CN-OS, and adaptive discrete Newton's method via step-length DN-SL for successive mesh refinement levels for viscoplastic Bingham model for yield stress parameter values $\tau_0 = 0.1$, $\tau_0 = 1.0$, $\tau_0 = 5.0$, and $\tau_0 = 10.0$. [Colour figure can be viewed at wileyonlinelibrary.com]

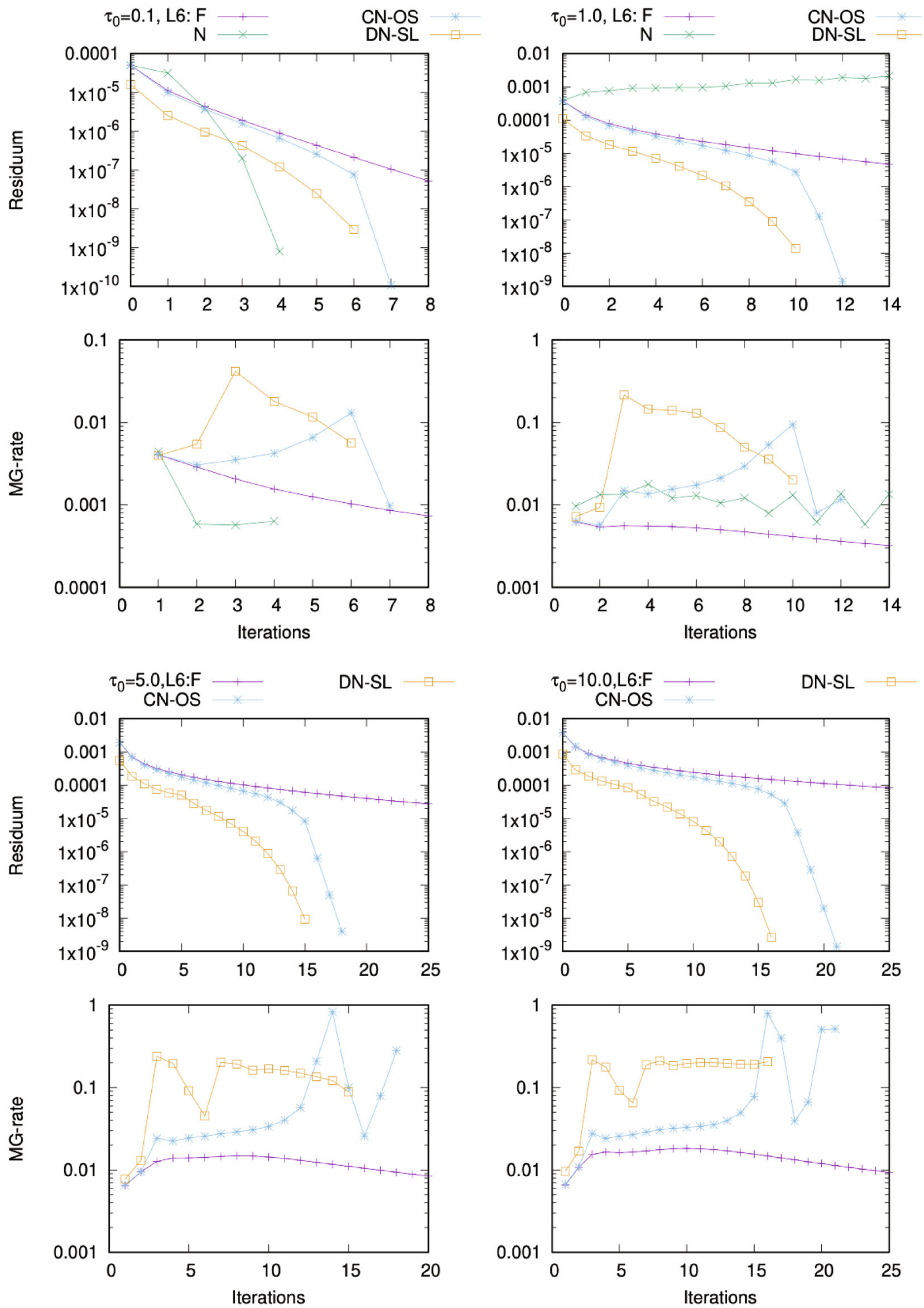

FIGURE A11 | Flow around cylinder case study for viscoplastic Bingham model: Performance comparison, in terms of Residuum convergence and Multigrid rate w.r.t. iterations, of fixed point, Newton's method, adaptive continuous Newton's method via operator splitting CN-OS, and adaptive discrete Newton's method via step-length DN-SL for successive mesh refinement levels for viscoplastic Bingham model for yield stress parameter values $\tau_0 = 0.1$, $\tau_0 = 1.0$, $\tau_0 = 5.0$, and $\tau_0 = 10.0$. [Colour figure can be viewed at wileyonlinelibrary.com]

TABLE A4 | Flow around cylinder case study for viscoplastic Bingham model: Statistic of the performance comparison, in terms of number of nonlinear iteration iterations, and the average number of multigrid required for one nonlinear iteration, of Fixed point method, Newton's method, adaptive continuous Newton's method via operator CN-OS splitting, and adaptive discrete Newton's method via step-length DN-SL for successive mesh refinement levels for viscoplastic Bingham model for yield stress parameter values $\tau_0 = 0.1$, $\tau_0 = 1.0$, $\tau_0 = 5.0$, and $\tau_0 = 10.0$.

Bingham viscoplastic model								
τ_0	**0.1**				**1.0**			
Level	**Fixed point**	**Newton**	**Adaptive CN-OS**	**Adaptive DN-SL**	**Fixed point**	**Newton**	**Adaptive CN-OS**	**Adaptive DN-SL**
3	12/1	4/1	7/1	7/1	*40/1	—	12/1	12/1
4	12/1	4/1	7/1	7/1	*40/1	—	12/1	12/1
5	12/1	4/1	7/1	6/1	*40/1	—	12/1	11/1
6	10/1	4/1	7/1	6/1	*40/1	—	12/1	10/1

Bingham viscoplastic model								
τ_0	**5.0**				**10.0**			
Level	**Fixed point**	**Newton**	**Adaptive CN-OS**	**Adaptive DN-SL**	**Fixed point**	**Newton**	**Adaptive CN-OS**	**Adaptive DN-SL**
3	*40/1	—	17/1	16/1	—	—	20/1	17/1
4	*40/1	—	18/1	16/1	—	—	22/1	17/1
5	*40/1	—	17/1	15/1	—	—	20/1	17/1
6	*40/1	—	18/2	15/2	—	—	21/2	16/2

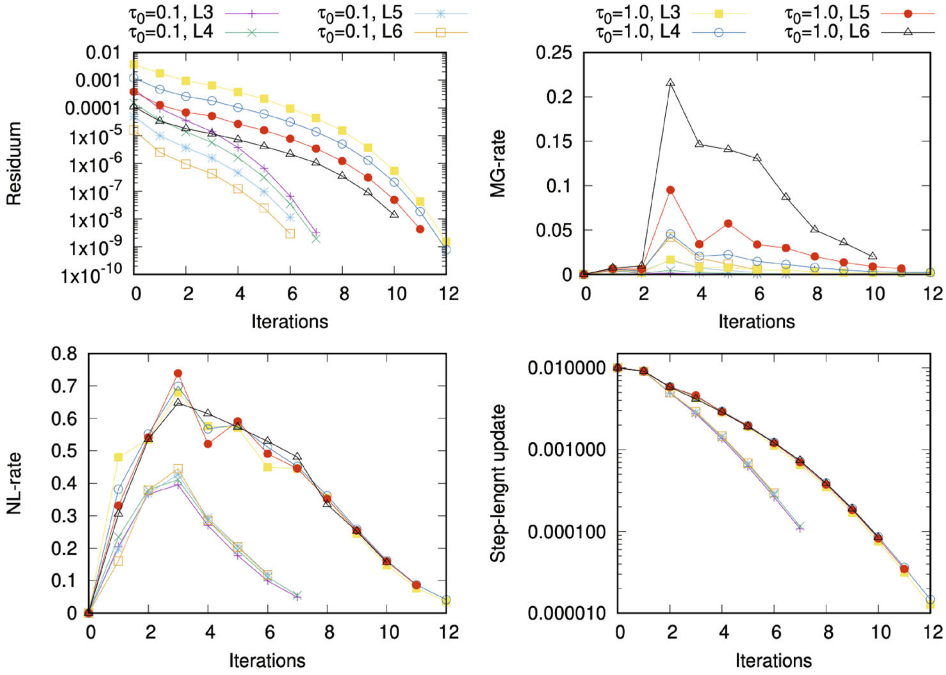

FIGURE A12 | Adaptive discrete Newton via step-length for flow around cylinder case study for viscoplastic Bingham model: Solver behavior, Residuum, Multgrid rate, Nonlinear rate, and the step-length update, during the convergence process for viscoplastic Bingham model w.r.t. mesh refinement levels, L3, L4, L5, and L6, and nonlinearity, that is, for the yield stress parameter values $\tau_0 = 0.1$ and $\tau_0 = 1.0$. [Colour figure can be viewed at wileyonlinelibrary.com]

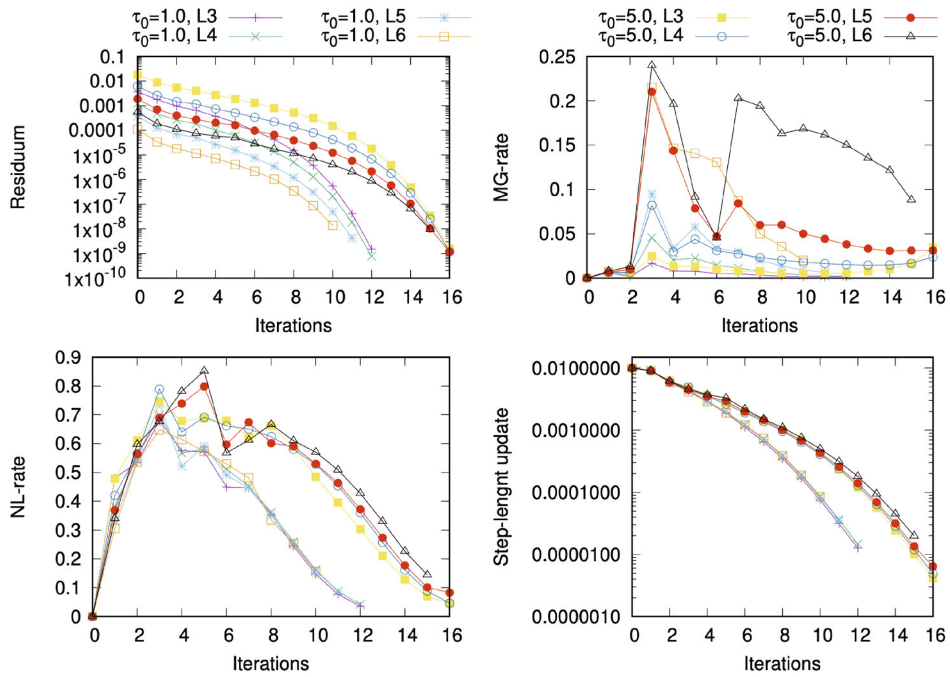

FIGURE A13 | Adaptive discrete Newton via step-length for flow around cylinder case study for viscoplastic Bingham model: Solver behavior, Residuum, Multgrid rate, Nonlinear rate, and the step-length update, during the convergence process for viscoplastic Bingham model w.r.t. mesh refinement levels, L3, L4, L5, and L6, and nonlinearity, that is, for the yield stress parameter values $\tau_0 = 1.0$ and $\tau_0 = 5.0$. [Colour figure can be viewed at wileyonlinelibrary.com]

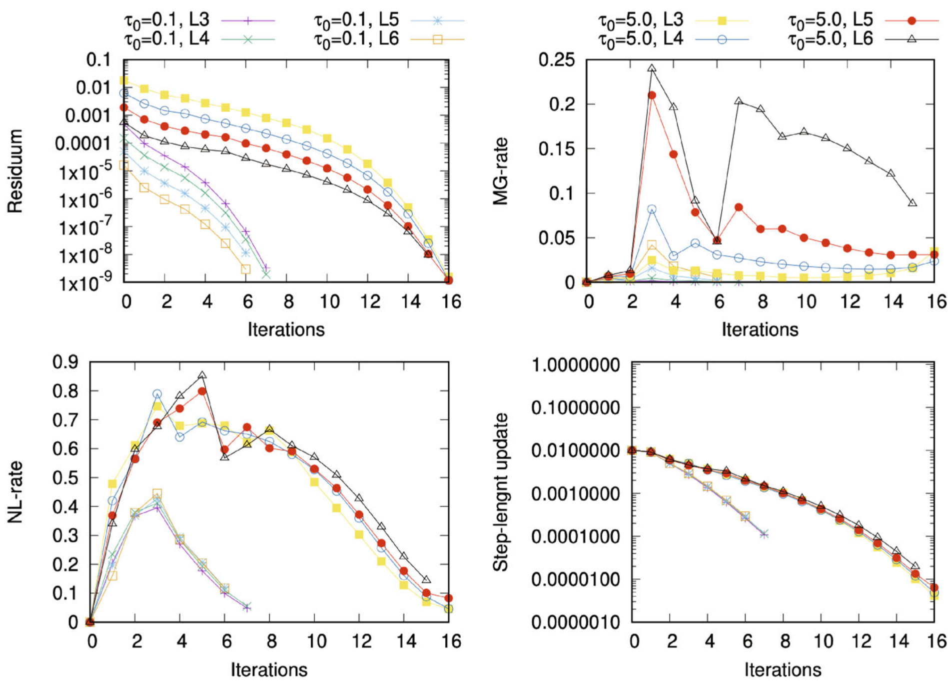

FIGURE A14 | Adaptive discrete Newton via step-length for viscoplastic Bingham model: Flow around cylinder study case. Solver behavior, Residuum, Multgrid rate, Nonlinear rate, and the step-length update, during the convergence process for viscoplastic Bingham model w.r.t. mesh refinement levels, L3, L4, L5, and L6, and nonlinearity, that is, for the yield stress parameter values $\tau_0 = 0.1$ and $\tau_0 = 5.0$. [Colour figure can be viewed at wileyonlinelibrary.com]

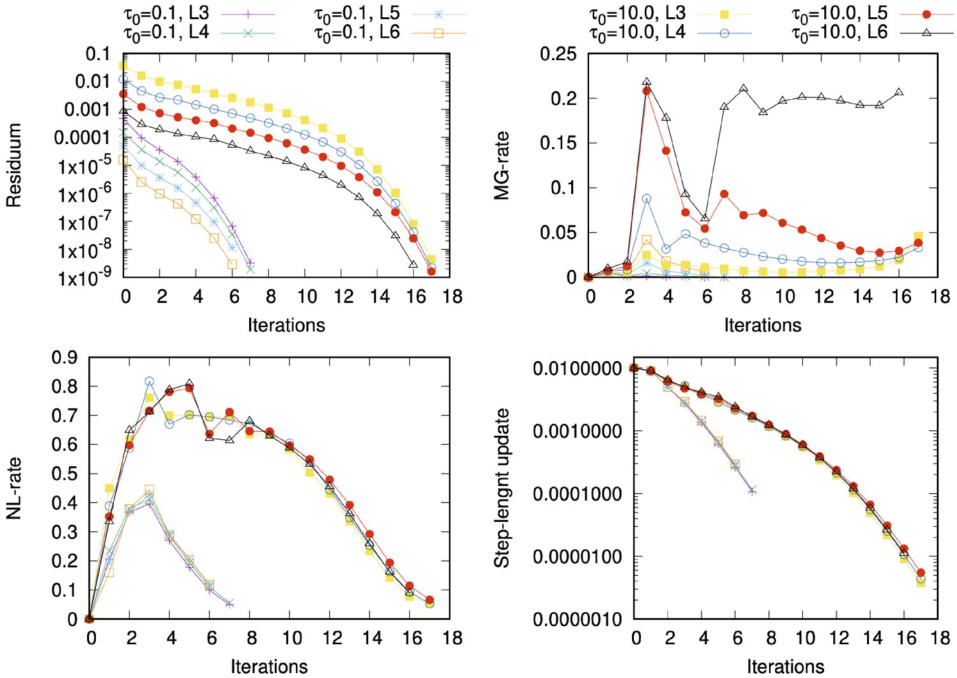

FIGURE A15 | Adaptive discrete Newton via step-length for viscoplastic Bingham model: Flow around cylinder study case. Solver behavior, Residuum, Multgrid rate, Nonlinear rate, and the step-length update, during the convergence process for viscoplastic Bingham model w.r.t. mesh refinement levels, L3, L4, L5, and L6, and nonlinearity, that is, for the yield stress parameter values $\tau_0 = 0.1$ and $\tau_0 = 10.0$. [Colour figure can be viewed at wileyonlinelibrary.com]